U.PORTO

FEUP FACULDADE DE ENGENHARIA
UNIVERSIDADE DO PORTO

Energy wear methods for dual-mortar contact analysis of frictional problems at finite inelastic strains

A DISSERTATION PRESENTED
BY
Thiago Doca
TO
THE DEPARTMENT OF MECHANICAL ENGINEERING

IN PARTIAL FULFILLMENT OF THE REQUIREMENTS
FOR THE DEGREE OF
DOCTOR OF PHILOSOPHY
IN THE SUBJECT OF
COMPUTATIONAL MECHANICS

PROF. F.M. ANDRADE PIRES, SUPERVISOR

UNIVERSITY OF PORTO
PARANHOS, PORTO
MAY 2014

Abstract

In a wide range of problems involving deformable bodies undergoing finite strains and experiencing inelastic material behavior, frictional contact and wear are inevitably present. These types of problems are very common in engineering practice and are of the utmost importance in forming operations, machine design and structural engineering. Therefore, a numerical strategy developed for the analysis of this variety of applications requires appropriate consideration of both theoretical and algorithmic issues.

The present work is concerned with the development of two energy-based formulations for the numerical simulation of frictional contact problems, at finite inelastic strains and fretting wear conditions. The first formulation, is a nested (two-step) scheme, while the second one is a single step fully implicit strategy. Both frameworks are based on the Mortar method of enforcement for the constraints [9]. In particular, lagrangian multipliers described in a dual-basis [83] associated with quadratic finite elements are employed. Element technology capable of dealing with plastic incompressibility and avoiding volumetric locking [15] is also included.

The contact and finite frictional sliding inequality constraints are reformulated in a set of so-called complementarity functions as in [33]. When combined with the equilibrium equations, which include nonlinear constitutive material behavior at finite strains [14, 20, 59, 69, 81], this leads to a system of nonlinear and non-differentiable equations that can be solved in terms of a semi-smooth Newton method. The resulting primal-dual active set strategy (PDASS) deals with nonlinearities stemming from contact (search for inactive, stick and slip set) and all other nonlinearities (i.e. geometrical and material) in one single iterative scheme. The consistent linearization of all terms of the framework (i.e. material, kinematic, frictional contact and wear) yields a robust, accurate and highly efficient approach for the numerical solution of frictional contact problems with deformable solids undergoing finite strains with inelastic behavior and able to account for material loss.

In order to evaluate fretting wear effects, a new numerical formulation based on the Dissipated energy method [28, 66, 79] is introduced. This formulation is able to model the fretting wear phenomena even when the boundary conditions (i.e. contact pressure, sliding distance, etc) are evolving. A new method for topography update of the contact interface is also described. Associated with a multi-directional frictional function, this method enables the solid's discretized shape to mimic real material behavior while preserving the aspect ratio of the finite elements involved in the degeneration process.

Within this thesis, several numerical examples are provided. They are used to investigate the performance, the accuracy and robustness of the presented formulations throughout comparison against experimental data and a classical formulation, the Archard method [2].

Resumo

Em um grande número de problemas envolvendo corpos sólidos sob o efeito de grandes deformações em regime inelástico, é inevitável a presença de contacto com atrito e desgaste. Estes problemas são de grande importância em processos de de conformação mecânica, maquinagem e engenharia estrutural. Portanto, estratégias visando a análise deste tipo de problema requerem abordagens apropriadas, tanto no aspecto teórico quanto numérico.

Neste trabalho são desenvolvidas duas formulações, baseadas no princípio de conservação de energia, voltadas à simulação numérica de problemas de contacto com atrito e sob condições de desgaste. A primeira formulação possui dois passos de solução iterativa, já a segunda possui um único passo de cálculo totalmente implícito. Ambas as estratégias computacionais são baseadas no método Mortar de imposição das condições de contacto [9]. Em particular, foram utilizados multiplicadores de Lagrange descritos em uma base dual em associação com elementos finitos de segunda ordem [83]. Adicionalmente, é também utilizada tecnologia de elementos [15] capaz de operar em regime de incompressibilidade e evitar distorções volumétricas.

As inequações de contacto e deslocamento com atrito são reformuladas utilizando funções de complementaridade [33]. Essas funções, quando combinadas com as equações de equilíbrio que incluam modelagem constitutiva de materiais não-lineares em regime de grandes deformações [14, 20, 59, 69, 81], geram um sistema de equações não-linear e não-diferenciável passivo de solução através do método *semi-smooth* de Newton. A estratégia de ativação nodal primal-dual (PDASS) resultante é capaz de lidar com a não-linearidade proveniente do contacto (busca e activação de nós) e demais não-linearidades (i.e. geométricas, material) em um único passo iterativo. A linearização consistente de todos os termos desta formulação (material, cinemática, atrito e desgaste) produz um método robusto, exato e muito eficiente para a solução de problemas de contacto com atrito, com grandes deformações inelásticas e com perda de material.

Para analisar os efeitos do desgaste, é apresentada uma nova formulação numérica baseada no método da energia dissipada [28, 66, 79]. Esta formulação é capaz de modelar o fenómeno de desgaste por *fretting* mesmo quando as condições de contorno iniciais (i.e. pressão, amplitude de deslocamento, etc) são alteradas ao longo da solução. Também é descrita um novo método de atualização da topografia da interface de contacto. Em associação com uma função de atrito multi-direcional, este método permite que a forma discretizada do sólido imite o comportamento real de materiais ao mesmo tempo em que preserva as características volumétricas dos elementos finitos envolvidos no processo de desgaste.

Nesta tese, diversos exemplos numéricos são disponibilizados. Eles são utilizados para investigar a desempenho, exatidão e robustez da presente formulação através de comparação com dados experimentais e com formulações clássicas, nomeadamente o método de Archard [2].

Acknowledgments

I would like to thank my supervisor Prof. Francisco Manuel Andrade Pires, for his invaluable support and guidance. Thanks is also due to Prof. José Manuel de Almeida César de Sá for helping me during my time as an assistant professor.

The contents of this work were partly funded by the Portuguese Science and Technology Foundation (FCT) under the scholarship SFRH/BD/66617/2009. I gratefully acknowledge this support.

I also would like to thank my colleagues at FEUP: Lucival Malcher, Filipe Xavier, Fábio Reis, Shenghua Wu and Mohsen Mirkhalaf.

Special thanks to all my friends who were always happy to see me back home every other summer. Thank you Lucianna, Ayo and Amanda for even visiting me during this time abroad. Thank you Eric and Kesley for being like brothers to me. I own a large debt of gratitude to my family. Particularly, I thank my mother Zilda and my grandparents Saulo and Ana, for the continuous support and kindness. Lastly, I wish to express my deepest love for my fiance Mirellen for her understanding and constant presence in my life during these last 4 years.

Porto, Winter of 2013.

Thiago Doca

Contents

List of Figures

List of Tables

List of Symbols

Abbreviations

BVP	boundary value problem
FE	finite element
KKT	KarushKuhnTucker
LTU	local topography update
NTN	node-to-node
NTS	node-to-surface
PDASS	primal-dual active set strategy
STS	segment-to-segment

Scalars

$n_{(\cdot)}$	number of $(\cdot)$
N	standard shape function
g	normal gap
p	normal pressure
w	material worn
h	wear depth
α_w	energy wear coefficient
β	velocity-traction ratio
ϵ	penalty parameter
c	complementarity parameter
E	Young's modulus
G	shear modulus
ν	Poisson's coefficient
σ_y	yield stress
μ	friction coefficient
ρ	relative density
A	plastic strain coefficient
b	plastic strain exponent
J	JACOBIAN determinant
φ	relative tangential velocity
ξ, χ, ζ	local coordinate parameters

Boundaries, Domains and Indexes

γ	boundary at spatial configuration
Γ	boundary at material configuration

Ω	domain of the solid
$(\cdot)_0$	entity at the reference configuration
$(\cdot)_t$	entity at the current configuration
$(\cdot)_c$	contact related entity
$(\cdot)_\sigma$	Neumann related entity
$(\cdot)_u$	Dirichlet related entity
$(\cdot)_\eta$	normal component
$(\cdot)_\tau$	tangential component
$(\cdot)^e$	elastic component
$(\cdot)^p$	plastic component
$(\cdot)^{ext}$	external
$(\cdot)^{int}$	internal
$\hat{(\cdot)}$	prescribed value
$\tilde{(\cdot)}$	weighted entity
$\bar{(\cdot)}$	averaged/modified quantity
$(\cdot)^h$	discretized entity
$\mathcal{I}, (\cdot)_\mathcal{I}$	inactive nodes and their associated entities
$\mathcal{A}, (\cdot)_\mathcal{A}$	active nodes and their associated entities
$\mathcal{S}, (\cdot)_\mathcal{S}$	slave nodes and their associated entities
$\mathcal{M}, (\cdot)_\mathcal{M}$	master node and their associated entities
$\mathcal{Q}, (\cdot)_\mathcal{Q}$	nodes and entities at stick-state condition
$\mathcal{L}, (\cdot)_\mathcal{L}$	nodes and entities at slip-state condition

Operators

$\Delta(\cdot)$	incremental quantity
$\delta(\cdot)$	virtual valued/test entity
$\frac{d}{dt}(\cdot)$	time derivative
$grad(\cdot)$	gradient operator, spatial configuration
$Grad(\cdot)$	gradient operator, material configuration
$span(\cdot)$	linear span operator
$det(\cdot)$	determinant
$exp(\cdot)$	exponential
$ln(\cdot)$	natural logarithm
$(\cdot)^T$	transpose operator
$(\cdot)^{-1}$	inverse operator
$\|(\cdot)\|$	absolute value
$\|\|(\cdot)\|\|$	Euclidean norm
$\mathsf{A}(\cdot)$	finite element assembly operator

Functions and Vectors

$\mathfrak{F}$	friction function
ϕ	dual shape function
Φ	yield function

C	complementarity function
$\mathbf{t}$	surface traction at spatial configuration
$\mathbf{T}$	surface traction at material configuration
$\mathbf{b}$	body force
$\mathbf{f}$	vector of forces
$\mathbf{r}$	vector of residual forces
$\mathbf{g}$	gap vector
Π	potential energy
$\boldsymbol{\varphi}$	motion
$\mathbf{x}$	spatial coordinates
$\mathbf{X}$	material coordinates
$\mathbf{u}$	displacement field
$\mathbf{v}$	displacement test functions
$\mathbf{d}$	nodal displacements
$\mathbf{z}$	nodal Lagrange multipliers
$\boldsymbol{\eta}$	surface normal at current configuration
$\mathbf{N}$	surface normal at reference configuration
$\boldsymbol{\tau}$	surface tangent at current configuration

Matrices and Tensors

C	right Cauchy-Green tensor
D	plastic stretch
E	Green-Lagrange tensor
F	deformation gradient
T	Kirchhoff stress
W	plastic spin
$\boldsymbol{\sigma}$	Cauchy stress tensor
$\mathbf{D}$	slave side Mortar matrix
$\mathbf{M}$	master side Mortar matrix
$\mathbf{F}$, $\mathbf{H}$, $\mathbf{Q}$	stick-state matrices
$\mathbf{J}$, $\mathbf{G}$, $\mathbf{L}$	slip-state matrices
$\mathbf{K}$	Stiffness matrix

To my family.

"A person who never made a mistake never tried anything new."
Albert Einstein (1879-1955)

Chapter 1

Introduction

1.1 Motivation

Contact mechanics phenomena arise in almost all manufacturing processes, natural phenomena and in our daily activities. Contact is almost a requirement to promote deformation and movement. It is essential to build a car, to predict an earthquake, to produce a biomechanical implant, to make a comfortable chair or even good shoes. To imagine an industrial process without contact arising during at least one of its stages is barely impossible. However, to visualize contact problems in our lives is much simpler than to model them.

Contact mechanics involves several sources of nonlinearity, which makes these problems extremely difficult to solve without resorting to finite element computations. Therefore, the interest of conducting research on robust and efficient numerical schemes to solve this class of problems is very high due to many reasons. Firstly, the range of contact problems that can be solved by analytical procedures is very limited. Secondly, experimental research on this subject is very expensive and/or time consuming (i.e. car crash tests and jewelery manufacture). Thirdly, due to the fact that some conditions are unpractical to be reproduced inside a laboratory: the contact of a turbine blade and it's frame case or the contact of the inner parts of a submerged drill, for example. Nevertheless, numerical simulations also have some shortcomings. The contact between solid bodies originates a highly nonlinear problem with a vast number of variables. In addition, the contact area has a nonlinear evolution (geometrical nonlinearity) and there is the well known nonlinear behavior due to the energy dissipation associated to the contact interaction (phenomenological nonlinearity). Finally, the material model, damage evolution and thermomechanical effects also increase the non-linearity of the problem.

A long path has been covered leading to the development of several commercial packages including contact algorithms. Ansys Workbench by Ansys solutions Inc., MSC Marc from MSC Software Co., Abaqus by Dassault systems and Elfen by Rockfield software LTD are examples of popular available packages, offering several types of contact formulations. However, some problems remained unsolved due to inability of these finite element codes to properly deal with complex geometries, energy dissipation, fracture, wear, crack propagation and many other phenomena.

1.2 Literature overview: Contact formulations

The study of contact phenomena started in the ancient Egypt with empirical approaches. By applying basic concepts of lubrication and rollers it was possible to reduce the frictional force developed in the contact interface of large stone blocks and ground. During the 15^{th} century these concepts were explored by Da Vinci, Amontons and Coulomb resulting in the well know "Coulomb's friction law". This approach considers bodies as non-deformable, which clearly restricts it's application to the solution of a small number of problems since the deformations and stresses inside the bodies can not be predicted. Another liability relies on the fact that the frictional force was treated only as a function of the friction coefficient (excluding surface roughness effects) reducing even more the application field.

A more realistic approach was later developed by Hertz [38] when the theory of elasticity was applied to obtain an analytical solution to describe stresses and deformations near the contact point. Half a century later, Signorini [68] devised a general formulation for frictionless contact problems establishing the boundary conditions for an elastic/rigid contact between two bodies, which leaded to works such as the ones conducted by Goldsmith [34]. He analyzed several elastic contact/impact problems supported by experimental tests. However, due to the complexity of the treatment of the non-linearity associated with the contact area, the number of problems that could be solved analytically with this formulation was relatively small.

In the first applications of the finite elements method (FEM) into contact problems of two deformable bodies, only small changes in the geometry were assumed such that the geometrically linear theory could be applied. In this case, it is possible to incorporate the contact constraints on a purely nodal basis, see e.g. Francavilla & Zienkiewicz [30]. Later, contact elements accounting for element degeneration/distortion were developed, see e.g. Stadter & Weiss [74]. A mathematical study of these classes of elements which also accounts for the correct integration rules, can be found in Oden [55]. All of the above mentioned elements need a discretization where the element nodes match each other at the contact interface. For the general case of nodes being arbitrarily distributed along the possible contact interface between two bodies, which can occur when automatic meshing is used for two different bodies, Simo et al. [72] developed a segment approach to discretize the contact interface. For further information on early treatments of contact problems with the finite element method, the reader is referred to Wilson & Parsons [82], Timoshenko [76], Johnson [46], Belytschko et al. [8] and Hughes et al. [44].

In the early seventies, an initial formulation, accounting for frictional behavior and limited to elastic response, was proposed by Fredriksson [31]. Later, the development of theories of plasticity and linear viscoelasticity enabled the appropriate treatment of problems involving frictional contact of inelastic bodies (e.g. Bathe & Chaudhary [4], Ju & Taylor [47] and Wriggers et al [87]). Hence, with the progress of digital computers and finite element codes, formulations mainly based on the Penalty and Lagrangian multiplier methods, allowed the numerical solution of a much larger number of contact problems (see Kikuchi & Oden [48] and Simo & Hughes [70]).

Over the 20^{th} century, several algorithms have been proposed for the numerical treatment of frictional contact conditions and deformable bodies [50, 85]. The contact formulations were initially based on the node-to-segment (NTS) approach, which has been extended and generalized by numerous authors [19, 36, 75, 87]. Although quite popular and widely used, there are well known limitations in the robustness of NTS formulations. It has been shown in Papadopoulos & Taylor [57] that the so-called single pass algorithms do not satisfy the contact patch test and there is a degradation of spatial convergence rates. Furthermore, non-physical jumps in the contact forces can occur when finite sliding situations occur due to the non-smoothness of the discretized contact surfaces. Several strategies have been proposed to overcome these issues [64, 73, 86], leading to more elaborated algorithms.

Early in this decade, alternative methods for discretizing the contact surface based on the so-called segment-to-segment (STS) approaches, where introduced. For instance, the Mortar element method introduced by Bernardi et al. [9] has become very popular. It was originally designed as a domain decomposition technique and is particularly suited for the exchange of information between non-conforming meshes [6, 7]. It introduces the continuity condition at the interface in an integral form, rather than as nodal constrains. Of particular importance is the fact that this enforcement method preserves optimal convergence rates from the finite element method as long as suitable mortar spaces are chosen. Belgacem et al. [5] and McDewitt & Laursen [54] were among the first researchers applying these concepts to contact mechanics.

The search for improvements on the field of domain decomposition leaded to the formulation of the so-called dual Mortar method. This approach, proposed by Wohlmuth [83] employ dual spaces for the Lagrange multipliers, which applied to the contact environment allows for the local elimination of the contact constraints. As a consequence, the Lagrangian multipliers can be conveniently condensed and no additional equations are needed for the solution of the global system of equations [23, 84]. The remaining problem is positive definite and the unknowns are the displacements only. The reformulation of the frictional contact constraints into so-called complementarity functions [1,49] allows rewriting the inequality constraints as equalities. The combination of this set of equalities with the equilibrium equations leads to a system of nonlinear equations that can be solved with the semi-smooth Newton method [11, 21] or be equivalently interpreted as a primal-dual active set strategy (PDASS) [39, 42]

The first implementations of the PDASS, in the context of small deformation frictional contact, has been introduced by Hüeber et al. [41]. This strategy was latter applied to nonlinear material problems at small strains in Brunssen et al. [10] and in Hager & Wohlmuth [35]. While the solution of dynamic contact problems can be found in Hartmann et al. [37]. In the recent years, through the addition of complementarity parameters, consistently linearized formulations for the solution frictionless contact were introduced in Popp et al. [62] and for frictional contact in Gitterle et al. [33].

1.3 Literature overview: Fretting Wear formulations

Wear has been subject of intense research for over 40 years, especially for the study of metal coatings and elastomeric protective layers. Although most of the studies on this topic are experimentally based, numerical simulation of such a class of problems has had a significant growth over the recent years. In particular, formulations employing the Archard method [2] combined with the classical NTS contact formulation [17, 53, 60]. The Archard method uses the input variables from the contact setting (i.e. prescribed normal load, displacement amplitude, friction coefficient, etc) to calculate the wear loss. Consequently, the Archard coefficient becomes dependent of the problem's initial conditions [45]. This liability limits the range of applications of the Archard method to problems that do not experience changes in the loading conditions. For such a class of problems, the energy-based methods has shown better results [25, 58, 66]. For instance, the Dissipated energy method [27, 28] only uses the measurements of the contact problem. In particular, the friction force and the displacement. During this evaluation a friction map [78], containing the information about the total amount of energy lost, is created. Finally, this dissipated energy is related to the material worn using an independent parameter: the energy wear coefficient.

1.4 Objectives

The mortar formulation employing dual spaces for the Lagrange multipliers combined with the PDASS for the enforcement of constraints has undergone substantial progress in the last years. An extension of this formulation to include both finite strain inelastic material behavior and finite frictional sliding is still not available in the literature. A contact formulation that includes all the features stated above has been presented in [18] and will be discussed here. In addition, the Mortar method with quadratic dual-basis for the lagrangian multipliers with second order finite elements is studied and compared to other methods of constraint enforcement.

Despite the fact that many works aim to model the fretting wear phenomena, very few actually address deformation and fretting wear simultaneously. In most predictive tools available in the literature, the contact laws are restricted to the enforcement of the non-penetration rule. Moreover, the level of contact forces are kept so small that they become insignificant when compared with the wear depth evolution. This leads to the material being removed without ever reaching finite levels of strain. Also very common, are formulations that make use of the analytical solution for the contact pressure (i.e Hertz formulae in the context of small strains) in the first loading cycle, ignoring the wear effect and the removal of material in the subsequent cycles. Inevitably, these approaches provide inaccurate results. In addition, the available methods are mainly focused on the two-dimensional wear analysis of a single solid. In this work, a framework crafted for the analysis of two- and three-dimensional finite strain frictional contact problems including solutions

for the analysis of the fretting wear phenomena, for multiple bodies, is introduced.

1.5 Outline

This work is structured as follows:

Chapter 2
Describes the physical laws that govern the contact mechanics of frictional solid bodies in the context of finite strains and fretting wear condition. It also contains an extension of the Coulomb friction conditions to the three dimensional setting, in order to allow the analysis of wear problems.

Chapter 3
Introduces the general definitions concerning the wear phenomena are provided. Additionally, a new energy-based fretting wear formulation, in conjunction with methods for shape representation of worn surfaces.

Chapter 4
The numerical implementation of the frictional contact problem with finite strains and fretting wear is presented. It includes the weak formulation problem, the introduction of the Mortar method concepts for segmentation of the contact interface and the reformulations of the contact constraints and frictional conditions, for both two- and three-dimensional analysis.

Chapter 5
Contains the algebraic form of the consistently linearized contact problem alongside with two different ways of solving the residual system of equations.

Chapter 6
To validate and access the performance of the proposed methods, a vast collection of numerical examples is discussed in this chapter.

Chapter 7
This chapter summarizes the conclusions drawn during this work. It also contains final remarks concerning the results obtained in the preceding chapter and the perspectives of future work.

Appendices
Appendix A presents the Total Lagrange formulation employed for the evaluation of the internal forces.
Appendix B introduces the most relevant directional derivatives required for the incremental solution.
Appendix C gives a brief overview of the Penalty method.
Appendix D illustrates two patch tests.

Chapter 2

Contact mechanics of solid bodies

Contact mechanics is the study of the stresses and deformations which arise when multiples bodies in space are brought in contact. In this chapter, the physical laws that govern the contact between solid bodies are provided. Both friction and fretting Wear phenomena are also covered. The Section 2.1 provides the equations that govern the kinematics of the frictional contact problem and the topographic update of the contact surfaces due to fretting Wear. The Section 2.2 presents the strong formulation of the problem. Section 2.3 describes the equations employed for the enforcement of the contact constrains and update of the wear depth. Lastly, Section 2.4 addresses the constitutive material models commonly employed to characterize the mechanical behavior of solids.

2.1 Kinematic description

The kinematical description of the contact problem with finite strains, finite sliding and topographic wear update is given in Figure 2.1. The motion, $\mathbf{x}$, is described by a mapping φ between the reference configuration $\mathbf{X}$ (at time 0) and the current configuration $\mathbf{x}$ (at time t),

$$\mathbf{x} = \varphi\left(\mathbf{X}, t\right). \tag{2.1}$$

Therefore, the vector of nodal displacements, $\mathbf{u}$, is obtained from the reference configuration, as follows,

$$\mathbf{u}\left(\mathbf{X}, t\right) = \mathbf{x}\left(\mathbf{X}, t\right) - \mathbf{X}. \tag{2.2}$$

It is assumed that the bodies are only subjected to body forces, $\mathbf{b}$, and applied boundary traction, $\hat{\mathbf{t}}$. The solid bodies in the reference configuration, are denoted by Ω_0^s and Ω_0^m, $\{\Omega_0^s \cup \Omega_0^m = \Omega_0 : \Omega \subset \mathbb{R}^{n_{dim}}\}$, where n_{dim} denotes the spatial dimension. The superscripts s and m represent the common nomenclature employed in contact mechanics of a *Slave* and a *Master* body. $\Gamma_{_D}$ represents the Dirichlet boundary while $\gamma_{_N}$ is defined as the Neumann boundary The potential contact zone is represented by, $\Gamma_c = \{\Gamma_c^s \cup \Gamma_c^m\}$ and the spatial counterparts of the three boundaries are denoted by γ_c, $\gamma_{_N}$ and $\gamma_{_D}$, respectively.

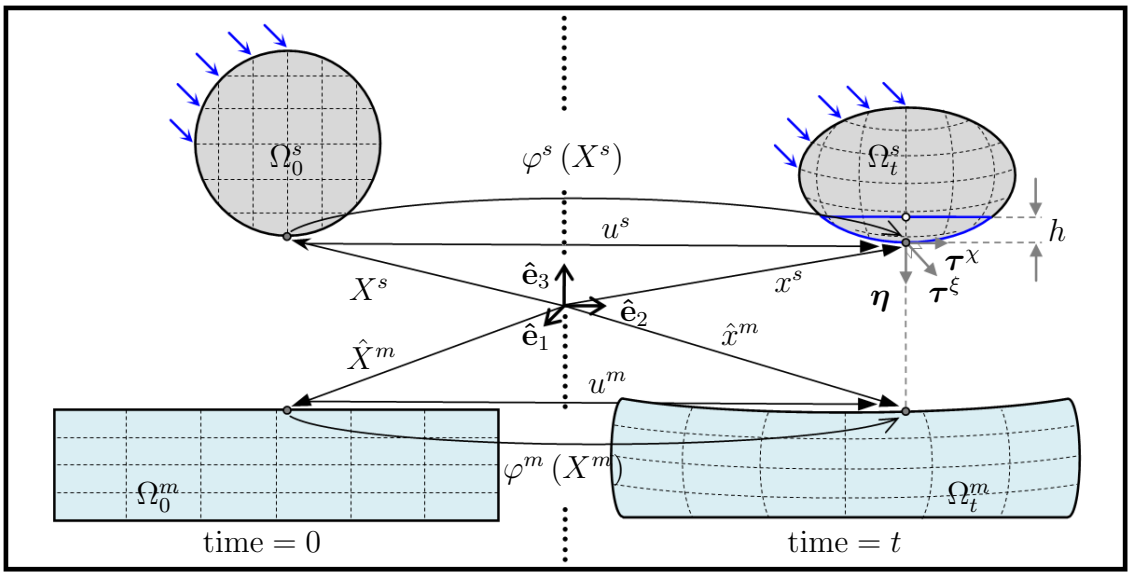

Figure 2.1: Illustration of a two bodies contact problem.

2.2 Strong form

The strong form of the frictional contact problem is stated here. The Boundary Value Problem (BVP), defined in terms of the displacement vector $\mathbf{u}$ and the Cauchy stress tensor, $\boldsymbol{\sigma}$, in the current configuration, is given as follows:

$$\begin{aligned} \operatorname{div}(\boldsymbol{\sigma}^i(\mathbf{u})) + \mathbf{b}^i &= 0 && \text{in } \Omega_t^i, \\ \boldsymbol{\sigma}^i(\mathbf{u})\boldsymbol{\eta}^i &= \hat{\mathbf{t}}^i && \text{on } \gamma_N^i \\ \mathbf{u}^i &= \hat{\mathbf{u}}^i && \text{on } \gamma_D^i, \ i = s, m. \end{aligned} \tag{2.3}$$

where $\hat{\mathbf{u}}^i$ and $\boldsymbol{\eta}^i$ represents the prescribed displacement and the current outward unit normal vector, respectively. Index i emphasizes that the BVP condition must be attained for all bodies involved. Furthermore, the deformation gradient, F, with respect to the reference configuration, Ω_0, is given by

$$\mathsf{F} = \nabla\varphi(\mathbf{X}, t) = \frac{\partial\varphi(\mathbf{X}, t)}{\partial\mathbf{X}} = \frac{\partial\mathbf{x}}{\partial\mathbf{X}}\ , \tag{2.4}$$

and its used to define the right Cauchy-Green, C^i, and the Green-Lagrange, E^i, strain tensors,

$$\mathsf{C}^i = \left[\mathsf{F}^i\right]^T \mathsf{F}^i, \tag{2.5}$$

$$\mathsf{E}^i = \frac{1}{2}\left\{\left[\mathsf{F}^i\right]^T \mathsf{F}^i - \mathbf{I}\right\}. \tag{2.6}$$

The determinant of the deformation gradient has to be greater than zero, $J = \det(\mathsf{F})$, in order for the motion of the bodies to be meaningful.

Further details on the solution of the boundary value problem, in the context a a Total Lagrange formulation, can be found in Appendix A.

2.3 Contact constraints and wear depth

For enforcing the contact constraints at normal and tangential directions in a three-dimensional domain, the surface tractions defined on the slave surface, $\mathbf{t}_c^s$, are decomposed as follows,

$$\mathbf{t}_c^s = p_\eta \boldsymbol{\eta} + t_\tau^\xi \boldsymbol{\tau}^\xi + t_\tau^\chi \boldsymbol{\tau}^\chi,\ p_\eta = \mathbf{t}_c^s \cdot \boldsymbol{\eta},\ t_\tau^\xi = \mathbf{t}_c^s \cdot \boldsymbol{\tau}^\xi,\ t_\tau^\chi = \mathbf{t}_c^s \cdot \boldsymbol{\tau}^\chi, \tag{2.7}$$

where the current outward unit normal, $\boldsymbol{\eta}$, defined on the slave surface, γ_c^s, in conjunction with unit tangential vectors $\boldsymbol{\tau}^\xi$ and $\boldsymbol{\tau}^\chi$ produce an orthonormal basis in x^s point, as seen in Figure 2.1.

2.3.1 Normal constraints

Constraints in the normal direction are fulfilled by a non-penetration condition which evaluates the relative distance (*gap*) between, $\mathbf{x}^s$, on the slave surface and, $\hat{\mathbf{x}}^m$, over the master surface in the current configuration – see Figure 2.1. The caret represents that $\hat{\mathbf{x}}^m$ is the closest projection of $\mathbf{x}^s$ onto the master surface, γ_c^m. This gap vector is obtained, in the current configuration, as follows,

$$\mathbf{g}(\mathbf{X}^s, t) = [\mathbf{x}^s(\mathbf{X}^s, t) - \hat{\mathbf{x}}^m(\hat{\mathbf{X}}^m, t)]. \tag{2.8}$$

Furthermore, the computation of the normal distance between $\mathbf{x}^s$ and $\hat{\mathbf{x}}^m$ yields the definition of the scalar-valued gap function,

$$g(\mathbf{X}^s, t) = -\boldsymbol{\eta}\left(\mathbf{x}^s(\mathbf{X}^s, t)\right) \cdot \mathbf{g}(\mathbf{X}^s, t). \tag{2.9}$$

Together with the definition of a non-positive normal contact traction, p_η, and a positive wear depth state variable, $h(\mathbf{X}^s, t)$, the following set of inequalities must be attained:

$$g(\mathbf{X}^s, t) + h(\mathbf{X}^s, t) \geq 0, \quad p_\eta \leq 0, \quad p_\eta[g(\mathbf{X}^s, t) + h(\mathbf{X}^s, t)] := 0. \tag{2.10}$$

2.3.2 Tangential constraints

The frictional conditions, for the two-dimensional domain, are fulfilled by employing the standard Coulomb's law:

$$\mathfrak{F} := |t_\tau| - \mu |p_\eta| \leq 0,\ \forall\ \Omega_0 \in \mathbb{R}^2. \tag{2.11}$$

$$\vartheta_\tau\left(\mathbf{X}^s, t\right) + \beta \mathbf{t}_\tau = 0,\ \forall\ \beta \geq 0, \tag{2.12}$$

where $\mu \geq 0$ represents the coefficient of friction given by the ratio of the normal and tangential forces, depicted in Figure 2.2. The relative tangential velocity, $\vartheta_\tau(\mathbf{X}^s, t)$, is defined as the rate of change:

$$\dot{(*)} = \frac{d(*)}{dt} \approx \frac{(*)_t - (*)_0}{\Delta t}, \tag{2.13}$$

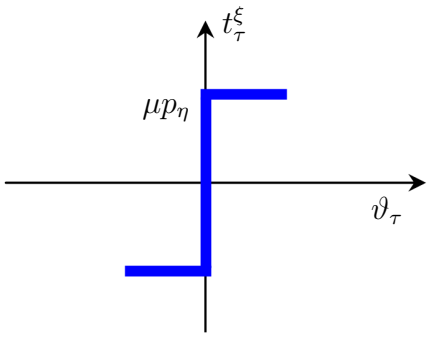

Figure 2.2: Coulomb's frictional contact conditions.

of the gap vector in the tangential direction, Equation (2.8),

$$\vartheta_\tau(\mathbf{X}^s, t) = \boldsymbol{\tau}\left(\mathbf{x}^s(\mathbf{X}^s, t)\right) \cdot \dot{\mathbf{g}}(\mathbf{X}^s, t). \tag{2.14}$$

Tangential stresses below the Coulomb threshold, $\mathfrak{F} < 0$, Equation (2.11), imply a tangential velocity, ϑ_τ, equal to zero, commonly called as stick/static state. When tangential stresses are at the Coulomb limit, they are opposed by the relative tangential velocity. In this case, we have a slip/kinectic state. The association of these two definitions generates the following state equation,

$$\mathfrak{F}\beta = 0. \tag{2.15}$$

2.3.3 Modified Coulomb's frictional condition

Due to the cyclical nature of the fretting wear phenomena, sudden changes on the tangential traction's orientation and direction (i.e. reciprocating motion, axis rotation, radial rotation) are very common. Therefore, in order to maintain the frictional force directions while the surface topography is updated, a modified version of the Coulomb function must be introduced. For the analysis of three-dimensional fretting wear problems, the tangential constraints must be fulfilled in a two-dimensional space ($\boldsymbol{\tau}^\xi$,$\boldsymbol{\tau}^\chi$). Therefore, in this work a parameterized function, $\bar{\mathfrak{F}}$ is employed,

$$\bar{\mathfrak{F}}\left(x = \vartheta_\tau, y = \boldsymbol{\chi}^\xi, z = \mu|p_\eta|\right) \leq 0, \ \forall\ \Omega_0 \in \mathbb{R}^3 \tag{2.16}$$

The definition of this tri-directional frictional function enforces a smoother transition from the stick state to the slip state while also maintaining the direction of the material removal process. The constants a, b, c and the directional parameters $[u, v]$ employed in the function, were specifically designed to reproduce reciprocating, circular motion, axis rotation and combination of these three, in an accurate manner. However, by choosing appropriate values for these constants, elliptical motion can be addressed as well.

The direction, z is used to describe the relation between the friction force and the normal force for a uni-direction motion. Therefore, the function $z(u, v)$ can be interpreted as an approximation of the standard Coulomb's friction, as depicted

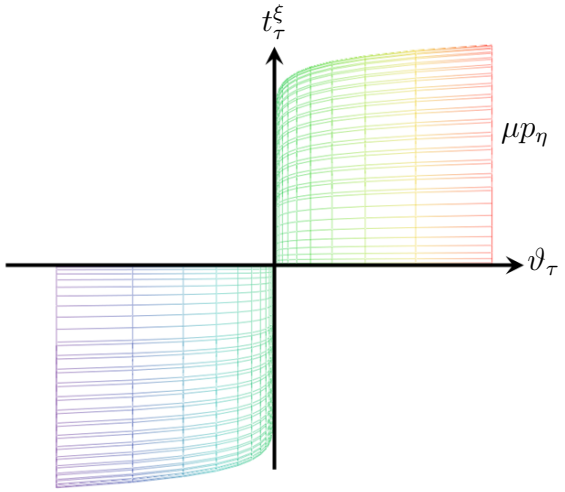

Figure 2.3: Continuous friction function - X-Z plot.

in Figure 2.3. The functions $x(u, v)$ and $y(u, v)$ are employed to describe circular motion and axis rotation, respectively. Their values are given as follows,

$$\begin{aligned} x(u,v) &= au[1 - cos(v)], \\ y(u,v) &= bu[sin(v)], \\ z(u,v) &= c[u]^7, \end{aligned} \tag{2.17}$$

where $a = \frac{1}{8}$; $b = \frac{1}{4}$; $c = \frac{1}{50000}$ for $u \in [-1, 1]$ and $v \in [0, 2\pi]$.

It is important to remark that for solving uni-directional two-dimensional contact problems, one may set the parameter $y = 0$ and recover the standard Coulomb's condition on the two-dimensional domain, $\bar{\mathfrak{F}} = \mathfrak{F}$, as stated in Equation (2.11) and shown in Figure 2.2. Furthermore, setting parameter $z = 0$, a frictionless formulation ($\mu = 0$) is obtained. Moreover, the wear phenomena can benefit from the smoother transition between stick and slip states provided by the continuous function $z(u, v)$. The surface plot given by the set of frictional conditions in the three-dimensional domain is depicted in Figure 2.4.

A summarized statement of the frictional contact constraints for the modified Coulomb friction is given by,

$$\begin{aligned} \bar{\mathfrak{F}}(x,y,z) &\leq 0 \;\forall\; \Omega_0 \subset \mathbb{R}^3; \\ \bar{\mathfrak{F}}(x,0,z) = \mathfrak{F} &\leq 0 \;\forall\; \Omega_0 \subset \mathbb{R}^2; \\ \vartheta_\tau\left(\mathbf{X}^s, t\right) - \beta \mathbf{t}_\tau = \mathbf{0},\ \wedge\ \beta \geq 0 \ \ \therefore\ \ \bar{\mathfrak{F}}\beta &= 0. \end{aligned} \tag{2.18}$$

More details about the topography update procedure are provided in Chapter 3.

2.4 Constitutive modelling

The modelling of nonlinear solid material behavior has undergone substantial development over the last decades and, as result, a wide range of material models,

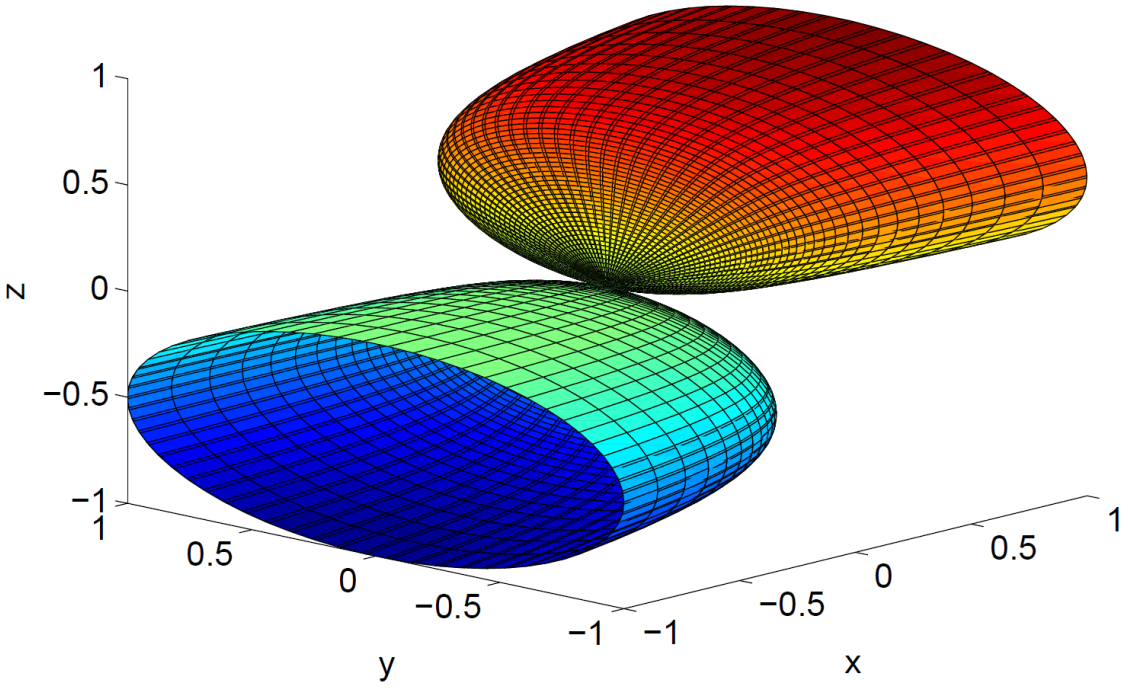

Figure 2.4: Three-dimensional continuous friction function.

incorporating elastic, viscoelastic and viscoplastic material behavior are currently available [13, 16].

2.4.1 Finite Inelastic deformations

A class of isotropic hyperelastic based finite strain inelastic constitutive models, formulated in the spatial configuration, is considered here. A more detailed discussion of the approach, which is well established and widely accepted for the description of finitely deforming solids, can be found in [13, 16].

The main hypothesis underlying this class of models is the multiplicative decomposition of the deformation gradient, F, into an elastic, F^e, and a plastic, F^p, contributions,

$$\mathsf{F} = \mathsf{F}^e \mathsf{F}^p \tag{2.19}$$

which was first introduced by Lee [52] and admits the existence of a local unstressed intermediate-configuration defined by the plastic deformation gradient, F^p. The polar decomposition of the elastic and plastic deformation gradients leads to:

$$\mathsf{F}^e = \mathsf{R}^e \mathsf{U}^e = \mathsf{V}^e \mathsf{R}^e, \;\; \mathsf{F}^p = \mathsf{R}^p \mathsf{U}^p = \mathsf{V}^p \mathsf{R}^p, \tag{2.20}$$

where U^e and U^p are the elastic and the plastic right stretch tensors, V^e and V^p are the elastic and plastic left stretch tensors and R^e and R^p the elastic and plastic rotation tensors.

The velocity gradient, $\mathsf{L} = \dot{\mathsf{F}}\mathsf{F}^{-1}$, can be decomposed additively as,

$$\mathsf{L} = \mathsf{L}^e + \mathsf{F}^e \mathsf{L}^p \left[\mathsf{F}^e\right]^{-1}, \tag{2.21}$$

where the elastic, L^e, and plastic, L^p, velocity gradients are defined by:

$$\mathsf{L}^e = \dot{\mathsf{F}}^e \left[\mathsf{F}^e\right]^{-1}, \ \mathsf{L}^p = \dot{\mathsf{F}}^p \left[\mathsf{F}^p\right]^{-1}. \tag{2.22}$$

The plastic stretch, D^p, and the plastic spin, W^p, tensors can also be defined as:

$$\mathsf{D}^p = \mathrm{sym}\left(\mathsf{L}^p\right), \ \mathsf{W}^p = \mathrm{skew}\left(\mathsf{L}^p\right). \tag{2.23}$$

The rotation of the plastic stretch, D^p, to the deformed configuration lead us to:

$$\mathsf{d}^p = \mathsf{R}^e \mathsf{D}^p \left[\mathsf{R}^e\right]^T = \mathsf{R}^e sym\left(\dot{\mathsf{F}}^p \left[\mathsf{F}^p\right]^{-1}\right) \left[\mathsf{R}^e\right]^T. \tag{2.24}$$

Following the formalism of thermodynamics with internal variables, an isotropic hyperelastic constitutive equation can be obtained:

$$\mathsf{T} = \bar{\rho} \frac{\partial \psi^e}{\partial \boldsymbol{\varepsilon}^e} = \mathsf{D}^e : \boldsymbol{\varepsilon}^e = \left[2G\mathsf{I} + \varsigma \left[\mathbf{I} \otimes \mathbf{I}\right]\right] : \boldsymbol{\varepsilon}^e \tag{2.25}$$

where $\mathsf{T} = J\boldsymbol{\sigma}$ is the Kirchhoff stress, $\bar{\rho}$ is the reference mass density, D^e denotes the fourth-order isotropic constant elastic tensor with $\mathbf{I}$ and I given in component form as $\mathbf{I}_{ij} = \delta_{ij}$ and $\mathsf{I}_{ijkl} = \frac{1}{2}\left[\delta_{ik}\delta_{jl} + \delta_{il}\delta_{jk}\right]$. Equation (2.25) is derived from the so-called Henky strain energy function, $\psi^e(\boldsymbol{\varepsilon}^e)$, which is generally accepted for a wide range of applications, given by,

$$\psi^e\left(\varsigma_1^e, \varsigma_2^e, \varsigma_3^e\right) = G\left[ln\left(\varsigma_1^e\right)^2 + ln\left(\varsigma_2^e\right)^2 + ln\left(\varsigma_3^e\right)^2 + \frac{1}{2}\varsigma \ ln\left(J^e\right)^2\right], \tag{2.26}$$

where G and ς are positive material constants (principal stretches and Bulk modulus, respectively) and $J^e = \varsigma_1^e \varsigma_2^e \varsigma_3^e$ is the Jacobian. The Eulerian logarithmic elastic strain tensor is employed as strain measure, which can be defined by,

$$\varepsilon^e = ln\left(\mathsf{V}^e\right) = \frac{1}{2} ln\left(\mathsf{B}^e\right) = \frac{1}{2} ln\left(\mathsf{F}^e [\mathsf{F}^e]^T\right), \tag{2.27}$$

where $ln(\cdot)$ denotes the tensorial logarithm of $(\cdot)$ and $\mathsf{B}^e = \left[\mathsf{V}^e\right]^2$ is the elastic Cauchy-Green strain tensor.

The evolution law for the plastic deformation gradient, F^p, adopted here, is defined in terms of the plastic multiplier, $\dot{\gamma}^p$, and of a generic plastic flow potential, $\psi\left(\mathsf{T}, A\right)$, expressed as a function of the Kirchhoff stress and the thermodynamic force set, A:

$$\mathsf{d}^p = \dot{\gamma}^p \frac{\partial \psi\left(\mathsf{T}, A\right)}{\partial \mathsf{T}}. \tag{2.28}$$

Combining the definition of the rotated plastic strech, Equation (2.24), with the constitutive law, Equation (2.28), and the assumption of zero plastic spin, $\mathsf{W}^p = 0$, the following evolution for the plastic deformation gradient can be obtained:

$$\dot{\mathsf{F}}^p \left[\mathsf{F}^p\right]^{-1} = \dot{\gamma}^p \left[\mathsf{R}^e\right]^T \frac{\partial \psi}{\partial \mathsf{T}} \mathsf{R}^e. \tag{2.29}$$

Table 2.1: General isotropic finite strain multiplicative elasto-plastic model.

1. Multiplicative decomposition of the deformation gradient, F,

   $$\mathsf{F} := \mathsf{F}^e \mathsf{F}^p.$$

   where the elastic, F^e, and the plastic parts, F^p, are obtained by performing the polar decompositions.

2. Evolution equations for F^p,

   $$\dot{\mathsf{F}^p} \left[\mathsf{F}^p\right]^{-1} = \dot{\gamma} \left[\mathsf{R}^e\right]^T \frac{\partial \Psi}{\partial \boldsymbol{\tau}} \mathsf{R}^e,$$

3. Hardening law,

   $$\dot{\boldsymbol{\alpha}} := \dot{\gamma}^p \mathsf{H}(\boldsymbol{\sigma}, A).$$

4. Loading/unloading criterion (plasticity set of Kuhn-Karush-Tucker conditions),

   $$\Phi \leq 0,\ \dot{\gamma}^p \geq 0,\ \dot{\gamma}^p \Phi = 0.$$

The evolution equation for the set of internal variables is given by,

$$\dot{\alpha} = \dot{\gamma}^p \mathsf{H}\left(\mathsf{T}, A\right), \tag{2.30}$$

where $\mathsf{H}\left(\mathsf{T}, A\right)$, represents a constitutive function and $\dot{\gamma}^p$ is the plastic multiplier. In order to define the onset of plastic flow, a general yield function, $\Phi\left(\mathsf{T}, A\right)$, is introduced. Together with the plastic multiplier, the yield function must comply with the standard complementarity relations (loading/unloading criterion),

$$\Phi \leq 0,\ \dot{\gamma}^p \geq 0,\ \dot{\gamma}^p \Phi = 0. \tag{2.31}$$

The finite strain hyperelastic-based model described here permits a convenient extension of the general isotropic infinitesimal elasto-plastic models to the finite strain range. The set of conditions described above are summarized in Table 2.1.

2.4.2 Material model

One of the most widespread phenomenological models for inelastic deformations is the classical von Mises model, [13, 16]. This model, which will be adopted here, assumes that plastic yielding occurs when the second invariant of the deviatoric stress tensor, $J_2 = \frac{1}{2}\left[\mathbf{s} : \mathbf{s}\right]$, reaches a critical value.

The elastic strain-energy, ψ^e, of this particular model can be decomposed as the sum of the distortional, ψ^e_d, and volumetric, ψ^e_v, contributions

$$\psi^e = \psi^e_d + \psi^e_v = \frac{1}{G} J_2 + \frac{1}{K} p^2, \tag{2.32}$$

with G and K representing, respectively, the shear and the bulk modulus. The deviatoric stress tensor, $\mathbf{s}$, can be expressed in terms of the Cauchy stress tensor and the hydrostatic pressure, $p = \frac{1}{3}\boldsymbol{\sigma} : \mathbf{I}$, as:

$$\mathbf{s}(\boldsymbol{\sigma}) = \boldsymbol{\sigma} - p\mathbf{I}. \tag{2.33}$$

The definition of the yield function for the von Mises criterion, is given by,

$$\Phi(\boldsymbol{\sigma}) = \sqrt{3J_2(\mathbf{s}(\boldsymbol{\sigma}))} - \sigma_y, \tag{2.34}$$

where σ_y is the uni-axial yield stress.

Taking the von Mises yield function, Equation (2.34), as the flow potential, the Prandtl-Reuss plastic flow rule is obtained:

$$\dot{\boldsymbol{\varepsilon}}^p = \dot{\gamma}^p \frac{\partial \Phi}{\partial \boldsymbol{\sigma}} = \dot{\gamma}^p \frac{\partial}{\partial \boldsymbol{\sigma}} \left[\sqrt{3J_2(\mathbf{s})}\right] = \dot{\gamma}^p \sqrt{\frac{3}{2}} \frac{\mathbf{s}}{\|\mathbf{s}\|}. \tag{2.35}$$

The assumption of isotropic strain hardening leads to the von Mises accumulated plastic strain, defined as

$$\bar{\boldsymbol{\varepsilon}}^p = \int_0^t \sqrt{\frac{2}{3}\left[\dot{\boldsymbol{\varepsilon}}^p : \dot{\boldsymbol{\varepsilon}}^p\right]}\, dt = \int_0^t \sqrt{\frac{2}{3}}\, \|\dot{\boldsymbol{\varepsilon}}^p\|\, dt. \tag{2.36}$$

By letting the uni-axial yield stress be a function of the accumulated plastic strain, a von Mises isotropic strain hardening model is obtained,

$$\boldsymbol{\sigma}_y = \boldsymbol{\sigma}_y(\bar{\boldsymbol{\varepsilon}}^p). \tag{2.37}$$

The von Mises model defined by the elastic potential, Equation (2.32), the yield function, Equation (2.34), and the flow potential – which is the von Mises yield function – can be extended to finite strains by adopting the same functional structure described in Subsection 2.4.1.

Chapter 3

Fretting wear phenomena

This Chapter introduces the energy-based formulation employed for solving the frictional contact problem. In Section 3.1, a brief overview on the principal wear mechanics definitions and fretting formulations is presented. In Section 3.2, the Dissipated energy method is detailed. The material removal strategy is the subject of Section 3.3.

3.1 Wear mechanics

The interface of solid bodies under interaction often displays complex physical phenomena. Surfaces in motion and in contact are bound to friction, which may lead to volume variations due to Wear and/or Adhesion. Moreover, the interface may present a material flux caused by chemical reactions such as ion-coupled electron transfer or due to mechanical processes like welding.

fretting wear is defined as the degeneration process of a solid body under the effects of frictional forces. This mechanical material removal from a body may occur in several different ways [46, 65]. The first and most usual one is known as Abrasive wear, which repeated in a cyclical way is defined as fretting wear [80]. In this case third bodies are formed due to detachment of particles from the contact surface. A second case occurs when material is transferred from a body to another, which is referred as Adhesive wear. In both these situations, the contact forces can also lead to crack nucleation, which may initiate another failure mechanism known as fretting fatigue [79]. Corrosive wear may also occur if materials prone to chemically react are in place. Another distinction, made within wear mechanisms, is the fretting regime. According with Vingsbo and Soderberg [78], fretting can be divided into three regimes and one intermediate phase: stick regime, mixed stick-slip regime, gross slip regime and reciprocating sliding regime. The fretting regime is identified by a fretting map, which shows the effect of the friction force *versus* the sliding amplitude. The influence of the fretting regime acts on the wear scar profile, on the worn volume and also on the chemical composition of the scar and debris.

The two most commonly used methods to predict the wear kinetics of a contact problem are the so-called *Archard* method [2] and the Dissipated energy method [29]. The Archard method uses the input variables from the contact setting (i.e. pre-

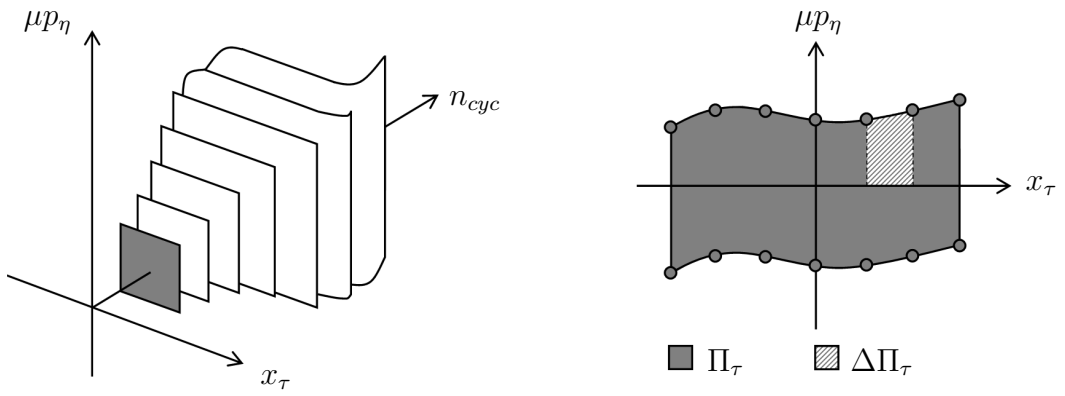

(a) fretting map. (b) Friction trace.

Figure 3.1: Energy dissipated by the frictional force.

scribed normal load, displacement amplitude, etc.) to calculate the wear loss. Therefore, the Archard coefficient becomes dependent of the initial problem conditions. On the other hand, the Dissipated energy method uses the measurements obtained from the contact problem. The frictional force is measured at every increment of displacement, which at the end of a loading cycle enables the creation of the so-called Friction trace. The Friction trace represents the total amount of energy lost in a given loading cycle, see Figure 3.1(b). This energy is later related to the material loss using an independent coefficient: the energy wear coefficient. After many loading cycles are performed, a loading history of dissipated energy is created. This history is known as the fretting map depicted in Figure 3.1(a).

3.2 Dissipated energy method

The dissipated energy method for prediction of wear postulates [26, 66] that the material loss, w, is proportional to the energy lost due to friction, in the following way,

$$w = \alpha_w \Pi_w. \tag{3.1}$$

where the energy wear coefficient, α_w, is a material parameter obtained during the same procedure usually employed to evaluate the coefficient of friction of a specific pair of surfaces. Π_w is the total energy dissipated by friction over the n_{cyc} loading cycles,

$$\Pi_w = \sum_{i=1}^{n_{cyc}} \{\Pi_\tau\}_i \,, \tag{3.2}$$

where, Π_τ, is the work done by the frictional forces when loading cycle i is performed.

The main advantage of this method relies on the possibility of using the same wear coefficient for any normal load, displacement amplitude, or load frequency even if they change during the simulation. Moreover, the influence of the wear conditions are accounted as the energy is dissipated through the process of sliding

and it's evolution is obtained knowing only the time history of displacement and the frictional force (i.e fretting map).

It is important to emphasize that this proposed implementation of Dissipated energy method assumes that the friction coefficient remains constant during the wear evaluation. Only changes of regime state (i.e stick or slip) are considered. Moreover, it is assumed that the frequency of the loading cycles are low enough such that the thermomechanical effects can be disregarded.

3.3 Material removal strategy

At the point where the quantity of material lost is know, a suitable procedure for updating the contact surfaces must be introduced. The most coarse strategy for updating the finite element mesh would be removing the volume from the contact elements. However, since the fretting mechanism is a recurring process that often leads to the loss of a substantial quantity of material, this could be a constant source of computational instability. In particular, the finite elements at hand could be completely worn out of the structure, as seen in Figure 3.2. The picture shows a cubic structure being worn to 50% of it's initial height. In this scenario, the absence of mesh treatment would lead to the complete removal of both first and second finite element layers. From a finite element perspective, there are several strategies that can be adopted for dealing with such a problem. Many of these are based on the concept of remeshing.

3.3.1 Shape update methods

The available remeshing methods are mainly focused in the treatment of distortion and high level of deformation, often creating new elements by dividing the existing ones. From a contact formulation viewpoint, the removal or the creation of new elements is a very costly and inefficient strategy. The new contact candidates would add to both time search and matrices size. Moreover, since the process of remeshing must happen during the iterative solution of the problem (a requirement for precise computation of fretting Wear) the convergence rate of the solution would also be impacted. Additionally, since the contact interface is usually a rather small part of the whole structure, the use of such methods would lead to an unnecessary increase in the computational cost. In order to circumvent these shortcomings, a local topography update working in synergy with the contact search might be more appropriate.

Therefore, ruling out the remeshing schemes that generate new elements, the methods that remain are nodal re-collocations methods and Arbitrary Lagrangean-Eulerian (ALE) strategies [3, 8]. A standard nodal re-collocation solution, when employed throughout a whole solid body, would produce results similar to the ones depicted in Figure 3.3. In this case, the wear depth is shared by all layers, which helps to preserve the number of elements in the structure and the good aspect ratio of the elements over the contact surface. This is basically the same concept employed to average displacements in a given mesh. However, by adopting this

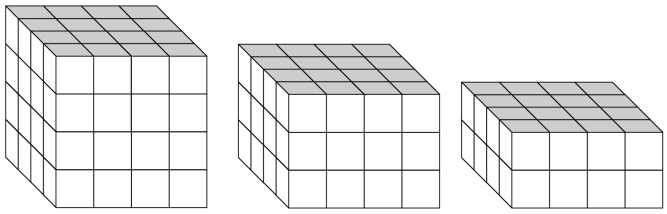

Figure 3.2: Complete removal of finite elements.

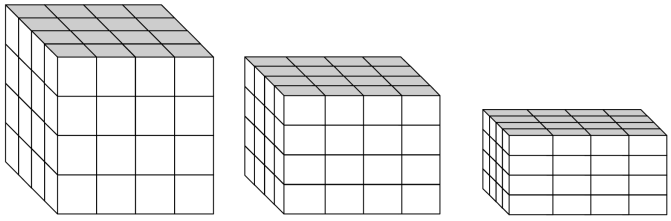

Figure 3.3: Wear depth equally balanced over all layers.

method, properties like effective plastic strain on the contact elements would no longer be precisely described.

A third scenario is the adaptive balance of the wear depth. In this case, the aspect ratio of the finite elements and it's relative position in regard to the interface have direct correlation with the material lost in the layer under consideration, see Figure 3.4.

Throughout this work, an adaptive approach coupled with a *Wear Box* concept is favored.

3.3.2 Wear box concept

In this approach, a bounding box surrounding an appropriate number of finite elements is defined as the area of interest, such as the finite elements highlighted in blue Figure 3.5. For instance, these highlighted finite elements represent both the set contact candidates elements (elements at the the contact interface) and the element passive to the wear balance procedure. The material lost, w, defined in Equation (3.1), is shared by the n_e^{box} finite elements defined within the wear box, as

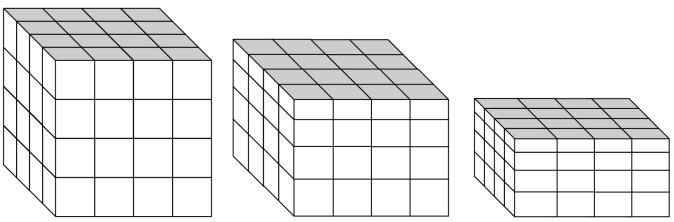

Figure 3.4: Adaptive balance of the worn volume.

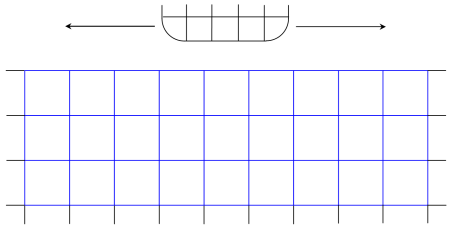

Figure 3.5: Wear Box.

follows,

$$w = \sum_{e=1}^{n_e^{box}} w_e. \tag{3.3}$$

The subdivision of the material lost among the finite elements in contact is guided by the normal reactions on each contact node j, such that the element worn volume, w_e, of each finite element, e, has a direct dependency of the contact load. This procedure assures that finite elements experiencing higher load condition will display higher levels of degeneration while preserving their aspect ratio. Figure 3.6 shows the problem geometry undergoing the material removal balance procedure followed by the shape update. In this work, focused is given to quadrilateral and hexahedral finite elements. Nevertheless, the concepts employed here can be extended to any finite element type. The weighting balance of the material lost is given by,

$$w_e = \left[\frac{\sum_{j=1}^{n_{nod}} \{p_\eta\}_j}{\sum_{e=1}^{n_e} \sum_{j=1}^{n_{nod}} \{p_\eta\}_j} \right] w. \tag{3.4}$$

where n_{nod} are the number of contacting nodes and n_e represents the number of elements within the wear box.

In addition, due to the nature of the finite element type chosen to discretize the contacting bodies (quadrilaterals or hexahedrals elements in this case), the element worn volume must respect a second geometrical rule,

$$w_e = \left[\frac{\sum_{j}^{n_{nod}^e} h_j}{n_{nod}^e} \right] A_e. \tag{3.5}$$

where n_{nod}^e is the number of nodes of the element e. The scalar A_e represents the section area (or the length, in case of two-dimensional meshes) of element e. The wear depth, h_j, is also balanced using the same procedure employed in Equation (3.4),

$$\frac{h_j}{\sum_{e=1}^{n_e} \sum_{j=1}^{n_{nod}^{adj}} h_j^e} \equiv \frac{\{p_\eta\}_j}{\sum_{e=1}^{n_e} \sum_{j=1}^{n_{nod}^{adj}} \{p_\eta\}_j^e}. \tag{3.6}$$

where n_{nod}^{adj} is the number of adjacents nodes of node j. Moreover, combination of Equations. (3.4 - 3.6) yields an expression for wear depth, h_j, in terms of the normal pressure, $\{p_\eta\}_j$, and the material lost, w,

$$h_j = \frac{w \{p_\eta\}_j}{n^e A^e \sum_{e=1}^{n_e} \sum_{j=1}^{n_{nod}^{adj}} \{p_\eta\}_j^e}. \tag{3.7}$$

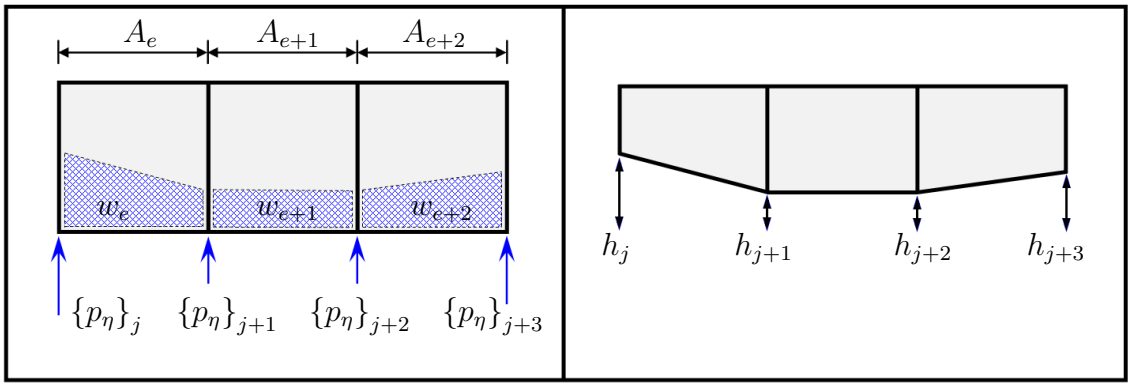

Figure 3.6: Removal of worn area.

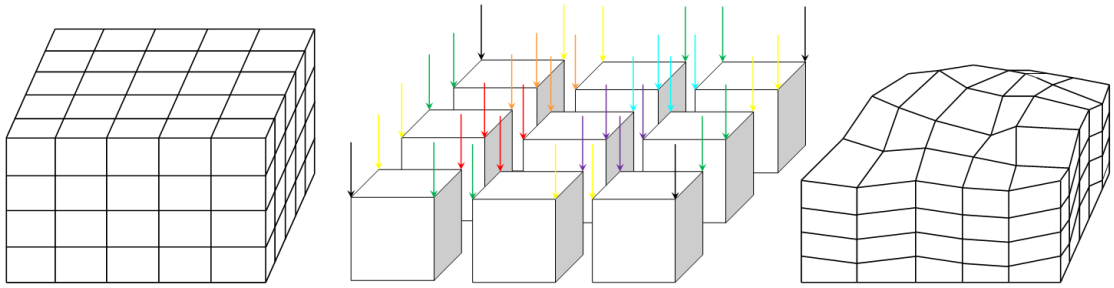

Figure 3.7: Topography update of a surface under a wide spectrum of forces.

3.3.3 Aspect ratio algorithm

Following the evaluation of the wear depth, the topography of the contact surface must be updated. However, in order to maintain the aspect ratio of the worn elements in the contact zone, an algorithm for preserving a minimal set of dimensions is required. The first item that is analyzed when enforcing the material removal is the ratio between the finite element height and its cross-sectional area. Furthermore, once a volumetric condition is met, the balance procedure is enabled. Herein, the desired aspect ratio for the contact elements must respect the conditions stated at Table 3.1. This set of new methods for performing the update of the geometrical shape of the contact elements under fretting wear results in a very robust framework. The wear height is computed in a point-wise manner while still considering the repercussion on the adjacent nodes. Therefore, complex topographies, such as the one depicted in Figure 3.7, can be obtained a very small impact on the overall solution the problem.

Table 3.1: Wear volume balance procedures.

IF $\bar{h}_e/(A_e^i) > 0.1$ **THEN** Remove the allowed quantity from layer i,

$h_j^i = \bar{h}_e - 0.1A_e^i$,

ELSE

1. Keep the required wear depth,

   $r_j^i = h_j^i$,

2. Remove the allowed quantity, h_j^i, from layer i,

   $h_j^i = \bar{h}_e - 0.1A_e^i$,

3. Remove the remaining wear depth from the elements at the lower layers (i+1), according with the balance method employed,

   Evenly balanced

   $h_j^{i+1} = r_j^i/n_{lrs}$,

   Adaptive method

   $h_j^{i+1} = r_j^i[n_{lrs} - i - 1]/2n_{lrs}$,

   where $\bar{h}_e$ is the average height of element e and n_{lrs} is the number of layers within the "wear box".

END

Chapter 4

Numerical formulation

In this chapter the weak and discrete forms of the frictional contact problem with wear, presented in Chapters 2 and 3 are derived. The Section 4.1 is concerned with the virtual work done by the tractions, the contact constraints and the dissipated energy. The basic steps for performing an incremental solution are shown in the Section 4.2. The spatial discretization of the solid bodies is covered in the third section. Lastly, a summary of the discretized is problem is given in Section 4.4.

4.1 Weak form

Following the definition of an energy-based problem, a variational method is employed to obtain the weak form of the contact virtual work together with the KKT conditions. In particular, for solving the Boundary Value Problem, Equation (2.3), the principle of virtual work is applied. However, in order to do so, a vector valued solution space and a weighting space must be introduced. The vector valued solution space, $\mathbf{u} \subset \{\mathbf{u}^s \cup \mathbf{u}^m\}$, containing the admissible displacement field, must be defined on the *Sobolev* space of functions, H^1, such that,

$$\mathcal{U}^i := \left\{ \mathbf{u}_j^i \in \left[H^1 \left(\Omega^i \right) \right] \ : \ \mathbf{u}_j^i \big|_{\Gamma_D^i} = \mathbf{u}_j^i \right\}, \tag{4.1}$$

while the weighting space for the incremental displacements, $\delta\mathbf{u}$, is given by,

$$\mathcal{V}^i := \left\{ \delta\mathbf{u}_j^i \in \left[H^1 \left(\Omega^i \right) \right] \ : \ \delta\mathbf{u}^i \big|_{\Gamma_D^i} = 0 \right\}. \tag{4.2}$$

Furthermore, by employing test functions $\mathbf{v}^i \in H^1(\Omega^i)$ one can state the energy problem, in terms of the displacement field $\mathbf{u}$, as follows,

$$\begin{aligned} \delta\Pi \left(\mathbf{u}, \delta\mathbf{u} \right) =& \delta\Pi_{\text{int,ext}} \left(\mathbf{u}, \delta\mathbf{u} \right) + \delta\Pi_c \left(\mathbf{u}, \delta\mathbf{u} \right) \\ &+ \delta\Pi_w \left(\mathbf{u}, \delta\mathbf{u} \right) = 0, \ \forall \ \left\{ \delta\mathbf{u}^i \in \mathcal{V}^i \right\}, \end{aligned} \tag{4.3}$$

where $\delta\Pi_{\text{int,ext}} \left(\mathbf{u}, \delta\mathbf{u} \right)$ is the standard virtual work from the internal and external forces, $\delta\Pi_c \left(\mathbf{u}, \delta\mathbf{u} \right)$, represents the contact virtual work and $\delta\Pi_w \left(\mathbf{u}, \delta\mathbf{u} \right)$ is the potential energy related to the material removed from the physical system. The former

can be computed for each body as:

$$\begin{aligned}\delta\Pi^i_{\text{int,ext}}\left(\mathbf{u}^i,\delta\mathbf{u}^i\right) = &\int_{\varphi\left(\Omega^i_0\right)} \boldsymbol{\sigma}^i\cdot\operatorname{grad}\left(\delta\mathbf{u}^i\right)\ d\Omega\\ &-\int_{\varphi\left(\Omega^i_0\right)} \mathbf{b}^i\cdot\delta\mathbf{u}^i\ d\Omega\\ &-\int_{\varphi\left(\Gamma^i_N\right)} \hat{\mathbf{t}}^i\cdot\delta\mathbf{u}^i\ d\gamma_N,\end{aligned} \tag{4.4}$$

The contact virtual work, $\delta\Pi_c\left(\mathbf{u},\delta\mathbf{u}\right)$, is obtained as the integral – over the *slave side* – of the work done by the contact traction $\mathbf{t}^s_c$, by applying a balance of linear momentum at the contact interface, $\mathbf{t}^s_c d\gamma^s_c = \mathbf{t}^m_c d\gamma^m_c$, as follows,

$$\delta\Pi_c\left(\mathbf{u},\delta\mathbf{u}\right) = -\int_{\gamma^s_c}\mathbf{t}^s_c\cdot\left[\delta\mathbf{u}^s-\delta\mathbf{u}^m\right]d\gamma^s_c. \tag{4.5}$$

Since in the Dissipated energy method is related to the energy lost due to wear, $\delta\Pi_w$, as the energy dissipated by the frictional force, from Equation (3.2) it is possible to write a weak form for the Wear energy, such that,

$$\delta\Pi_w\left(\mathbf{u},\delta\mathbf{u}\right) = \int_{\gamma^s_c}\mu\left[\boldsymbol{\eta}\mathbf{t}^s_c\right]\cdot\left[\delta\mathbf{u}^s-\delta\mathbf{u}^m\right]d\gamma^s_c \leq 0. \tag{4.6}$$

The first step towards the definition of the weak form of the contact conditions is attained by replacing the normal contact pressure and the tangential tractions by lagrangian multipliers, such that,

$$\boldsymbol{\lambda} = -\mathbf{t}^s_c\ \because\ \lambda_n = -p_\eta,\ \lambda^\xi_\eta = t^\xi_\tau,\ \lambda^\chi_\eta = t^\chi_\tau. \tag{4.7}$$

Therefore, a modified set of KKT conditions can be rewritten in terms of the lagrangian multipliers, as follows,

$$g(\mathbf{X}^s,t)+h(\mathbf{X}^s,t)\geq 0,\ \lambda_\eta\geq 0,\ \lambda_\eta\left[g(\mathbf{X},t)+h(\mathbf{X}^s,t)\right]=0. \tag{4.8}$$

Same procedure can be applied to the Coulomb's function, which yields,

$$\mathfrak{F} := |\lambda_\tau| - \mu(x,y,z)|\lambda_\eta| \leq 0. \tag{4.9}$$

Furthermore, the strong pointwise conditions stated in Equation (4.8) can be replaced by a weak integral condition, over $\delta\gamma^s_c$,

$$\delta g = \int_{\gamma^s_c}\delta\lambda_\eta\left[g(\mathbf{X},t)\right]\ d\gamma^s_c,\ \forall\ \left\{\delta\lambda_\eta\in\mathcal{M}\right\}, \tag{4.10}$$

where $\mathcal{M}$ represents the chosen space for the lagrangian multipliers. The weak form of the contact conditions, in the tangential direction, is given by,

$$\int_{\gamma^s_c}\delta\lambda_\tau\left[\left(\vartheta_\tau(\mathbf{X},t)-\beta\lambda_\tau\right)\right]\ d\gamma^s_c,\ \forall\ \left\{\delta\lambda_\tau\in\mathcal{M}\right\}. \tag{4.11}$$

Next, by introducing the lagrangian multipliers into Equation (4.5) and Equation (4.6) yields the following expression for the contact virtual work with wear,

$$\delta\Pi_c\left(\mathbf{u},\delta\mathbf{u},\boldsymbol{\lambda}\right)+\delta\Pi_w\left(\mathbf{u},\delta\mathbf{u},\boldsymbol{\lambda}\right)=\int_{\gamma_c^s}\left[\boldsymbol{\lambda}-\mu\boldsymbol{\lambda}\cdot\boldsymbol{\eta}\right]\cdot\left[\delta\mathbf{u}^s-\delta\mathbf{u}^m\right]d\gamma_c^s. \tag{4.12}$$

Finally, by introducing the dissipated energy, $\delta\Pi_w$ into the definition of wear volume, w, it's weak form is obtained,

$$\delta w=\alpha_w\left\{\delta\Pi_w\right\}=\alpha_w\int_{\gamma_c^s}\mu\lambda_\eta[\delta\mathbf{u}^s-\delta\mathbf{u}^m]d\gamma_c^s. \tag{4.13}$$

4.2 Incremental form

4.2.1 Numerical integration algorithm

The solution of the constitutive model, described in Section 2.4, defined by the corresponding rate constitutive equations and a set of initial conditions is not usually known for complex deformation paths. Therefore, the use of a numerical algorithm for integration of the rate constitutive equations is essential.

Algorithms based on the operator split methodology are particularly suitable for numerical integration of the evolution problem and have been widely used in computational plasticity, [13,16]. Here, such an operator split method is used in the numerical integration of the elasto-plastic constitutive equations. An essential point in the derivation of the algorithm is the exponential approximation employed in the discretization of the plastic flow rule, in the plastic corrector stage, which was firstly employed in the computational literature by Webber and Anand [81]. It leads to the following incremental evolution equation:

$$\begin{aligned}\mathsf{F}_{n+1}^p&=\exp\left(\Delta\gamma^p\left[\mathsf{R}_{n+1}^e\right]^T\left.\frac{\partial\Phi}{\partial\mathsf{T}}\right|_{n+1}\mathsf{R}_{n+1}^e\right)\mathsf{F}_n^p\\&=\left[\mathsf{R}_{n+1}^e\right]^T\exp\left(\Delta\gamma^p\left.\frac{\partial\Phi}{\partial\mathsf{T}}\right|_{n+1}\right)\mathsf{R}_{n+1}^e\mathsf{F}_n^p.\end{aligned} \tag{4.14}$$

In addition, a one step backward Euler scheme is used to integrate the evolution equation for the internal variable,

$$\bar{\varepsilon}_{n+1}^p=\bar{\varepsilon}_n^p-\Delta\gamma^p\left.\frac{\partial\Phi}{\partial\mathsf{T}}\right|_{n+1}. \tag{4.15}$$

It can be shown that the approximation of Equation (4.14) results in the following simpler update formula in terms of the logarithm eulerian strain tensor:

$$\boldsymbol{\varepsilon}_{n+1}^e=\boldsymbol{\varepsilon}_{n+1}^{e\ \mathrm{trial}}-\Delta\gamma^p\left.\frac{\partial\Phi}{\partial\mathsf{T}}\right|_{n+1}, \tag{4.16}$$

which is valid whenever the elastic right Cauchy-Green tensor $\mathsf{C}_{n+1}^{e\ \mathrm{trial}}=\left[\mathsf{F}_{n+1}^{e\ \mathrm{trial}}\right]^T\mathsf{F}_{n+1}^{e\ \mathrm{trial}}$ and $\left.\frac{\partial\Phi}{\partial\mathsf{T}}\right|_{n+1}$ commute. Using Equation (4.16) and imposing the elastic law at t_{n+1},

the following expression for the stress tensor consistent with the exponential approximation, Equation (4.14), is obtained,

$$\mathsf{T}_{n+1} = \mathsf{D}^e : \left[\boldsymbol{\varepsilon}^{e\ \mathrm{trial}}_{n+1} - \Delta\gamma^p \left. \frac{\partial \Phi}{\partial \mathsf{T}} \right|_{n+1} \right]. \tag{4.17}$$

Consequently, the Cauchy stress is given by:

$$\boldsymbol{\sigma}_{n+1} = \mathsf{R}^e_{n+1} \mathsf{T}_{n+1} \left[\mathsf{R}^e_{n+1} \right] / \det \left(\mathsf{U}^e_{n+1} \right). \tag{4.18}$$

Therefore, due to the use of logarithmic strains to describe elasticity together with the exponential approximation, the stress updating procedure can be written in the same format as the classical return mapping schemes of infinitesimal elastoplasticity, see Ortiz and Popov [56], Simo & Hughes [70], Souza Neto et al. [16]. Here, the numerical integration of the small strain von Mises constitutive equations was undertaken with the backward Euler scheme.

4.2.2 Incremental boundary value problem

Assuming that the values of F^p and $\bar{\varepsilon}^p$ are known at a certain time t_n, the deformation φ_{n+1} at a subsequent time t_{n+1} will determine uniquely the value of $\boldsymbol{\sigma}$ at time t_{n+1}, through the integration algorithm. This defines the incremental constitutive relation:

$$\boldsymbol{\sigma}_{n+1} = \hat{\boldsymbol{\sigma}} \left(\mathsf{F}^p_n, \bar{\varepsilon}^p_n, \varphi_{n+1} \right). \tag{4.19}$$

Including Equation (4.19) in the weak form of the equilibrium, the incremental boundary value problem can be stated as follows: given F^p and $\bar{\varepsilon}^p$ at time t_n and given the body force and surface traction fields at time t_{n+1}, find the kinematically admissible configuration $\varphi\left(\Omega_0\right)\big|_{n+1}$, such that,

$$\begin{aligned} \sum_i^{s,m} \Bigg\{ & \int_{\varphi\left(\Omega_0^i\right)\big|_{n+1}} \hat{\boldsymbol{\sigma}}^i \cdot \operatorname{grad}\left(\delta \mathbf{u}^i\right) \, d\Omega - \int_{\varphi\left(\Omega_0^i\right)\big|_{n+1}} \mathbf{b}^i_{n+1} \cdot \delta \mathbf{u}^i \, d\Omega \\ & - \int_{\varphi\left(\Gamma_N^i\right)\big|_{n+1}} \hat{\mathbf{t}}^i_{n+1} \cdot \delta \mathbf{u}^i \, d\gamma_N \Bigg\} - \int_{\varphi(\Gamma_c^s)|_{n+1}} \boldsymbol{\lambda}_{n+1} \left[\delta \mathbf{u}^s - \delta \mathbf{u}^m \right] \, d\gamma_c^s \\ & = 0, \ \forall \ \left\{ \delta \mathbf{u}^i \in \mathcal{V}^i \right\}. \end{aligned} \tag{4.20}$$

The equations employed to discretize the body's geometry, the kinematic equations, the inequalities related to the contact constraints and the virtual work variables in Equation (4.3), are the subject of the following section.

4.3 Spatial discretization

Herein, the Finite Element method is employed for the spatial discretization of the variables contained in the virtual work, Equation (4.3), and the variables in the enforced contact constraints, Equations. (4.8-4.11). Two distinct approaches are undertaken for each spatial dimension and they are detailed in the following sections.

4.3.1 Finite elements for 2D analysis

Two types of finite elements were chosen for the analysis of two-dimensional problems. The first one is the 2D bi-linear F-bar finite element [15]. This finite element is know for it's improved behavior under nearly isochoric deformations. An F-bar element is obtained from the standard finite element by replacing the volumetric component of the deformation gradient, F, by the volumetric component of the deformation gradient at the centroid of the element, $\{\mathsf{F}_0\}_v$. Therefore, the F-bar deformation gradient, at a specific Gauss point, is the product of the isochoric component of F with the volumetric component of F_0:

$$\mathsf{F}_{bar} = \mathsf{F}_{iso}\,\{\mathsf{F}_0\}_v = \left[\frac{det(\mathsf{F}_0)}{det(\mathsf{F})}\right]^{1/3}\mathsf{F}. \tag{4.21}$$

Particularly important in the present context is the fact that this element can be used with any material model, can produce solutions with reasonably sized meshes, is able to avoid volumetric locking and is suitable to capture strains locally. The F-bar element has got exactly the same shape functions as the conventional 4-noded quadrilateral finite element (*quad4fbar*), which are displayed in Figure 4.1a. The second finite element type chosen for 2D analysis was the standard isoparametric 8-noded element (*quad8*). The additional number of degrees of freedom, in this particular element, allows for a better enforcement of the contact constraints and balance of the wear depth. Geometry and shape function for the quad8 element are detailed in Figure 4.1b.

4.3.2 Finite elements for 3D analysis

For the three-dimensional case, the 8-noded tri-linear F-bar hexahedral element (*hexa8fbar*) is employed for the discretization of the solid bodies, $\Omega_0^i, i = s, m$. This finite element can provide accurate results for both large inelastic contact problems and fretting wear problems therefore being a standard choice for 3D analysis. The geometry as well the shape functions for this element type are depicted in Figure 4.1c.

4.3.3 Geometrical interpolations

Having defined the finite element type to be employed, the geometrical coordinates, $\mathbf{x}$, are approximated by interpolation of the nodal coordinates using the given shape

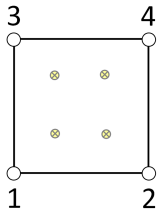

$$N_1 = \tfrac{1}{4}(1-\xi)(1-\eta);\quad N_2 = \tfrac{1}{4}(1+\xi)(1-\eta);$$
$$N_3 = \tfrac{1}{4}(1+\xi)(1+\eta);\quad N_4 = \tfrac{1}{4}(1-\xi)(1+\eta);$$

(a) 2D F-bar element - *quad4fbar*

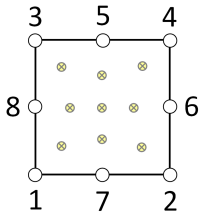

$$N_1 = \tfrac{-1}{4}(1-\xi)(1-\eta)(1+\xi+\eta);\quad N_2 = \tfrac{-1}{4}(1+\xi)(1-\eta)(1-\xi+\eta);$$
$$N_3 = \tfrac{-1}{4}(1+\xi)(1+\eta)(1-\xi-\eta);\quad N_4 = \tfrac{-1}{4}(1-\xi)(1+\eta)(1+\xi-\eta);$$
$$N_5 = \tfrac{1}{2}\left(1-\xi^2\right)(1-\eta);\ N_6 = \tfrac{1}{2}(1+\xi)\left(1-\eta^2\right);$$
$$N_7 = \tfrac{1}{2}\left(1-\xi^2\right)(1+\eta);\ N_8 = \tfrac{1}{2}(1-\xi)\left(1-\eta^2\right)$$

(b) 2D 8-Noded element - *quad8*

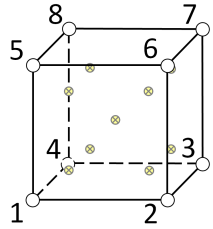

$$N_1 = \tfrac{1}{8}(1-\xi)(1-\eta)(1-\zeta);\quad N_2 = \tfrac{1}{8}(1+\xi)(1-\eta)(1-\zeta);$$
$$N_3 = \tfrac{1}{8}(1+\xi)(1+\eta)(1-\zeta);\quad N_4 = \tfrac{1}{8}(1-\xi)(1+\eta)(1-\zeta);$$
$$N_5 = \tfrac{1}{8}(1-\xi)(1-\eta)(1+\zeta);\quad N_6 = \tfrac{1}{8}(1+\xi)(1-\eta)(1+\zeta);$$
$$N_7 = \tfrac{1}{8}(1+\xi)(1+\eta)(1+\zeta);\quad N_8 = \tfrac{1}{8}(1-\xi)(1+\eta)(1+\zeta);$$
$$\xi = [-1,+1];\ \eta = [-1,+1];\ \zeta = [-1,+1].$$

(c) 3D F-bar element - *hexa8fbar*

Figure 4.1: Finite elements types and shape functions.

functions, $N^i(\boldsymbol{\xi}^i)$,

$$\mathbf{x}^s\big|_{\{\Gamma_c^s\}} \approx \{\mathbf{x}^s\}^h\Big|_{\{\Gamma_c^s\}^h} = \sum_{k=1}^{n_s} \{N_k^s(\boldsymbol{\xi}^s)\mathbf{x}_k^s\} \ , \tag{4.22}$$

$$\mathbf{x}^m\big|_{\{\Gamma_c^m\}} \approx \{\mathbf{x}^m\}^h\Big|_{\{\Gamma_c^m\}^h} = \sum_{l=1}^{n_m} \{N_l^m(\boldsymbol{\xi}^m)\mathbf{x}_l^m\} \ , \tag{4.23}$$

while the displacement interpolations are obtained from the nodal displacements, $\mathbf{d}$, in a similar way,

$$\mathbf{u}^s\big|_{\{\Gamma_c^s\}} \approx \{\mathbf{u}^s\}^h\Big|_{\{\Gamma_c^s\}^h} = \sum_{k=1}^{n_s} \{N_l^s(\boldsymbol{\xi}^s)\mathbf{d}_k^s\} \ , \tag{4.24}$$

$$\mathbf{u}^m\big|_{\{\Gamma_c^m\}} \approx \{\mathbf{u}^m\}^h\Big|_{\{\Gamma_c^m\}^h} = \sum_{l=1}^{n_m} \{N_l^m(\boldsymbol{\xi}^m)\mathbf{d}_l^m\} \ , \tag{4.25}$$

where n_s and n_m denote the number of nodes on the slave and master boundary side, respectively. The slave and master element shape functions are represented by N^i and the surface element parametrization, $\boldsymbol{\xi}$, as defined by,

$$\boldsymbol{\xi}^i = \xi^i, \ \forall \ \Omega_0^i \subset \mathbb{R}^2, i = s, m, \tag{4.26}$$

$$\boldsymbol{\xi}^i = (\xi^i, \eta^i), \ \forall \ \Omega_0^i \subset \mathbb{R}^3, i = s, m. \tag{4.27}$$

The solution of the Boundary Value Problem, Equation (2.3), is undertaken by approximating $\mathbf{u}$ with a virtual displacements vector $\mathbf{u}^h \in \mathcal{U}^h$, where $\mathcal{U}^h = \text{span}\{N_k\}$. The discretized space of test functions must then fulfill the condition $\mathbf{u}^h = \overline{\mathbf{u}}^h$ on the Dirichlet boundary $\Gamma_{_D}$.

4.3.4 Lagrange multipliers discretization

Following a mortar formulation, the set of lagrangian multipliers $\boldsymbol{\lambda}$ is approximated by a discretized space $\mathcal{M}^h = \text{span}\left\{\boldsymbol{\phi}_j(\boldsymbol{\xi}^s)\right\}$, where ϕ_j is chosen to be the so-called dual shape functions [83]. Consequently, the discretized form of the lagrangian multipliers is defined as,

$$\boldsymbol{\lambda}^h = \sum_{j=1}^{n_s} \left\{\boldsymbol{\phi}_j\left(\boldsymbol{\xi}^s\left(\mathbf{X}\right)\right)\mathbf{z}_j\right\}, \tag{4.28}$$

where, $\mathbf{z}_j$ is the lagrangian multiplier on the slave node $j = \{1, ..., n_s\}$ while n_s represents the number of nodes on the slave side. The dual shape functions must fulfill the so-called bi-orthogonality condition, as follows,

$$\int_{\{\gamma_c^s\}^h} \boldsymbol{\phi}_j N_k^s\left(\xi^s(\mathbf{X}^s)\right) \ d\gamma_c^s = \delta_{jk} \int_{\{\gamma_c^s\}^h} N_k^s\left(\xi^s(\mathbf{X}^s)\right) \ d\gamma_c^s \ , \tag{4.29}$$

where δ_{jk} is the Kronecker delta. It is important to remark that, for practical reasons, the bi-orthogonality condition is defined on the slave side boundary, γ_c^s.

In the context of the *quad4fbar* element, since the Jacobian of the linear shaped mortar segments is constant, the following piecewise linear dual shape functions can be obtained from Equation 4.29,

$$\boldsymbol{\phi}_1 = \frac{1}{2}\left(1 - 3\xi\right), \ \boldsymbol{\phi}_2 = \frac{1}{2}\left(1 + 3\xi\right). \tag{4.30}$$

The *quad8* element have a non-constant element Jacobian determinant. Therefore, it's associated dual shape functions are element specific [84]. In the context of two-dimensional analysis of an undistorted element, the quadratic dual shape functions can be defined as,

$$\boldsymbol{\phi}_1 = \frac{1}{4}\left[5\xi^2 - 2\xi - 1\right], \ \boldsymbol{\phi}_2 = \frac{1}{2}\left[3 - 5\xi^2\right], \ \boldsymbol{\phi}_3 = \frac{1}{4}\left[5\xi^2 + 2\xi - 1\right]. \tag{4.31}$$

while in the general cases, it can be obtained by solving the following equation system:

$$\boldsymbol{\phi}_j(\xi,\eta) = a_{jk} N_k^s(\xi,\eta), \ \mathbf{A}_e = \mathbf{D}_e \mathbf{M}_e^{-1} = [a_{jk}] \in \mathbb{R}^{m_e^s \times m_e^s} \tag{4.32}$$

where m_e^s, represents the number of nodes in this specific element e facet. While, $\mathbf{D}_e = \delta_{jk} \int_e N_k^s(\xi,\eta) J(\xi,\eta) \ d_e$ and $\mathbf{M}_e = \int_e N_j^s(\xi,\eta) N_k^s(\xi,\eta) J(\xi,\eta) \ d_e$ are, respectively, the element entry of the non-mortar and the mortar matrices, which will be further explained in the following sections.

A similar situation applies to the 3D case. The first-order interpolation of the *hexa8fbar* element leads to *quad4* surface facets which may have a non-constant element Jacobian determinant. Thus, the solution of Equation (4.32) is also required.

4.3.5 Evaluation of the mortar integrals for 2D analysis

The segmentation method adopted here was proposed by [88]. It is based in a continuous normal field, defined on the slave (i.e. non-mortar) surface, which is used to obtain both sets of projections. However, rather than using first order mortar elements we employ second order finite elements and a quadratic dual basis for the lagrangian multipliers, Fig. 4.2 illustrates the segments generated by the continuous field of normal vectors in this specific condition.

To find a projection of a slave node with coordinates, $\mathbf{x}_1^s$, onto a master element, with nodal coordinates x_1^m and x_2^m, one must fulfill the following inner product,

$$\left[N_1^m\left(\xi^m\right)\mathbf{x}_1^m + N_2^m(\xi^m)\mathbf{x}_2^m - \mathbf{x}_1^s\right] \times \boldsymbol{\eta}_1^s = \mathbf{0}, \tag{4.33}$$

where $N_{1,2}^m$ are shape functions defined on the master side local coordinate system and ξ^m is the unknown local coordinate.

The normal vector $\boldsymbol{\eta}_1^s$ is defined on the slave surface and is given by the average of its two adjacent slave segments (i.e. in a two-dimension domain), as follows,

$$\boldsymbol{\eta}_j^s = \frac{\frac{l_2}{l_1}\boldsymbol{\eta}_1^{seg} + \frac{l_1}{l_2}\boldsymbol{\eta}_2^{seg}}{\left\|\frac{l_2}{l_1}\boldsymbol{\eta}_1^{seg} + \frac{l_1}{l_2}\boldsymbol{\eta}_2^{seg}\right\|}, \ \forall \ \Omega_0^s \subset \mathbb{R}^2. \tag{4.34}$$

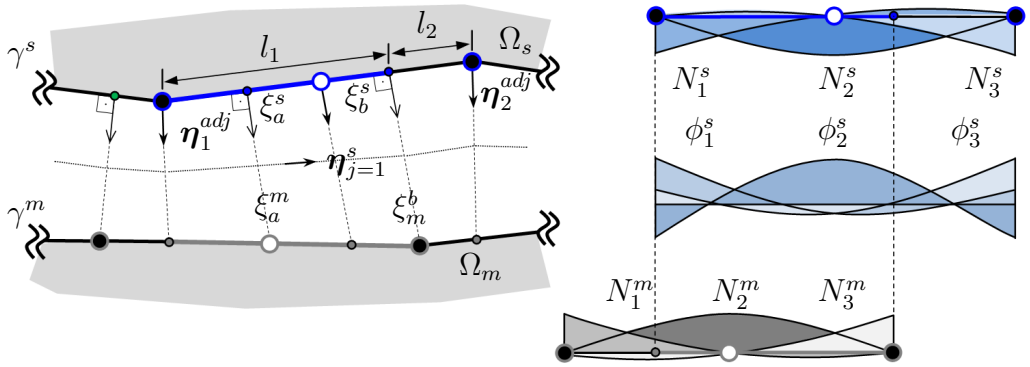

Figure 4.2: Continuous normal field Mortar segmentation method.

Here, $\boldsymbol{\eta}_{1,2}^{seg}$ are the unit vectors normal to the segments adjacent to the slave node with coordinates $\mathbf{x}_1^s$ and $l_{1,2}$ are the respective lengths of these segments.

On the other hand, the projection of the master node, x_2^m, onto a slave element, with nodal coordinates x_1^s and x_2^s, is given by,

$$[N_1^s(\xi^s)\mathbf{x}_1^s + N_2^s(\xi^s)\mathbf{x}_2^s - \mathbf{x}_2^m] \times [N_1^s(\xi^s)\boldsymbol{\eta}_1^s + N_2^s(\xi^s)\boldsymbol{\eta}_2^s] = \mathbf{0}, \tag{4.35}$$

where $N_{1,2}^s$ are the shape functions defined on slave side local coordinate system and, ξ^s, is the unknown projection coordinate defined on the slave side local coordinate system.

The vectors $\boldsymbol{\eta}_{1,2}^s$ are the normal vectors associated with the two slaves nodes adjacent to the mortar element in question. A segment parametrization $\zeta \in [-1, +1]$ is introduced for every segment, where the end points are defined by the local element coordinates of the slave side, ξ_a^s and ξ_b^s, and master side, ξ_a^m and ξ_b^m. Therefore, employing the segment coordinates, ζ, it is possible to define a mapping from element coordinates, $\xi^i,\ i = \{s, m\}$, to the segment coordinates, ζ,

$$\xi^i = \frac{1}{2}\left[1 - \zeta\right]\xi_a^i + \frac{1}{2}\left[1 + \zeta\right]\xi_b^i. \tag{4.36}$$

Finally, segment contributions are summed on both sides of the contact surface (element by element), for all contact segments, n_{seg}^m, respecting Eq. (4.29),

$$\begin{aligned}
\mathbf{D}_{[j,k]} &= \int_{\{\gamma_c^s\}^h} \boldsymbol{\phi}_j N_k^s d\gamma_c^s\ \mathbf{I}_2 = \int_{\{\gamma_c^s\}^h} N_j^s d\gamma_c^s\ \mathbf{I}_2 = D_{[j,j]}\ \mathbf{I}_2, \\
D_{[j,j]} &= \sum_{e=1}^{n_{ele}^s} \int_{-1}^{+1} N_j^s\left(\xi_e^s\right) \left\| \frac{\partial \mathbf{x}}{\partial \xi_e^s} \right\| d\xi_e^s = \sum_{e=1}^{n_{ele}^s} \frac{l_e}{2},
\end{aligned} \tag{4.37}$$

$$\mathbf{M}_{[j,l]} = \int_{\{\gamma_c^s\}^h} \boldsymbol{\phi}_j N_l^m \; d\gamma_c^s \; \mathbf{I}_2 = M_{[j,l]} \; \mathbf{I}_2,$$

$$M_{[j,l]} = \sum_{e=1}^{n_{ele}^s} \sum_{m=1}^{n_{seg}^m} \int_{-1}^{+1} \phi_j \left(\xi_e^s \left(\zeta_m\right)\right) N_j^m \left(\xi_e^s \left(\zeta_m\right)\right) \left\| \frac{\partial \mathbf{x}}{\partial \xi_e^s} \right\| \; \frac{\partial \xi_e^s}{\partial \zeta_m} \; d\zeta_m$$

$$= \sum_{e=1}^{n_{ele}^s} \sum_{m=1}^{n_{seg}^m} \sum_{gp=1}^{n_{gp}} \phi_j \left(\xi_e^s \left(\zeta_m^{gp}\right)\right) N_j^m \left(\xi_e^s \left(\zeta_m^{gp}\right)\right) \left\| \frac{\partial \mathbf{x}}{\partial \xi_e^s} \right\| \; \frac{\partial \xi_e^s}{\partial \zeta_m} \; w_{gp}. \tag{4.38}$$

where, $\mathbf{D} \in \mathbb{R}^{\{2n_s\}\times\{2n_s\}}$ and $\mathbf{M} \in \mathbb{R}^{\{2n_s\}\times\{2n_m\}}$ are known as mortar matrices and $\mathbf{I}_2$ is the second order identity tensor. Mortar matrices must be pulled back to the reference configuration using the mapping operator φ in order to respect the Total Lagrangian formulation detailed in Appendix A.

As mentioned in Section 2.3, the computation of the unit tangential vector can be recovered directly from its orthonormal relation with the normal vector, as follows,

$$\boldsymbol{\tau} = e_3 \times \boldsymbol{\eta}, \; \forall \; \Omega_0^s \subset \mathbb{R}^2. \tag{4.39}$$

4.3.6 Evaluation of the mortar integrals for 3D analysis

In the three-dimensional domain, the computation of surface unit normal vectors, are obtained following the same concept presented in Equation (4.34): by averaging the element adjacent normals, $\boldsymbol{\eta}_e^{adj}$,

$$\boldsymbol{\eta}_1^s = \frac{\sum_{e=1}^{n_e^{adj}} \left(\boldsymbol{\eta}_1^e\right)}{\left\| \sum_{e=1}^{n_e^{adj}} \left(\boldsymbol{\eta}_1^e\right) \right\|}, \; \forall \; \Omega_0^s \subset \mathbb{R}^3. \tag{4.40}$$

However, within this work, the relative dimension of the finite elements employed for the discretization of the 3D solids has made the inclusion of lenght and width of finite element e (i.e. weighting balance) irrelevant to the computation of Equation 4.40. Therefore, this aspect is disregarded. Again, the surface unit tangential vectors are obtained from the orthonormal relation with the normal direction, such that,

$$\boldsymbol{\eta}_j \times \boldsymbol{\tau}_j^{\xi} = \boldsymbol{\tau}_j^{\chi}, \; \boldsymbol{\eta}_j \cdot \boldsymbol{\tau}_j^{\xi} = 0, \; \boldsymbol{\eta}_j \cdot \boldsymbol{\tau}_j^{\chi} = 0, \; \forall \; \Omega_0^s \subset \mathbb{R}^3. \tag{4.41}$$

Since the overlapped region of contact between three-dimensional bodies generates polygon areas, the numerical integration of the mortar operators, matrices $\mathbf{D} \in \mathbb{R}^{\{3n_s\}\times\{3n_s\}}$ and $\mathbf{M} \in \mathbb{R}^{\{3n_s\}\times\{3n_m\}}$, requires a more complex approach. In order to obtain the mortar matrices within a three-dimensional domain, one can employ the so-called Mortar coupling algorithm, introduced by Puso & Laursen [63], and described as follows,

1. Start loop over non-mortar side elements $k = 1, ..., n_e^s$, where n_e^s is the number of elements on non-mortar side,

2. Create an auxiliary plane p from the unit normal vector $\boldsymbol{\eta}$ and the point, $\mathbf{x}_0$, at the geometric center of element k,

3. Obtain the projected slave nodes, $\tilde{\mathbf{x}}_k^s$, by mirroring the slave element nodes (from facet k onto plane p), $\mathbf{x}_k^s$, $k = 1, ..., n_{seg}^s$, along the unit normal vector, $\boldsymbol{\eta}$,

4. Obtain the projected master nodes, $\tilde{\mathbf{x}}_l^m$, by mirroring the master element nodes (from facet l onto plane p), $\mathbf{x}_l^m$, $l = 1, ..., n_e^m$, along the unit normal vector, $\boldsymbol{\eta}$,

5. Use a clipping algorithm [24] to create the polygon formed by $\tilde{k} \cap \tilde{l}$ (Figure 4.3).

6. Apply Delaunay triangulation: Locate geometric center of polygon, $\mathbf{x}_q = \sum_{q=1}^{3} N_q(\xi)\mathbf{x}_q^{cell}$, by dividing the polygon into n_{cell} triangular cells (Figure 4.3) and parametrize each triangle q using it's vertices, $\mathbf{x}_q^{cell}, q = 1, ..., 3$, and triangular shape functions N_q within the parent domain $\boldsymbol{\xi} = [\xi_1, \xi_2]^T$,

7. Employ Gauss-Radau [12] to locate the Gauss points, n_{gp}, and the integration weights, w_{gp}, for each triangular cell.

8. Obtain the matrices $D_{[j,k]}^{s,m}$ and $M_{[j,l]}^{s,m}$, for $k = 1, ..., n_s^e$ and $l = 1, ..., n_m^e$ by performing a gaussian integration on all triangular cells, such that,

$$D_{[j,k]}^{s,m} = \sum_{c=1}^{n_{cell}} \left[\sum_{g=1}^{n_{gp}} w_{gp} \phi_j^s(\boldsymbol{\xi}^s) N_k^s(\boldsymbol{\xi}^s) J_c \right],$$
$$M_{[j,l]}^{s,m} = \sum_{c=1}^{n_{cell}} \left[\sum_{g=1}^{n_{gp}} w_{gp} \phi_j^s(\boldsymbol{\xi}^s) N_l^m(\boldsymbol{\xi}^m) J_c \right],$$

where $J_c, c = 1, ..., n_{cell}$ is the Jacobian determinant of the integration cell.

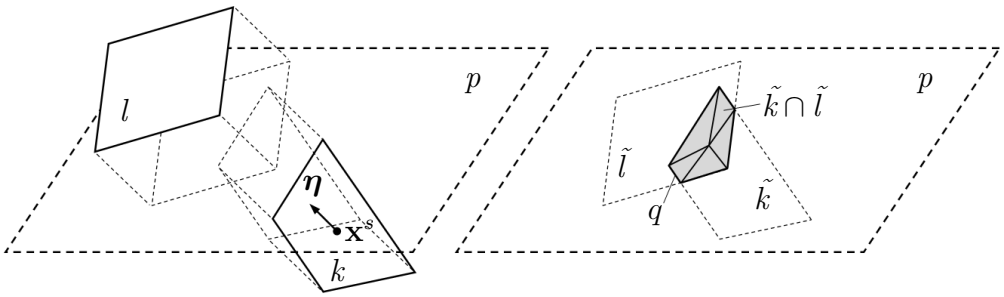

Figure 4.3: Clipping procedure employed to evaluate the Mortar integrals.

4.3.7 Discretization of the contact virtual work with wear

Replacing the displacement, $\mathbf{u}$, the incremental displacement, $\delta\mathbf{u}$, and the vector of lagrangian multipliers, $\boldsymbol{\lambda}$, in Equation (4.12) by their respective interpolations,

yields the discretized form of the contact virtual work with wear,

$$\begin{aligned}\delta\Pi_c + \delta\Pi_w \approx \delta\Pi_c^h + \delta\Pi_w^h &= \int_{\{\gamma_c^s\}^h} \left[1 - \mu \left\|\boldsymbol{\eta}\right\|\right] \boldsymbol{\lambda}^h \cdot \left[\left\{\delta\mathbf{u}^s\right\}^h - \left\{\delta\mathbf{u}^m\right\}^h\right] d\gamma_c^s \\ &= \sum_{j=1}^{n_s} \left\{ \sum_{k=1}^{n_s} \left[\delta\mathbf{d}_k^s\right]^T \int_{\{\gamma_c^s\}^h} \boldsymbol{\phi}_j N_k^s \; d\gamma_c^s \right. \\ &\quad \left. - \sum_{l=1}^{n_m} \left[\delta\mathbf{d}_l^m\right]^T \int_{\{\gamma_c^s\}^h} \boldsymbol{\phi}_j N_l^m \; d\gamma_c^s \right\} \left[1 - \mu \left\|\boldsymbol{\eta}\right\|\right] \mathbf{z}_j. \end{aligned} \tag{4.42}$$

Moreover, by introducing the Mortar matrices, $\mathbf{D} \in \mathbb{R}^{\{2n_s\}\times\{2n_s\}}$ and $\mathbf{M} \in \mathbb{R}^{\{2n_s\}\times\{2n_m\}}$,

$$\mathbf{D}_{[j,k]} = \int_{\{\gamma_c^s\}^h} \boldsymbol{\phi}_j N_k^s \; d\gamma_c^s \; \mathbf{I}_2, \tag{4.43}$$

$$\mathbf{M}_{[j,l]} = \int_{\{\gamma_c^s\}^h} \boldsymbol{\phi}_j N_l^m \; d\gamma_c^s \; \mathbf{I}_2, \tag{4.44}$$

it is possible to rewrite Equation (4.42), in it's algebraic form,

$$\delta\Pi_c^h + \delta\Pi_w^h = \left\{ \left[\delta\mathbf{d}^s\right]^T \mathbf{D} - \left[\delta\mathbf{d}^m\right]^T \mathbf{M}^T \right\} \left[\mathbf{z} - \mu\mathbf{z} \cdot \boldsymbol{\eta}\right], \tag{4.45}$$

where $\mathbf{I}_2$ is the identity matrix in $\mathbb{R}^{2\times2}$. The nodal test function values and the discrete nodal values are conveniently expressed in matrix notation by the global vectors $\delta\mathbf{d}^s$, $\delta\mathbf{d}^m$ and $\mathbf{z}$.

4.3.8 Discretization of the contact constraints and wear depth

The discretization of the contact constraints in the normal direction is performed by introducing the interpolation of displacements and lagrangian multipliers into Equation (4.10), which yields the following discretized form of the weak non-penetration condition [62],

$$\begin{aligned}\delta g \approx \delta g^h &= -\int_{\{\gamma_c^s\}^h} \left\{\delta\lambda_\eta\right\}^h \boldsymbol{\eta} \left[\left\{\mathbf{x}^s\right\}^h - \left\{\hat{\mathbf{x}}^m\right\}^h\right] d\gamma_c^s \\ &= -\sum_{j=1}^{n_s} \left\{ \sum_{k=1}^{n_s} \left\{\delta z_\eta\right\}_j \int_{\{\gamma_c^s\}^h} \boldsymbol{\phi}_j N_k^s \boldsymbol{\eta}_j^T \; d\gamma_c^s \; \mathbf{x}_k^s \right\} \\ &\quad + \sum_{j=1}^{n_s} \left\{ \sum_{l=1}^{n_m} \left\{\delta z_\eta\right\}_j \int_{\{\gamma_c^s\}^h} \boldsymbol{\phi}_j N_l^m \boldsymbol{\eta}_j^T \; d\gamma_c^s \; \mathbf{x}_l^m \right\} \geq 0. \end{aligned} \tag{4.46}$$

Hence, introducing a vector of discretized weighted gaps, $\tilde{\mathbf{g}} \in \mathbb{R}^{n_s}$, and a vector of nodal values of the normal contact stresses, $\delta\mathbf{z} \in \mathbb{R}^{n_s}$, yields the algebraic form of Equation (4.46),

$$\delta\tilde{g}^h = \left[\delta\mathbf{z}\right]^T \tilde{\mathbf{g}}, \tag{4.47}$$

which single entry, $\tilde{g}_j$, is given by,

$$\tilde{g}_j = -\left[\boldsymbol{\eta}_j\right]^T \left\{ \mathbf{D}_{[j,j]} \left[\mathbf{x}_j^s\right] - \sum_{l=1}^{n_m} \mathbf{M}_{[j,l]} \left[\mathbf{x}_l^m\right] \right\}. \tag{4.48}$$

The discretized form of total wear volume, $\delta\tilde{w}$, is obtained from the evaluation of the dissipated energy, such that,

$$\begin{aligned} \delta\tilde{w} \approx \delta w^h &= \alpha_w \int_{\{\gamma_c^s\}^h} \{\delta\mu\lambda_\eta\}^h \boldsymbol{\eta} \left[\{\mathbf{x}^s\}^h - \{\hat{\mathbf{x}}^m\}^h\right] d\gamma_c^s \\ &= \sum_{j=1}^{n_s} \left\{ \sum_{k=1}^{n_s} \{\delta z_\eta\}_j \int_{\{\gamma_c^s\}^h} \boldsymbol{\phi}_j N_k^s \boldsymbol{\eta}_j^T \; d\gamma_c^s \; \mathbf{x}_k^s \right\} \\ &\quad - \sum_{j=1}^{n_s} \left\{ \sum_{l=1}^{n_m} \{\delta z_\eta\}_j \int_{\{\gamma_c^s\}^h} \boldsymbol{\phi}_j N_l^m \boldsymbol{\eta}_j^T \; d\gamma_c^s \; \mathbf{x}_l^m \right\} \geq 0. \end{aligned} \tag{4.49}$$

Hence, employing the relations defined in Subsection 3.3.2 the single entry $\tilde{h}_j$, can be obtained,

$$\tilde{h}_j = \frac{\delta\tilde{w} \left\{z_\eta\right\}_j}{n^e A_e \sum_{e=1}^{n_e} \sum_{j=1}^{n_e^{adj}} \left(\left\{z_\eta\right\}_j\right)}. \tag{4.50}$$

where the z_η is the normal part of the discrete nodal values of the lagrangian multipliers, $\mathbf{z}_j$, such that,

$$\begin{aligned} \mathbf{z}_j &= \left\{z_\eta\right\}_j \boldsymbol{\eta}_j + \left\{z_\tau^\xi\right\}_j \boldsymbol{\tau}_j^\xi + \left\{z_\tau^\chi\right\}_j \boldsymbol{\tau}_j^\chi \; ; \\ \left\{z_\eta\right\}_j &= \mathbf{z}_j \cdot \boldsymbol{\eta}_j, \; \left\{z_\tau^\xi\right\}_j = \mathbf{z}_j^\xi \cdot \boldsymbol{\tau}_j^\xi, \; \left\{z_\tau^\chi\right\}_j = \mathbf{z}_j^\chi \cdot \boldsymbol{\tau}_j^\chi. \end{aligned} \tag{4.51}$$

The discretization of the tangential contact constraints adopted here has been proposed in Gitterle et al. [33] and is only briefly addressed. For the tangential direction, an additional interpolation β^h of β, Equation (2.12), is required

$$\beta \approx \beta^h = \sum_{b=1}^{n_s} \rho_b \left(\boldsymbol{\xi}^s \left(X^s\right)\right) \beta_b, \tag{4.52}$$

where β_b are discrete nodal values and ρ_b are the shape functions, which fulfill an additional condition in order to decouple the lagrangian multipliers [33]. Replacing

the terms of Equation (4.11) by their interpolated forms, yields,

$$\begin{aligned}
&\int_{\gamma_c^s} \delta\lambda_\tau \left[\vartheta_\tau(\mathbf{X},t) - \beta\lambda_\tau\right]\ d\gamma_c^s, \\
\approx &\int_{\{\gamma_c^s\}^h} \delta\lambda_\tau^h \left[\vartheta_\tau^h(\mathbf{X},t) - \beta^h\lambda_\tau^h\right]\ d\gamma_c^s, \\
= &\sum_{j=1}^{n_s}\sum_{k=1}^{n_s} \{\delta z_\tau\}_j \left[\boldsymbol{\tau}_j\right]^T \int_{\{\gamma_c^s\}^h} \boldsymbol{\phi}_j N_k^s d\gamma_c^s \dot{\mathbf{x}}_k^s \\
- &\sum_{j=1}^{n_s}\sum_{l=1}^{n_m} \{\delta z_\tau\}_j \left[\boldsymbol{\tau}_j\right]^T \int_{\{\gamma_c^s\}^h} \boldsymbol{\phi}_j N_l^m d\gamma_c^s \dot{\mathbf{x}}_l^m \\
- &\sum_{j=1}^{n_s}\sum_{b=1}^{n_s}\sum_{p=1}^{n_s} \{\delta z_\tau\}_j \left[\boldsymbol{\tau}_j\right]^T \int_{\{\gamma_c^s\}^h} \boldsymbol{\phi}_j \rho_b \boldsymbol{\phi}_p \beta_b \mathbf{z}_p\ d\gamma_c^s = 0,
\end{aligned} \tag{4.53}$$

which in nodal form is denoted by,

$$\begin{aligned}
&-\left[\boldsymbol{\tau}_j\right]^T \mathbf{D}_{[j,j]} \left[\dot{\mathbf{x}}_j^s\right] + \left[\boldsymbol{\tau}_j\right]^T \sum_{l=1}^{n_m} \mathbf{M}_{[j,l]} \left[\dot{\mathbf{x}}_l^m\right] \\
&-\left[\boldsymbol{\tau}_j\right]^T \sum_{b=1}^{n_s}\sum_{p=1}^{n_s} \int_{\{\gamma_c^s\}^h} \boldsymbol{\phi}_j \rho_b \boldsymbol{\phi}_p \beta_b \mathbf{z}_p\ d\gamma_c^s = 0.
\end{aligned} \tag{4.54}$$

Furthermore, by employing an appropriate measure for the tangential velocity, $\tilde{\vartheta}_\tau$, and a backward Euler scheme, it is possible to obtain the discretized form of the weak tangential condition, at a time t_n, for each slave node j,

$$\begin{aligned}
&-\{\left[\boldsymbol{\tau}_j\right]^T \dot{\mathbf{D}}_{[j,j]} \left[\mathbf{X}_j^s + \mathbf{d}_j^s\right] - \left[\boldsymbol{\tau}_j\right]^T \sum_{l=1}^{n_m} \dot{\mathbf{M}}_{[j,l]} \left[\mathbf{X}_l^m + \mathbf{d}_l^m\right]\} \cdot \Delta t_n \\
&-\{\left[\boldsymbol{\tau}_j\right]^T \int_{\{\gamma_c^s\}^h} \boldsymbol{\phi}_j \beta_j\ d\gamma_c^s\} \mathbf{z}_j \Delta t_n = 0,
\end{aligned} \tag{4.55}$$

which can be written in the following condensed form:

$$\{\tilde{u}_\tau\}_j - \left\{\tilde{\beta}_\tau\right\}_j \{z_\tau\}_j = 0. \tag{4.56}$$

4.4 Discretized problem

In order to make the notation clearer, the finite element nodes of the problem are grouped into three subsets: the set $\mathcal{M}$ of potential contact nodes on the mortar side, the set $\mathcal{S}$ of potential contact nodes on the slave side and the set $\mathcal{N}$ of all remaining nodes. Therefore, the vector of global nodal displacements can be represented by:

$$\mathbf{d} = \left[\mathbf{d}_{\mathcal{N}},\ \mathbf{d}_{\mathcal{M}},\ \mathbf{d}_{\mathcal{S}}\right]^T. \tag{4.57}$$

An equivalent notation is employed for the geometry and virtual displacements. Consequently, the discretized contact virtual work, Equation (4.12), can be expressed in matrix form,

$$\delta\Pi_c^h = [\delta\mathbf{d}]^T \left[\mathbf{D} - \mathbf{M}^T\right] \mathbf{z}, \tag{4.58}$$

from where the contact forces can be retrieved,

$$\mathbf{f}_c(\mathbf{d}, \mathbf{z}) = \left[\mathbf{0},\ -\mathbf{M}^T,\ \mathbf{D}\right] \mathbf{z}. \tag{4.59}$$

The weak form of equilibrium, Equation (4.20), can then be expressed by the following non-linear algebraic system:

$$\mathbf{f}_{\text{int}}(\mathbf{d}) - \mathbf{f}_{\text{ext}} + \mathbf{f}_c(\mathbf{d}, \mathbf{z}) = 0, \tag{4.60}$$

where $\mathbf{f}_{\text{int}}$ and $\mathbf{f}_{\text{ext}}$ are, respectively, internal and external global force vectors resulting from assemblage of the element vectors for each body:

$$\mathbf{f}_{\text{int}}^{i(e)} = \int_{\varphi\left(\Omega_0^{i(e)}\right)} [\mathsf{B}]^T\, \mathsf{S}_{n+1}\ d\Omega^i, \tag{4.61}$$

$$\mathbf{f}_{\text{ext}}^{i(e)} = \int_{\varphi\left(\Omega_0^{i(e)}\right)} [\mathsf{N}]^T\, \mathbf{b}_{n+1}\ d\Omega^i + \int_{\varphi\left(\Omega_0^{i(e)}\right)} [\mathsf{N}]^T\, \hat{\mathbf{t}}_{n+1}\ d\gamma_N^i, \tag{4.62}$$

with B and N being the standard discrete symmetric gradient operators and the interpolation matrix of the element (e), respectively. The vector S_{n+1} contains the Cauchy stress components delivered by the algorithmic constitutive function.

It is important to remark that Equation (4.60) is highly non-linear. From one side, the internal force vector is a non-linear function of the displacements due to the finite inelastic deformations involved. On the ther hand, the contact force vector also depends nonlinearly on the displacements since the mortar matrices are computed over the deformed configuration.

The overall discretized problem is composed by the discretized equilibrium equations, Equation (4.60), the discretized Karush-Kuhn-Tucker conditions:

$$[\tilde{g}_j + \tilde{h}_j] \geq 0,\ \{z_\eta\}_j \geq 0,\ \{z_\eta\}_j [\tilde{g}_j + \tilde{h}_j] = 0. \tag{4.63}$$

and the discretized relation for the tangential contact stresses:

$$\begin{aligned} \{\tilde{u}_\tau\}_j - \left\{\tilde{\beta}_\tau\right\}_j \{z_\tau\}_j = 0, \bar{\tilde{\mathfrak{F}}}_j \leq 0, \\ \left\{\tilde{\beta}_\tau\right\}_j \geq 0, \\ \bar{\tilde{\mathfrak{F}}}_j \left\{\tilde{\beta}_\tau\right\}_j = 0. \end{aligned} \tag{4.64}$$

The contact constraints Equation (4.63) and Equation (4.64) are expressed by a set of inequality conditions which need to be solved with an appropriate solution strategy.

Chapter 5

Solution procedure

The solution procedure employed for solving the discrete frictional contact problem in a fretting wear condition, presented in Chapter 4, is described here. In Section 5.1, the algebraic form of the minimization problem is introduced while Section 5.2 address the different approaches undertaken to solve it. A brief overview on the matrix representation of the residual problem is presented in Section 5.3.

5.1 Algebraic form

The frictional contact problem, which is described by the discretized system of equations (4.60) and constraints (4.63) and (4.64), is essentially a minimization problem with inequality constraints. This problem can be solved with a primal-dual active set strategy proposed by Hintermüller et al. [39] and first applied to contact problems by Hüeber et al. [43]. It consists in finding the set of *active* contacting nodes, $\mathcal{A}$, and the set of inactive nodes, $\mathcal{I}$, of the slave set $\mathcal{S} = \{\mathcal{A} \cup \mathcal{I}\}$ while minimizing the contact constraints. The search for the sets $\mathcal{A}$ and $\mathcal{I}$ is performed by solving the non-penetration function for every slave node, j,

$$\tilde{g}_j = 0, \ \forall \ \{j \in \mathcal{A}\} . \tag{5.1}$$

This search can be extended to include the subset of active contact nodes sticking, $\mathcal{Q}$, and the subset of active contact nodes sliding, $\mathcal{L}$. This can be achieved by solving the frictional condition, Equation $(4.64)_1$, for every slave node, j.

The determination of the sets $\mathcal{I}$ and $\mathcal{A}$, together with the subsets $\mathcal{Q}$ and $\mathcal{L}$,

allows the problem to be stated with equality conditions:

$$\begin{aligned}
\mathbf{r} &= \mathbf{f}_{\text{int}}(\mathbf{d}) - \mathbf{f}_{\text{ext}} + \mathbf{f}_c(\mathbf{d}, \mathbf{z}), \\
\tilde{g}_j &= 0, \ \forall \ \{j \in \mathcal{A}\}, \\
\tilde{h}_j &= 0, \ \forall \ \{j \in \mathcal{A}\}, \\
\{z_\eta\}_j &= 0, \ \forall \ \{j \in \mathcal{I}\}, \\
\left\{\tilde{\beta}_\tau\right\}_j &= 0, \ \forall \ \{j \in \mathcal{Q}\} \\
\bar{\mathfrak{F}}(x, y, z) &= 0, \ \forall \ \{j \in \mathcal{S}\} \\
\{\tilde{u}_\tau\}_j - \left\{\tilde{\beta}_\tau\right\}_j \{z_\tau\}_j &= 0, \ \forall \ \{j \in \mathcal{L}\}.
\end{aligned} \tag{5.2}$$

To solve the frictional problem with a semi-smooth Newton method, two complementarity functions for the frictional constraints must be introduced. The complementarity functions are non-continuous relations used to verify the frictional state of the contacting nodes. They implicit incorporate the distinction between inactive nodes, active sticking nodes and active sliding nodes. This concept was first introduced to a Dual Mortar formulation by Hüeber et al. [41], for the Tresca frictional case. Later, complementarity functions for Coulomb's friction were proposed by Gitterle et al. [33]. The complementarity function for the normal contact conditions, which is described in detail in [62], is defined for each slave node $j \in \mathcal{S}$ as:

$$\{C_\eta\}_j(\mathbf{d}, \mathbf{z}) = \{z_\eta\}_j - \max\left(0, \{z_\eta\}_j - c_n \tilde{g}_j\right), \tag{5.3}$$

For the tangential contact conditions, the complementarity functions given in [33] are defined for each slave node $j \in \mathcal{S}$ as:

$$\begin{aligned}
\{\mathbf{C}_\tau\}_j(\mathbf{d}, \mathbf{z}) = \{z_\tau\}_j \max\Big(&\mu\left[\{z_\eta\}_j - c_\eta \tilde{g}_j\right], \left|\{z_\tau\}_j + c_\tau \{\tilde{\mathbf{u}}_\tau\}_j\right|\Big) \\
&-\mu\left[\{z_\tau\}_j + c_\tau \tilde{\mathbf{u}}_j\right] \max\left(0, \left[\{z_\eta\}_j - c_\tau \tilde{g}_j\right]\right).
\end{aligned} \tag{5.4}$$

The parameters c_η and c_τ are positive constants that do not affect the solution results but can influence the convergence behavior. In the numerical examples, the impact of these parameters in the solution of the class of problems addressed in this work will be studied in detail.

The combination of the equilibrium equation (4.60) with the complementarity functions for the contact conditions in the normal, expression (5.3), and tangential, expression (5.4), directions leads to the following nonlinear system of equations:

$$\begin{aligned}
\mathbf{r} = \mathbf{f}_{\text{int}}(\mathbf{d}) - \mathbf{f}_{\text{ext}} + \mathbf{f}_c(\mathbf{d}, \mathbf{z}) &= \mathbf{0}, \\
\{C_\eta\}_j(\mathbf{d}, \mathbf{z}) &= 0, \ \forall \ \{j \in \mathcal{S}\}, \\
\{\mathbf{C}_\tau\}_j(\mathbf{d}, \mathbf{z}) &= 0, \ \forall \ \{j \in \mathcal{S}\}.
\end{aligned} \tag{5.5}$$

Due to the max-operator and the Euclidian norm employed in the two complementarity functions, they are continuous but non-smooth and not uniquely differentiable. Therefore, this justifies the application of the semi-smooth Newton-Method [11, 39]. The generalized derivative for the max-function [62], is defined

as:

$$f(x) = max(a, x) \rightarrow \Delta f(x) = \begin{cases} 0, & \text{if } x \leq a, \\ 1, & \text{if } x > a. \end{cases} \tag{5.6}$$

Therefore, the solution of the system of equations (5.5) treats material and geometrical nonlinearities as well as nonlinearities emerging from contact and friction.

5.2 Primal-dual active set algorithms

The solution of the frictional contact problem, with the so-called primal-dual active set strategy (PDASS), can be obtained by solving either the system of equations (5.2) or (5.5). In the first case, due to the possibility of linearizing the system of equations (5.5), an algorithm with a single iteration loop for the solution of all sources of nonlinearity is obtained, see Table 5.1. This strategy has been employed by several authors and proven to be very efficient [33, 41, 62]. In the second case, two nested iterative schemes are necessary. An inner iteration for the nonlinear finite element problem having the active set fixed followed by an outer loop for solving the active set and update the geometries for removing the worn material, see Table 5.2. This strategy has been employed for the solution of dynamic problems [37] and nonlinear material behavior with multigrid methods in [10], among others. Here, both PDASS will be applied to the simulation of frictional contact problems undergoing finite strains and inelastic material behavior. In the following, these two schemes are detailed and their algorithms presented.

5.2.1 Fully implicit scheme

The fully implicit scheme consists in the solution of both contact constraints and fretting wear variables in a single iterative step within a fully linearized tangent matrix. Therefore, in this strategy the energy lost due to wear and the subsequent wear depth are updated together with the gap and the primal-dual pair (i.e. in the same iteration $\Bbbk$). It is important to remark that this strategy can only be applied to problems where the wear coefficient α_w is relatively small or if small load increments are employed. This restriction is required due to the high sensitivity of the PDASS to active set changes, which might happen frequently if large amounts of material are removed in each load step. Employing the PDASS together with a linear form of the system of equations (5.2), allows the derivation of a single iteration loop algorithm for the solution of all sources of nonlinearity the contact problem. Table 5.1 summarizes this solution procedure.

5.2.2 Nested scheme

The *nested* scheme, as the name implies, is obtained by splitting the convergence check into two different iterative steps. The first pseudo-time step, $\mathbb{I}$, is used for finding the primal-dual pair, $\Delta\mathbf{d}^{\mathbb{I}+1}, \mathbf{z}^{\mathbb{I}+1}$. The pseudo-time step, $\mathbb{I}$, is nested into an outter step, $\Bbbk$, which is used for solving the active set alongside with the topography update (i.e. wear depth, h) of the geometry. This procedure is as detailed in

Table 5.1: Single iterative strategy within a load step.

1. Set $\Bbbk = 0$ and initial conditions $\mathbf{d}^0, \mathbf{z}^0$. *Initialize* $\mathcal{A}^0$ and $\mathcal{I}^0$, such that $\mathcal{S} = \mathcal{A}^0 \cup \mathcal{I}^0$, $\mathcal{A}^0 \cap \mathcal{I}^0 = \emptyset$ and $\mathcal{A} = \mathcal{Q}^0 \cup \mathcal{L}^0$.
2. Loop over $\Bbbk$.
3. Solve the linearization of (5.2) for $(\Delta\mathbf{d}^{\Bbbk+1}, \mathbf{z}^{\Bbbk+1})$:

   $$\begin{aligned}
   &\Delta\mathbf{r}\left(\mathbf{d}^{\Bbbk}, \mathbf{z}^{\Bbbk}\right) = -\mathbf{r}^{\Bbbk},\\
   &\mathbf{z}_j^{\Bbbk+1} = 0,\ \forall\ \left\{j \in \mathcal{I}^{\Bbbk}\right\},\\
   &\Delta\tilde{g}_j^{\Bbbk} = -\tilde{g}_j^{\Bbbk},\ \forall\ \left\{j \in \mathcal{A}^{\Bbbk}\right\},\\
   &\Delta\tilde{h}_j^{\Bbbk} = -\tilde{h}_j^{\Bbbk},\ \forall\ \left\{j \in \mathcal{A}^{\Bbbk}\right\},\\
   &\Delta\left\{C_\tau\right\}_j^{\Bbbk} = -\left\{C_\tau\right\}_j^{\Bbbk},\ \forall\ \left\{j \in \mathcal{L}^{\Bbbk}\right\} \vee \left\{j \in \mathcal{Q}^{\Bbbk}\right\},
   \end{aligned}$$

4. Update nodal displacements: $\mathbf{d}^{\Bbbk+1} = \mathbf{d}^{\Bbbk} + \Delta\mathbf{d}^{\Bbbk+1}$.
5. Set $\mathcal{A}^{\Bbbk+1}$, $\mathcal{I}^{\Bbbk+1}$, $\mathcal{Q}^{\Bbbk+1}$ and $\mathcal{L}^{\Bbbk+1}$ to

   $$\begin{aligned}
   \mathcal{A}^{\Bbbk+1} &:= \left\{j \in \mathcal{S} \mid \left\{z_\eta\right\}_j^{\Bbbk+1} > c_\eta \tilde{g}_j^{\Bbbk+1}\right\},\\
   \mathcal{I}^{\Bbbk+1} &:= \mathcal{S}/\mathcal{A}^{\Bbbk+1},\\
   \mathcal{Q}^{\Bbbk+1} &:= \left\{j \in \mathcal{A}^{\Bbbk+1} \mid \mu\left[\left\{z_\eta\right\}_j^{\Bbbk+1} - c_\eta\tilde{g}_j^{\Bbbk+1}\right] > \left|\left\{z_\tau\right\}_j^{\Bbbk+1} + c_\tau\left\{\tilde{u}_\tau\right\}_j^{\Bbbk+1}\right|\right\},\\
   \mathcal{L}^{\Bbbk+1} &:= \left\{j \in \mathcal{A}^{\Bbbk+1} \mid \mu\left[\left\{z_\eta\right\}_j^{\Bbbk+1} - c_\eta\tilde{g}_j^{\Bbbk+1}\right] \leq \left|\left\{z_\tau\right\}_j^{\Bbbk+1} + c_\tau\left\{\tilde{u}_\tau\right\}_j^{\Bbbk+1}\right|\right\}.
   \end{aligned}$$

6. Convergence check

   IF $\mathcal{I}^{\Bbbk+1} = \mathcal{I}^{\Bbbk}$, $\mathcal{Q}^{\Bbbk+1} = \mathcal{Q}^{\Bbbk}$, $\mathcal{L}^{\Bbbk+1} = \mathcal{L}^{\Bbbk}$ and $\left\|\mathbf{r}_{\text{tot}}^{\Bbbk}\right\| \leq \mathcal{E}_r$, *THEN GOTO* Next increment *ELSE* set $\Bbbk := \Bbbk + 1$ and *GOTO* 2.

Table 5.2: Nested iterative strategy within a load step.

1. Set $\mathbb{I} = 0$ and $\Bbbk = 0$. Initialize $\mathbf{d}^0, \mathbf{z}^0$, $\mathcal{A}^0$ and $\mathcal{I}^0$, such that $\mathcal{S} = \mathcal{A}^0 \cup \mathcal{I}^0$, $\mathcal{A}^0 \cap \mathcal{I}^0 = \emptyset$ and $\mathcal{A}^0 = \mathcal{Q}^0 \cup \mathcal{L}^0$.
2. Loop over the active set $\Bbbk$,
3. Loop over $\mathbb{I}$,
4. Solve the linearization of (5.2) for $(\Delta\mathbf{d}^{\mathbb{I}+1}, \mathbf{z}^{\mathbb{I}+1})$:

   $\Delta\mathbf{r}\left(\mathbf{d}^{\mathbb{I}}, \mathbf{z}^{\mathbb{I}}\right) = \mathbf{r}^{\mathbb{I}}$,
   $\Delta\tilde{g}_j^{\mathbb{I}} = -\tilde{g}_j^{\mathbb{I}},\ \forall\ \left\{j \in \mathcal{A}^{\Bbbk}\right\}$,
   $\{z_n\}_j^{\mathbb{I}+1} = 0,\ \forall\ \left\{j \in \mathcal{I}^{\Bbbk}\right\}$,
   $\left\{\tilde{\beta}_\tau\right\}_j^{\mathbb{I}} = 0,\ \forall\ \left\{j \in \mathcal{Q}^{\Bbbk}\right\}$,
   $\{\tilde{u}_\tau\}_j^{\mathbb{I}} - \left\{\tilde{\beta}_\tau\right\}_j^{\mathbb{I}} \{z_\tau\}_j^{\mathbb{I}+1} = 0,\ \forall\ \left\{j \in \mathcal{L}^{\Bbbk}\right\}$.

5. Update $\mathbf{d}^{\mathbb{I}+1} = \mathbf{d}^{\mathbb{I}} + \Delta\mathbf{d}^{\mathbb{I}+1}$
6. Update the sets $\mathcal{A}^{\Bbbk+1}$, $\mathcal{I}^{\Bbbk+1}$, $\mathcal{Q}^{\Bbbk+1}$ and $\mathcal{L}^{\Bbbk+1}$ with

   $\mathcal{A}^{\Bbbk+1} := \left\{j \in \mathcal{S} \mid \{z_n\}_j^{\mathbb{I}+1} \geq \left[\Delta\tilde{g}_j^{\mathbb{I}+1} - \mathbf{d}^{\mathbb{I}+1} \cdot \mathbf{n}\right]\right\}$
   $\mathcal{I}^{\Bbbk+1} := \mathcal{S} / \mathcal{A}^{\Bbbk+1}$,
   $\mathcal{Q}^{\Bbbk+1} := \left\{j \in \mathcal{A}^{\Bbbk+1} \mid \mu\left[\{z_\eta\}_j^{\mathbb{I}+1}\right] \leq \{z_\tau\}_j^{\Bbbk+1}\right\}$,
   $\mathcal{L}^{\Bbbk+1} := \mathcal{A}^{\Bbbk+1} / \mathcal{Q}^{\Bbbk+1}$.

7. Active set check

   IF $\mathcal{I}^{\Bbbk+1} = \mathcal{I}^{\Bbbk}$, $\mathcal{Q}^{\Bbbk+1} = \mathcal{Q}^{\Bbbk}$ and $\mathcal{L}^{\Bbbk+1} = \mathcal{L}^{\Bbbk}$ *THEN GOTO* 8
   ELSE Set $\mathbb{I} = 0$, $\Bbbk = \Bbbk + 1$ and *GOTO* 2.

8. Wear depth evaluation:

   $\tilde{h}^{\Bbbk+1} = \tilde{h}^{\Bbbk} + \Delta\tilde{h}^{\Bbbk+1}$

9. Convergence check

   IF $\|\mathbf{r}_{\text{tot}}\| \leq \mathcal{E}_r$, *THEN GOTO* Next increment
   ELSE set $\mathbb{I} := \mathbb{I} + 1$ and *GOTO* 3.

Table 5.2. Although in this scheme, the number of steps required to solve a single load increment is higher and often the computation of the wear depth must be undertaken more than once per increment, the different sources of nonlinearity are detached. Therefore, the number of iterations in each pseudo-time step is reduced. Overall, for problems with a significantly large contact surface (particularly in 3D problems) and small load increments, this scheme can actually be very efficient.

5.3 Matrix representation

In order to solve the nonlinear system of equations (5.5) with a semi-smooth Newton algorithm, it is necessary to perform the full linearization of $\mathbf{r}$, C_η and $\mathbf{C}_\tau$ and then convert the linear system into an algebraic form. In the following, a matrix representation of these directional derivatives is provided and a detailed linearization of each term can be found in [33,41,62]. The linearization of $\mathbf{r}$ includes the derivation of the internal force vector $\mathbf{f}_{\text{int}}(\mathbf{d})$ and the contact force vector $\mathbf{f}_c(\mathbf{d},\mathbf{z})$ since we assume that the external loads are independent of the displacement $\mathbf{d}$. Therefore, the derivation of the internal force vector $\mathbf{f}_{\text{int}}(\mathbf{d})$ leads to the corresponding tangent stiffness matrix $\mathbf{K} \in \mathbb{R}^{(2nx2n)}$ which, in the case of the F-BAR formulation employed in this work, is obtained by the assemblage of the element stiffness matrices [15]:

$$\mathbf{K}^e = \int_{\varphi(\Omega_0^e)} \mathsf{G}^T[\mathsf{a}][\mathsf{G}]d\Omega + \int_{\varphi(\Omega_0^e)} \mathsf{G}^T[\mathsf{q}][\mathsf{G}_0 - \mathsf{G}]d\Omega, \tag{5.7}$$

where G is the standard discrete spatial gradient operator, G_0, is the gradient operator at the element centroid, a denotes the matrix form of the fourth order spatial elasticity tensor evaluated at $\mathsf{F} = \bar{\mathbf{F}}$,

$$[\mathsf{a}]_{ijkl} = \frac{1}{\det(\mathsf{F})} F_{jp} F_{tq} A_{ipkq}, \tag{5.8}$$

and q is the matrix form of the fourth order tensor defined by:

$$\mathsf{q} = \frac{1}{3}\mathsf{a} : [\mathbf{I} \otimes \mathbf{I}] - \frac{2}{3}[\sigma \otimes \mathbf{I}], \tag{5.9}$$

also computed at $\mathsf{F} = \bar{\mathsf{F}}$. In expression (5.8), A_{ipkq} denotes the components of the first elasticity tensor.

The linearization of the contact forces $\mathbf{f}_c(\mathbf{d},\mathbf{z})$, defined in Equation(4.59), can be expressed for a generic iteration $\Bbbk$ by:

$$\Delta\mathbf{f}_c^{\Bbbk}(\mathbf{d},\mathbf{z}) = [\mathbf{0}, -\Delta\mathbf{M}^T, \Delta\mathbf{D}]\mathbf{z}^{\Bbbk} := \tilde{\mathbf{C}}[\Delta\mathbf{d}_{\mathcal{S}}^{\Bbbk} + \Delta\mathbf{d}_{\mathcal{M}}^{\Bbbk}], \tag{5.10}$$

with the matrix $\tilde{\mathbf{C}} \in \mathbb{R}^{(n_{dim}n_s + n_{dim}n_m)\times(n_{dim}n_s + n_{dim}n_m)}$ containing the directional derivatives of the mortar matrices $\mathbf{D}$ and $\mathbf{M}$ [62, 88] together with the vector of nodal lagrangian multipliers, $\mathbf{z}$. The vectors $\Delta\mathbf{d}_{\mathcal{S}} \in \mathbb{R}^{n_{dim}n_s}$ and $\Delta\mathbf{d}_{\mathcal{M}} \in \mathbb{R}^{n_{dim}n_m}$ are subsets of the global displacement incremental vector, $\Delta\mathbf{d}$, given by,

$$\Delta\mathbf{d} = \left[\Delta\mathbf{d}_{\mathcal{N}},\ \Delta\mathbf{d}_{\mathcal{M}},\ \Delta\mathbf{d}_{\mathcal{I}},\ \Delta\mathbf{d}_{\mathcal{Q}},\ \Delta\mathbf{d}_{\mathcal{L}}\right]^T, \tag{5.11}$$

where the set of potential slave nodes, $\mathcal{S}$, has been decomposed into an inactive set, $\mathcal{I}$, a set of sticking activenodes, $\mathcal{Q}$ and a set of sliding active nodes, $\mathcal{L}$. The slave (non-mortar) side and master (mortar) side mortar matrices are also modified,

$$\mathbf{D} = \begin{bmatrix} \mathbf{D}_{\mathcal{I}} & \mathbf{0} & \mathbf{0} \\ \mathbf{0} & \mathbf{D}_{\mathcal{L}} & \mathbf{0} \\ \mathbf{0} & \mathbf{0} & \mathbf{D}_{\mathcal{Q}} \end{bmatrix}, \tag{5.12}$$

$$\mathbf{M} = \left[\mathbf{M}_{\mathcal{I}}\,,\ \mathbf{M}_{\mathcal{Q}}\,,\ \mathbf{M}_{\mathcal{L}}\right]. \tag{5.13}$$

The linearization of C_η consists on the directional derivative of the weighted normal gap $\tilde{g}$, which can be defined, for the normal constraints of the active nodes, $j \in \mathcal{A}$, as in [62]:

$$\mathop{\mathsf{A}}_{j=1}^{n_a} \left(\{\Delta\tilde{g}\}_j^{\Bbbk}\right) := \tilde{\mathbf{D}}_{\mathcal{A}^{\Bbbk}} \Delta\mathbf{d}_{\mathcal{S}}^{\Bbbk} + \tilde{\mathbf{M}}_{\mathcal{A}^{\Bbbk}} \Delta\mathbf{d}_{\mathcal{M}}^{\Bbbk},\ \{j \in \mathcal{A}\}\,, \tag{5.14}$$

with $\tilde{\mathbf{D}} \in \mathbb{R}^{(n_a \times n_{dim} n_m)}$ and $\tilde{\mathbf{M}} \in \mathbb{R}^{(n_a \times n_{dim} n_m)}$. The quantity n_a is the number of active slave nodes and the symbol A denotes the finite element assembly operator.

When employing the single step strategy, the evaluation of the nodal wear depth h_j is performed within each iteration. Therefore, an appropriate weighted wear depth vector, $\tilde{h}$, must be associated to the weighted normal gap, $\tilde{g}$. This vector is obtained from the assemblage of each contribution of w_e (described in Section 3.3.2) and is defined as follows,

$$\mathop{\mathsf{A}}_{j=1}^{n_a} \left(\left\{\Delta\tilde{h}\right\}_j^{\Bbbk}\right) := \alpha_w \tfrac{1}{n_{nod}^{adj}} \mu \left\|\mathbf{z}_j \cdot \boldsymbol{\eta}\right\| \left[\tilde{\mathbf{D}}_{\mathcal{A}^{\Bbbk}} \Delta\mathbf{d}_{\mathcal{S}}^{\Bbbk} + \tilde{\mathbf{M}}_{\mathcal{A}^{\Bbbk}} \Delta\mathbf{d}_{\mathcal{M}}^{\Bbbk}\right],\ \{j \in \mathcal{A}\}\,, \tag{5.15}$$

The directional derivatives obtained from the linearization of Equation (5.4), are defined in terms of two sets of matrices. The first set is concerned with the stick condition:

$$\mathbf{F}_{\mathcal{Q}} \in \mathbb{R}^{(n_q \times n_{dim} n_s)},\ \mathbf{H}_{\mathcal{Q}} \in \mathbb{R}^{(n_q \times n_{dim} n_m)} \text{ and } \mathbf{Q}_{\mathcal{Q}} \in \mathbb{R}^{(n_q \times n_{dim} n_q)},$$

and the second set is concerned with the slip condition:

$$\mathbf{G}_{\mathcal{L}} \in \mathbb{R}^{(n_l \times n_{dim} n_s)}, \mathbf{J}_{\mathcal{L}} \in \mathbb{R}^{(n_l \times n_{dim} n_m)} \text{ and } \mathbf{L}_{\mathcal{L}} \in \mathbb{R}^{(n_l \times n_{dim} n_l)}.$$

Then, two systems – that must be solve within the Equation (4.60) for every iteration $\Bbbk$ – are created,

$$\mathop{\mathsf{A}}_{q=1}^{n_q} \left(\Delta\left\{C_\tau\right\}_q^{\Bbbk}\right) := \mathbf{F}_{\mathcal{Q}} \Delta\mathbf{d}_{\mathcal{S}}^{\Bbbk} + \mathbf{H}_{\mathcal{Q}} \Delta\mathbf{d}_{\mathcal{M}}^{\Bbbk} + \mathbf{Q}_{\mathcal{Q}} \mathbf{z}_{\mathcal{Q}}^{\Bbbk+1},\ \{q \in \mathcal{Q}\}\,, \tag{5.16}$$

$$\mathop{\mathsf{A}}_{l=1}^{n_l} \left(\Delta\left\{C_\tau\right\}_l^{\Bbbk}\right) := \mathbf{G}_{\mathcal{L}} \Delta\mathbf{d}_{\mathcal{S}}^{\Bbbk} + \mathbf{J}_{\mathcal{L}} \Delta\mathbf{d}_{\mathcal{M}}^{\Bbbk} + \mathbf{L}_{\mathcal{L}} \mathbf{z}_{\mathcal{L}}^{\Bbbk+1},\ \{l \in \mathcal{L}\}\,. \tag{5.17}$$

The assemblage of the vector of unknowns (primal-dual pair), the right-hand side vector (residual forces, non-penetration functions and complementarity functions) and the stiffness matrix leads to the following iterative global system of equations:

$$\mathbf{K}^{\Bbbk}\left[\Delta\mathbf{d}^{\Bbbk}+\mathbf{z}^{\Bbbk+1}\right]=-\left[\mathbf{r}+\tilde{\mathbf{g}}+\tilde{\mathbf{h}}+\mathbf{C}_{\tau}\right]^{\Bbbk}. \tag{5.18}$$

Then, subdividing the surface domain into the five different subsets $\{\mathcal{N},\ \mathcal{M},\ \mathcal{I},\ \mathcal{Q},\ \mathcal{L}\}$, the following equation system is obtained,

$$\begin{bmatrix}
\mathbf{K}_{\mathcal{N}\mathcal{N}} & \mathbf{K}_{\mathcal{N}\mathcal{M}} & \mathbf{K}_{\mathcal{N}\mathcal{I}} & \mathbf{K}_{\mathcal{N}\mathcal{Q}} & \mathbf{K}_{\mathcal{N}\mathcal{L}} & \mathbf{0} & \mathbf{0} & \mathbf{0} \\
\mathbf{K}_{\mathcal{M}\mathcal{N}} & \tilde{\mathbf{K}}_{\mathcal{M}\mathcal{M}} & \tilde{\mathbf{K}}_{\mathcal{M}\mathcal{I}} & \tilde{\mathbf{K}}_{\mathcal{M}\mathcal{Q}} & \tilde{\mathbf{K}}_{\mathcal{M}\mathcal{L}} & -\mathbf{M}_{\mathcal{I}}^{T} & -\mathbf{M}_{\mathcal{Q}}^{T} & -\mathbf{M}_{\mathcal{L}}^{T} \\
\mathbf{K}_{\mathcal{I}\mathcal{N}} & \tilde{\mathbf{K}}_{\mathcal{I}\mathcal{M}} & \tilde{\mathbf{K}}_{\mathcal{I}\mathcal{I}} & \tilde{\mathbf{K}}_{\mathcal{I}\mathcal{Q}} & \tilde{\mathbf{K}}_{\mathcal{I}\mathcal{L}} & \mathbf{D}_{\mathcal{I}} & \mathbf{0} & \mathbf{0} \\
\mathbf{K}_{\mathcal{Q}\mathcal{N}} & \tilde{\mathbf{K}}_{\mathcal{Q}\mathcal{M}} & \tilde{\mathbf{K}}_{\mathcal{Q}\mathcal{I}} & \tilde{\mathbf{K}}_{\mathcal{Q}\mathcal{Q}} & \tilde{\mathbf{K}}_{\mathcal{Q}\mathcal{L}} & \mathbf{0} & \mathbf{D}_{\mathcal{Q}} & \mathbf{0} \\
\mathbf{K}_{\mathcal{L}\mathcal{N}} & \tilde{\mathbf{K}}_{\mathcal{L}\mathcal{M}} & \tilde{\mathbf{K}}_{\mathcal{L}\mathcal{I}} & \tilde{\mathbf{K}}_{\mathcal{L}\mathcal{Q}} & \tilde{\mathbf{K}}_{\mathcal{L}\mathcal{L}} & \mathbf{0} & \mathbf{0} & \mathbf{D}_{\mathcal{L}} \\
\mathbf{0} & \mathbf{0} & \mathbf{0} & \mathbf{0} & \mathbf{0} & \mathbf{I}_{\mathcal{I}} & \mathbf{0} & \mathbf{0} \\
\mathbf{0} & \tilde{\mathbf{M}}_{\mathcal{A}} & \tilde{\mathbf{D}}_{\mathcal{A}\mathcal{I}} & \tilde{\mathbf{D}}_{\mathcal{A}\mathcal{Q}} & \tilde{\mathbf{D}}_{\mathcal{A}\mathcal{L}} & \mathbf{0} & \mathbf{0} & \mathbf{0} \\
\mathbf{0} & \mathbf{H}_{\mathcal{Q}} & \mathbf{F}_{\mathcal{Q}\mathcal{I}} & \mathbf{F}_{\mathcal{Q}\mathcal{Q}} & \mathbf{F}_{\mathcal{Q}\mathcal{L}} & \mathbf{0} & \mathbf{Q}_{\mathcal{Q}} & \mathbf{0} \\
\mathbf{0} & \mathbf{J}_{\mathcal{L}} & \mathbf{G}_{\mathcal{L}\mathcal{I}} & \mathbf{G}_{\mathcal{L}\mathcal{Q}} & \mathbf{G}_{\mathcal{L}\mathcal{L}} & \mathbf{0} & \mathbf{0} & \mathbf{L}_{\mathcal{L}}
\end{bmatrix}
\cdot
\begin{bmatrix}
\Delta\mathbf{d}_{\mathcal{N}} \\ \Delta\mathbf{d}_{\mathcal{M}} \\ \Delta\mathbf{d}_{\mathcal{I}} \\ \Delta\mathbf{d}_{\mathcal{Q}} \\ \Delta\mathbf{d}_{\mathcal{L}} \\ \mathbf{z}_{\mathcal{I}} \\ \mathbf{z}_{\mathcal{Q}} \\ \mathbf{z}_{\mathcal{L}}
\end{bmatrix}$$

$$= \left[\mathbf{r}_{\mathcal{N}},\ \mathbf{r}_{\mathcal{M}},\ \mathbf{r}_{\mathcal{I}},\ \mathbf{r}_{\mathcal{Q}},\ \mathbf{r}_{\mathcal{L}},\ \mathbf{0},\ \tilde{\mathbf{g}}_{\mathcal{A}}+\tilde{\mathbf{h}}_{\mathcal{A}},\ \{\mathbf{C}_{\tau}\}_{\mathcal{Q}},\ \{\mathbf{C}_{\tau}\}_{\mathcal{L}}\right]^{T}. \tag{5.19}$$

The matrices $\mathbf{K}$ and $\tilde{\mathbf{C}}$ contain the linearization of the internal force vector and the contact force vector, respectively. The blocks $\tilde{\mathbf{K}}_{\imath\jmath}$ are the sum of the aforementioned matrices, for different combinations of subsets $\{\imath,\jmath\in\mathcal{M}\cup\mathcal{S}\}$,

$$\tilde{\mathbf{K}}_{\imath\jmath}=\mathbf{K}_{\imath\jmath}+\tilde{\mathbf{C}}_{\imath\jmath}. \tag{5.20}$$

The first five rows of the system (5.19) represent the force equilibrium, Equation (4.60). The sixth row enforces the contact constraints over the inactive nodes, while the seventh row is concerned with the non-penetration condition on the active nodes. Matrices $\tilde{\mathbf{D}}$ and $\tilde{\mathbf{M}}$ are obtained from the linearization of Equation (4.43) and Equation (4.44), respectively. Eight and Ninth rows enforce the tangential conditions for both sticking, $\mathcal{Q}$, and sliding, $\mathcal{L}$, contact nodes.

The global system depicted in Equation (5.19) displays an increase of bandwidth (lagrangian multipliers) from the initial non-constrained form. However, the key asset of introducing a dual basis for the lagrangian multipliers is that they can be locally removed from Equation (5.19), such that,

$$\mathbf{z}=-\mathbf{D}^{-1}\left[\mathbf{r}_{\mathcal{S}}+\tilde{\mathbf{K}}_{\mathcal{S}\mathcal{N}}\Delta\mathbf{d}_{\mathcal{N}}+\tilde{\mathbf{K}}_{\mathcal{S}\mathcal{M}}\Delta\mathbf{d}_{\mathcal{M}}+\tilde{\mathbf{K}}_{\mathcal{S}\mathcal{S}}\Delta\mathbf{d}_{\mathcal{S}}\right]. \tag{5.21}$$

Hence, the equations related to the enforcement of contact constraints on the inactive set can be eliminated from the system and a pure displacement problem is obtained,

$$\begin{bmatrix}
\mathbf{K}_{\mathcal{N}\mathcal{N}} & \mathbf{K}_{\mathcal{N}\mathcal{M}} & \mathbf{K}_{\mathcal{N}\mathcal{I}} & \mathbf{K}_{\mathcal{N}\mathcal{Q}} & \mathbf{K}_{\mathcal{N}\mathcal{L}} \\
\hat{\mathbf{K}}_{\mathcal{A}\mathcal{N}} & \hat{\mathbf{K}}_{\mathcal{A}\mathcal{M}} & \hat{\mathbf{K}}_{\mathcal{A}\mathcal{I}} & \hat{\mathbf{K}}_{\mathcal{A}\mathcal{Q}} & \hat{\mathbf{K}}_{\mathcal{A}\mathcal{L}} \\
\mathbf{K}_{\mathcal{I}\mathcal{N}} & \tilde{\mathbf{K}}_{\mathcal{I}\mathcal{M}} & \tilde{\mathbf{K}}_{\mathcal{I}\mathcal{I}} & \tilde{\mathbf{K}}_{\mathcal{I}\mathcal{Q}} & \tilde{\mathbf{K}}_{\mathcal{I}\mathcal{L}} \\
\mathbf{0} & \tilde{\mathbf{M}}_{\mathcal{A}} & \tilde{\mathbf{D}}_{\mathcal{A}\mathcal{I}} & \tilde{\mathbf{D}}_{\mathcal{A}\mathcal{Q}} & \tilde{\mathbf{D}}_{\mathcal{A}\mathcal{L}} \\
\check{\mathbf{K}}_{\mathcal{Q}\mathcal{N}} & \check{\mathbf{K}}_{\mathcal{Q}\mathcal{M}}-\mathbf{H}_{\mathcal{Q}} & \check{\mathbf{K}}_{\mathcal{Q}\mathcal{I}}-\mathbf{F}_{\mathcal{Q}\mathcal{I}} & \check{\mathbf{K}}_{\mathcal{Q}\mathcal{Q}}-\mathbf{F}_{\mathcal{Q}\mathcal{Q}} & \check{\mathbf{K}}_{\mathcal{Q}\mathcal{L}}-\mathbf{F}_{\mathcal{Q}\mathcal{L}} \\
\check{\mathbf{K}}_{\mathcal{L}\mathcal{N}} & \check{\mathbf{K}}_{\mathcal{L}\mathcal{M}}-\mathbf{J}_{\mathcal{L}} & \check{\mathbf{K}}_{\mathcal{L}\mathcal{I}}-\mathbf{G}_{\mathcal{L}\mathcal{I}} & \check{\mathbf{K}}_{\mathcal{L}\mathcal{Q}}-\mathbf{G}_{\mathcal{L}\mathcal{Q}} & \check{\mathbf{K}}_{\mathcal{L}\mathcal{L}}-\mathbf{G}_{\mathcal{L}\mathcal{L}}
\end{bmatrix}$$

$$\cdot \begin{bmatrix} \Delta\mathbf{d}_{\mathcal{N}} \\ \Delta\mathbf{d}_{\mathcal{M}} \\ \Delta\mathbf{d}_{\mathcal{I}} \\ \Delta\mathbf{d}_{\mathcal{Q}} \\ \Delta\mathbf{d}_{\mathcal{L}} \end{bmatrix} = - \begin{bmatrix} \mathbf{r}_{\mathcal{N}} \\ \mathbf{r}_{\mathcal{M}} + \left[\mathbf{D}_{\mathcal{A}}^{-1}\mathbf{M}_{\mathcal{A}}\right]^{T}\mathbf{r}_{\mathcal{A}} \\ \mathbf{r}_{\mathcal{I}} \\ \tilde{\mathbf{g}}_{\mathcal{A}} + \tilde{\mathbf{h}}_{\mathcal{A}} \\ \mathbf{Q}_{\mathcal{Q}}\mathbf{D}_{\mathcal{Q}}^{-1}\mathbf{r}_{\mathcal{Q}} - \{\mathbf{C}_{\tau}\}_{\mathcal{Q}} \\ \mathbf{L}_{\mathcal{L}}\mathbf{D}_{\mathcal{L}}^{-1}\mathbf{r}_{\mathcal{L}} - \{\mathbf{C}_{\tau}\}_{\mathcal{L}} \end{bmatrix} \tag{5.22}$$

where the two matricial functions, $\hat{\mathbf{K}}_{\mathcal{A}\jmath}$ and $\check{\mathbf{K}}_{\imath\jmath}$, are introduced to facilitate the notation of this condensed system. They are constructed from the primary matrices in Equation (5.19) and described by suitable combinations of the subsets $\imath$ and $\jmath$, as follows,

$$\hat{\mathbf{K}}_{\mathcal{A}\jmath} = \begin{cases} \mathbf{K}_{\mathcal{M}\jmath} + \mathbf{D}_{\mathcal{A}}^{-1}\mathbf{M}_{\mathcal{A}}^{T}\mathbf{K}_{\mathcal{A}\jmath} & \text{for} \quad \{\jmath = \mathcal{N}\}, \\ \tilde{\mathbf{K}}_{\mathcal{M}\jmath} + \mathbf{D}_{\mathcal{A}}^{-1}\mathbf{M}_{\mathcal{A}}^{T}\tilde{\mathbf{K}}_{\mathcal{A}\jmath} & \text{for} \quad \{\jmath \neq \mathcal{N}\}. \end{cases} \tag{5.23}$$

$$\check{\mathbf{K}}_{\imath\jmath} = \begin{cases} \mathbf{P}_{\imath}\mathbf{D}_{\imath}^{-1}\mathbf{K}_{\imath\jmath} & \text{for} \quad \{\imath = \mathcal{Q}\} \wedge \{\jmath = \mathcal{N}\}, \\ \mathbf{P}_{\imath}\mathbf{D}_{\imath}^{-1}\tilde{\mathbf{K}}_{\imath\jmath} & \text{for} \quad \{\imath = \mathcal{Q}\} \wedge \{\jmath \neq \mathcal{N}\}, \\ \mathbf{L}_{\imath}\mathbf{D}_{\imath}^{-1}\mathbf{K}_{\imath\jmath} & \text{for} \quad \{\imath = \mathcal{L}\} \wedge \{\jmath = \mathcal{N}\}, \\ \mathbf{L}_{\imath}\mathbf{D}_{\imath}^{-1}\tilde{\mathbf{K}}_{\imath\jmath} & \text{for} \quad \{\imath = \mathcal{L}\} \wedge \{\jmath \neq \mathcal{N}\}. \end{cases} \tag{5.24}$$

At last, the condensed equation system can be solved for the incremental nodal displacement, $\Delta\mathbf{d}$, and then an appropriate integration algorithm (Section 2.4.2)can update the strains and stresses. In the nested scheme, the wear effects (i.e. computation of the dissipated energy, wear volume and wear depth) are accounted for after the solution of the residual problem. Therefore, the matricial representation of the nested scheme can be recovered by eliminating the wear depth vector, $\tilde{\mathbf{h}}$, from the (Equation 5.22). It is important to emphasize that, during the wear evaluation procedure (i.e. step 8 of the nested scheme and 3 the single step strategy), the stiffness matrices of all finite elements involved in the wear balance are directly affected by the wear depth. This consideration gives a rather physical sense to the wear evaluation, since changes in the solid's stiffness yields repercussions into the majority of the problem's variables.

In the following chapters, an extensive comparison of *nested* and the *single* step fully implicit approaches is conducted throughout numerical problems containing friction, large inelastic strain and fretting wear evolution. Comparisons with the results provided by the Penalty method are presented. A brief description of this method is given in Appendix C

Chapter 6

Numerical examples

In this Chapter, a comprehensive set of numerical examples is presented: six are two-dimensions and three are on three dimensions. These problems are used to demonstrate the accuracy and efficiency of the Dual-Mortar approach against the traditional node-to-segment penalty contact formulation, widely used in commercial finite element codes. Furthermore, the performance of the solution methods described in Section 5.2 will also be addressed for frictional contact problems with deformable bodies undergoing finite strains with inelastic material behavior and fretting wear.

In the first two problems, several enforcement methods are discussed. Problems three to five are focused on the computation of the tangential forces in the presence of finite strains, while the remaining examples are mainly concerned with the fretting wear phenomena. In summary, the examples are presented in such a way that the degree of nonlinearity (i.e. deformability, friction, inelastic material behavior, presence of fretting wear, geometrical shape, etc) increases problem by problem.

Table 6.1: Mechanical properties of the materials employed.

	Mechanical properties					
Materials	E(GPa)	G(GPa)	ν	σ_y(MPa)	A(MPa)	b
Pure aluminum	68.96	26	0.32	31	1574	0.220
Aluminum alloy	71.15	26	0.30	370	550	0.223
Hard steel	210	76	0.33	830	600	0.210
Elastomer	4	2.8	0.29	510	410	0.08
Tungsten alloy	400	85	0.33	880	700	0.205
Mild steel	200	75	0.3	490	585	0.25
Titanium	121	44	0.29	950	1470	0.14

Several materials were employed in this Chapter. In order to facilitate the readability, names were given to some of them: aluminum alloy, pure aluminum, elastomer, hard steel, tungsten alloy, mild steel and titanium. Their mechanical properties and coefficients A and b for the solution of the Ludwik-Hollomon equation ($\sigma = \sigma_y + A\epsilon^b$) are listed in Table 6.1. All the simulations presented in this section were performed with an implicit quasi-static finite element framework. Unless oth-

erwise mentioned, the values chosen for the Penalty multipliers were $\epsilon_n = \epsilon_\tau = 10^4$ and for the complementarity parameters were $c_\eta = c_\tau = 1$.

6.1 Pressurized hollow spheres

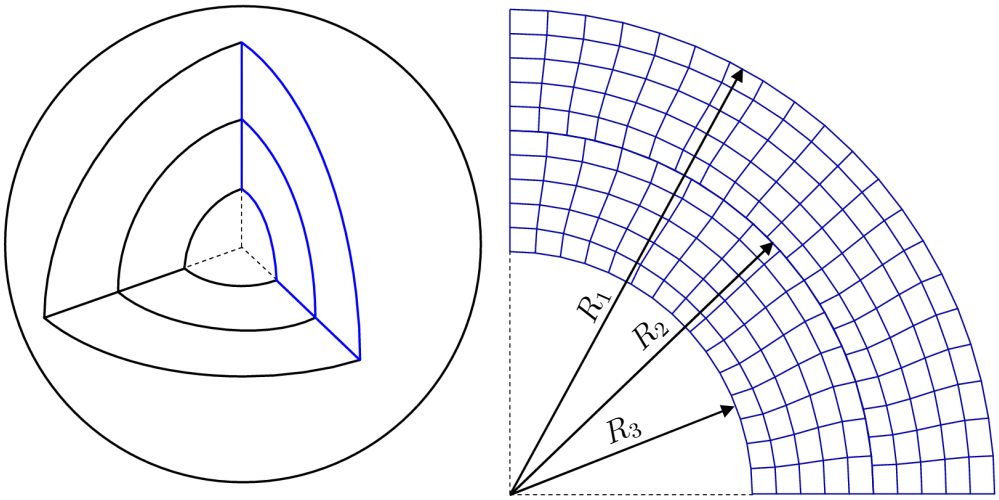

Figure 6.1: Pressurized hollow spheres - geometry and FE discretization.

The first example is the two-dimensional simplification of the pressurized spheres contact problem presented in [51]. In this problem, the contact surfaces are tied. Therefore, as long the contact forces are transmitted properly, the two spheres are expected to behave as a single structure. The simulation is performed assuming y-axial symmetry, see Figure 6.1.

The dimensions of the spheres are: $R_1 = 20$mm, $R_2 = 15$mm and $R_3 = 10$mm. A distributed pressure of 690MPa is applied to the inner sphere within 50 equal pseudo-time increments of $\Delta P = 13.8$MPa. At the final step, the whole structure is expected to be under plastic deformation. The material chosen for both spheres was the Aluminum alloy and no friction is considered in this example.

The results for both methods (i.e. Penalty method and Dual-Mortar single step strategy) have a good agreement during most part of the simulation. Figure 6.2 shows the results obtained for the equivalent stress distribution at the last step of the simulation with the single step dual mortar method. There was no appreciable difference in the equivalent stress contour between both methods. Nevertheless, the same conclusion does not hold for the enforcement of contact constraints. In fact, there was no relative displacement between the contact surfaces while the deformation remained within the elastic domain, which occurs for loads below 310MPa. However, the value initially chosen for the penalty multiplier is no longer large enough to enforce the contact constraints as soon as plastic strains are reached. This led to the small penetration shown in Figure 6.3b. Increasing the normal penalty multiplier, ϵ_η, to 10^7 improves the results obtained by the method, which become very similar to the ones obtained by the Dual-Mortar method, see Figure 6.3a. Nevertheless,

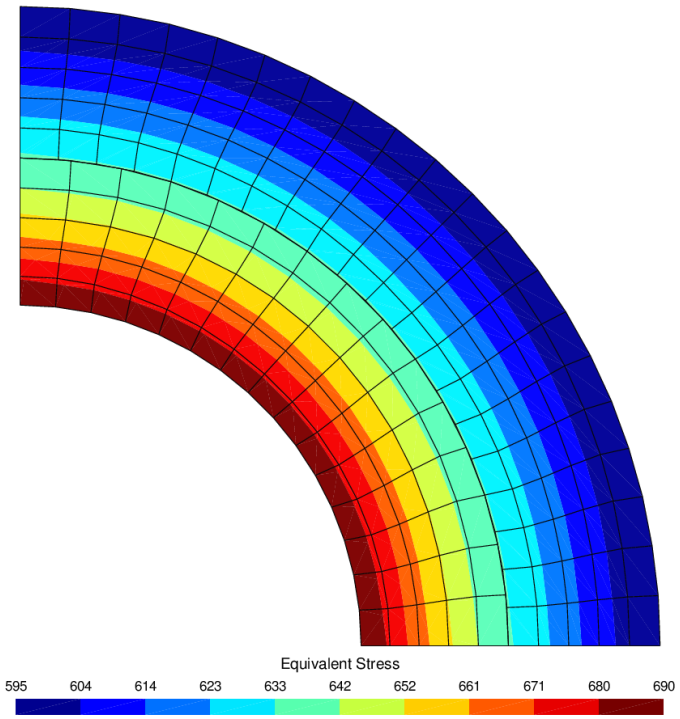

Figure 6.2: Pressurized hollow spheres - equivalent stress distribution for the Dual Mortar method.

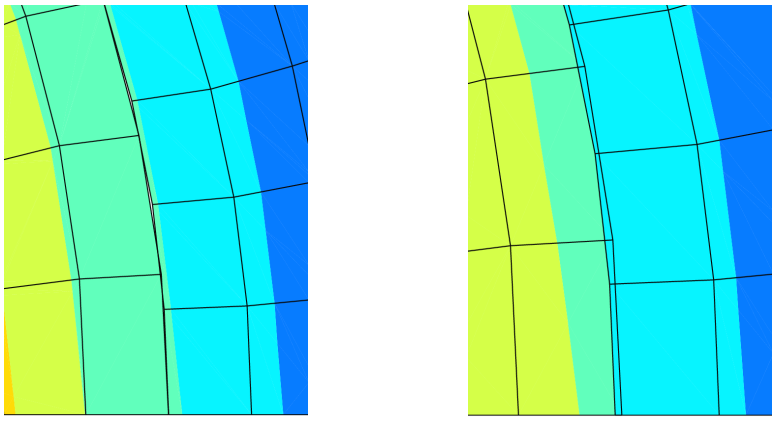

(a) Dual-Mortar method (b) Penalty method

Figure 6.3: Pressurized hollow spheres - contact interface.

due to this increase of the normal penalty multiplier the first increments presented convergence difficulties since the stiffness matrix becomes slightly ill-conditioned. In this example, it became clear that the Dual Mortar method was able to enforce the contact constraints more accurately and efficiently over the entire loading path. Two patch tests for the evaluation of the constraint enforcement are presented in the Appendix D.

6.2 Disc in contact with a half ring

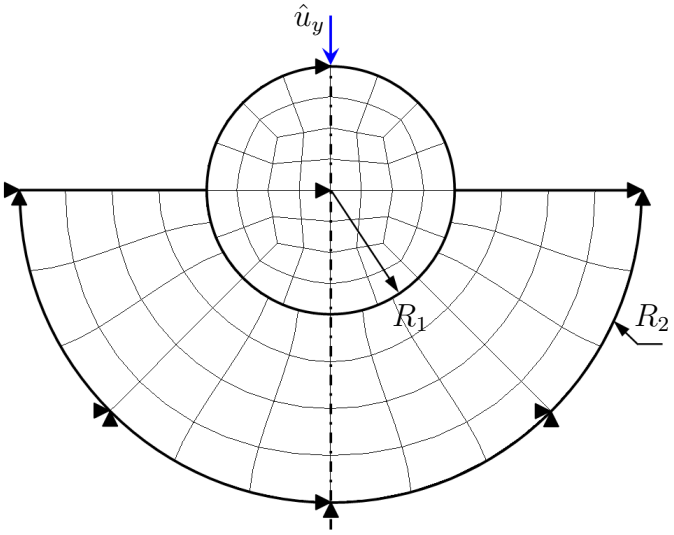

Figure 6.4: Disc in contact with a half ring - geometry and FE discretization

This example features the contact between a cylinder disc and a half ring. This problem was employed to study surface smoothing strategies by M. Tur et al. [77]. Here, it is used to study the precision of the enforcement method in the solution of problems with curved surfaces. Figure 6.4 shows the problem geometry and the mesh discretization adopted.

The dimensions of this problem are: disc outer radius/half ring inner radius, $R_1 = 50$mm; Half ring outer radius, $R_2 = 125$mm. The solids are described by the Neo-Hookean material model with the Young's modulus for the disc being $E_1 = 10^5$MPa while the half ring have a Young's modulus of $E_2 = 10^3$MPa. Poisson ratio for both bodies are equal to 0.3. A displacement equal to $\hat{u}_y = -90$mm is applied to the disc, this load is divided into 20 equal pseudo-time increments. Frictionless contact is assumed and the value chosen for the normal complementarity parameter was $c_\eta = 10^3$. During this analysis a comparison of four different enforcement methods is addressed: a) standard mortar method, b) dual mortar method, c) quadratic dual mortar method, d) smooth formulation by M. Tur et al. [77].

In order to employ an energy approach to evaluate the fretting wear mechanics of a contact problem, it is crucial that the contact forces are correctly computed during the whole simulation. The slightest error on the enforcement of constraints can lead to a significant variation of the wear depth when a large number of loading cycles occurs. Therefore, the objective of this example is to verify if this requirement is meet, by analyzing the contact pressure distribution over the contact zone. Figure 6.5 and Figure 6.6show a side-by-side comparison for the first steps of the simulation.

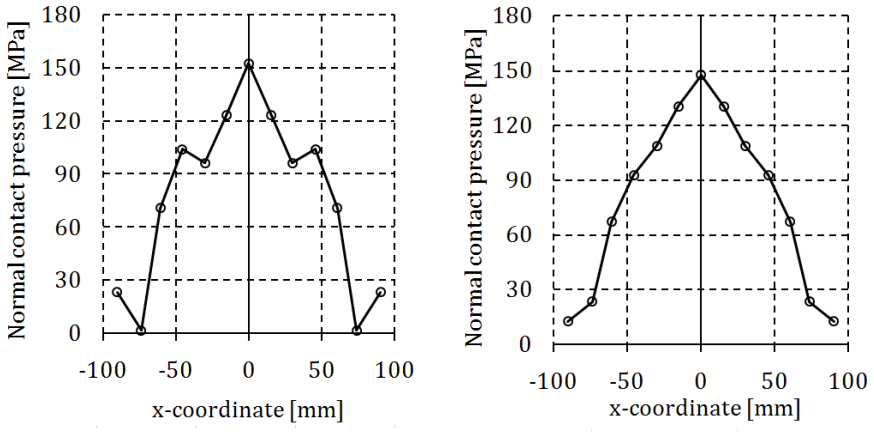

(a) T=1

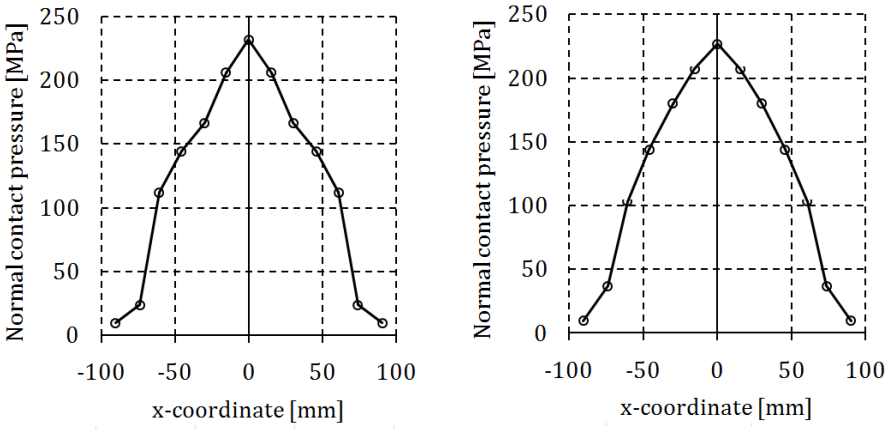

(b) T=2

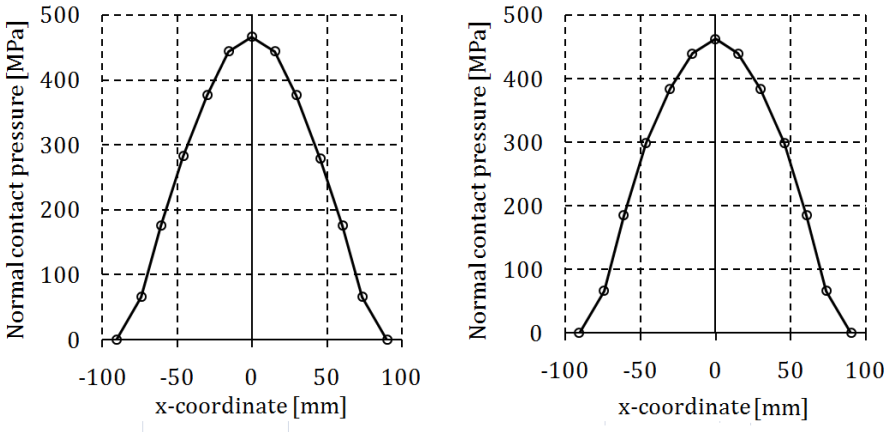

(c) T=5

Figure 6.5: Disc in contact with a half ring - Contact pressure distribution – mortar standard basis (left) vs mortar dual basis (right).

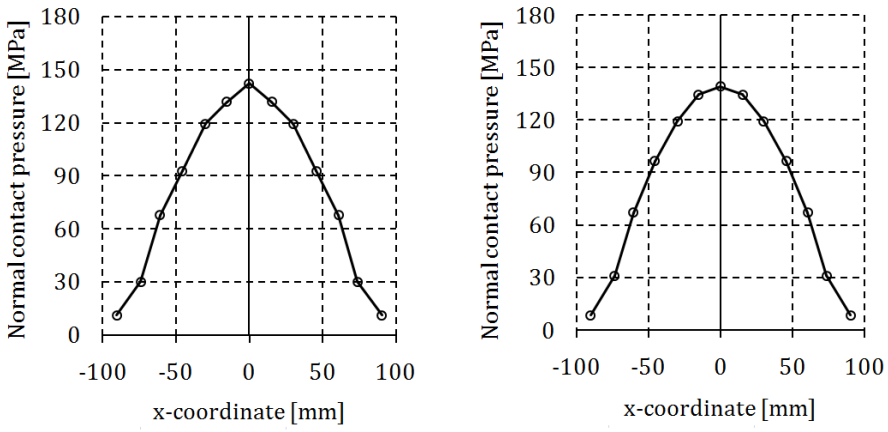

(a) T=1

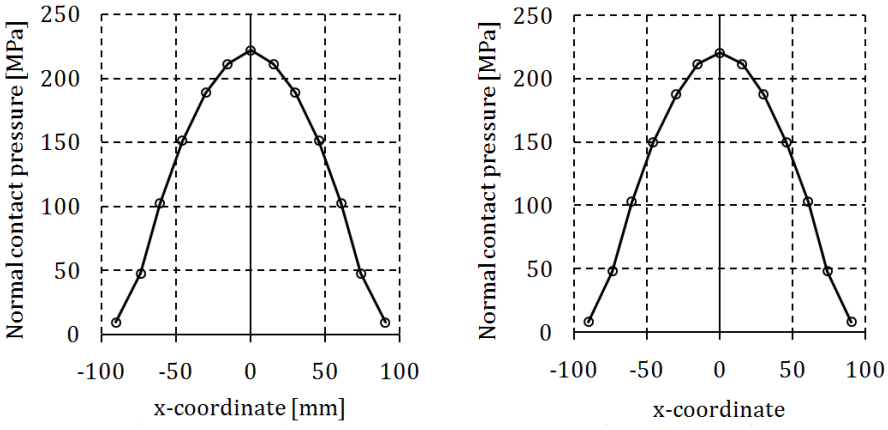

(b) T=2

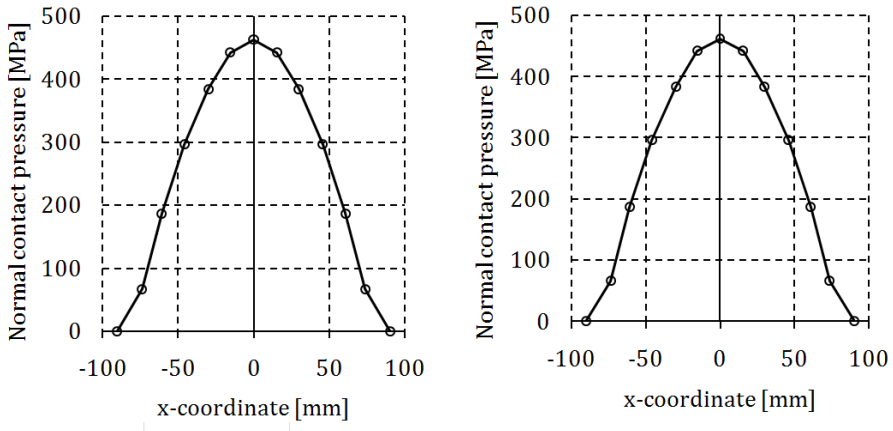

(c) T=5

Figure 6.6: Disc in contact with a half ring - Contact pressure distribution – mortar dual basis with quadratic elements (left) vs smoothing [77] (right).

Despite the fact that all aforementioned methods provide a correct value and a smooth distribution of the contact pressure at the end of the simulation (as seen

in Figures 6.5(c) and 6.6(c)), there is a direct relation between the level of surface discretization and the smoothness of the pressure distribution. For the first increment, it is possible to conclude that the mortar method with dual basis garantees a better enforcement of the contact than the standard basis. Furthermore, it has a performance equivalent to the smoothing strategy. Therefore, in cases where multiple loading stages occurs, enforcing the contact conditions with the standand mortar method would require the selection of a smoother mesh and/or significantly smaller increments in order to have a precise contact pressure distribution.

6.3 Conical extrusion

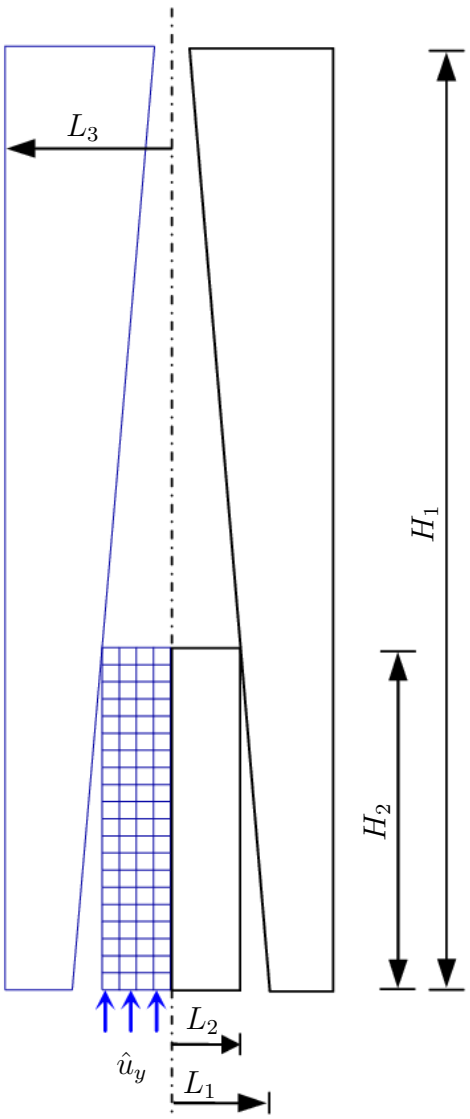

(a) Geometry and FE discretization.

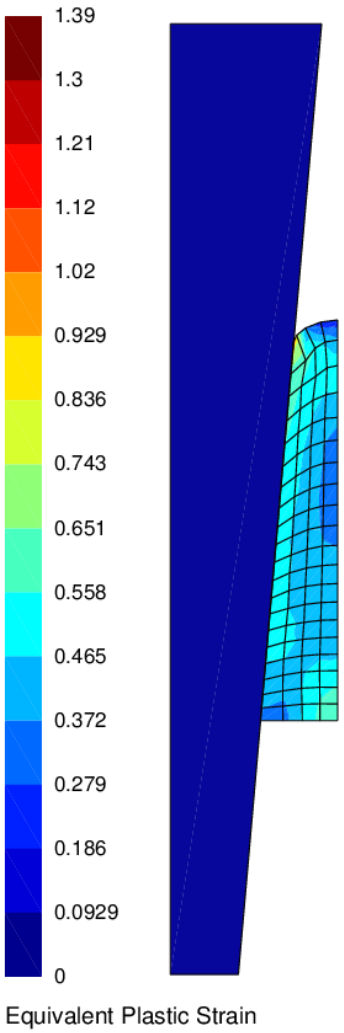

(b) Effective plastic strain contour at $\hat{u}_y = 177.8$mm.

Figure 6.7: Conical extrusion - initial conditions and numerical results.

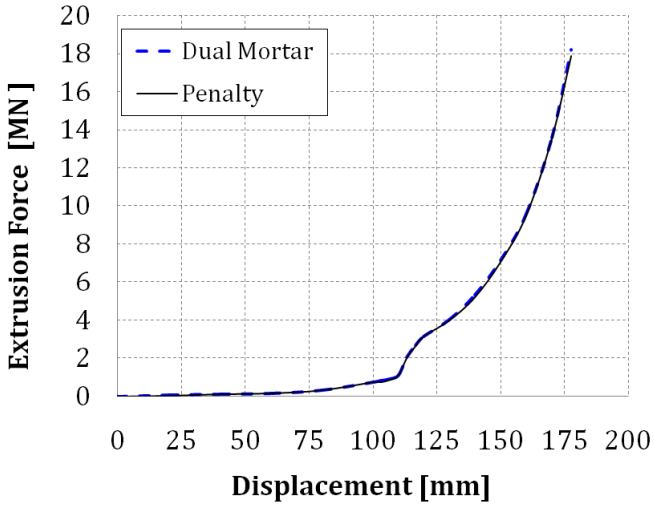

Figure 6.8: Conical extrusion - evolution of the extrusion force.

In this example, the frictional elasto-plastic stress analysis of a cylindrical billet [71] is presented. The billet is pushed across a total distance of $\hat{u}_y = 177.8$mm through a rigid conical die, which has a wall angle of 5 degrees, see Figure 6.7(a). The geometrical dimensions for this problem are: $H_1 = 700$mm, $H_2 = 254$mm, $L_1 = 73.02$mm, $L_2 = 50.8$mm, $L_3 = 123.02$mm. The billet is discretized with 80 4-noded F-bar elements.

Due to the presence of high frictional contact forces and the development of finite plastic strains in the billet, this example will allow the assessment of the performance of Penalty and the Dual-Mortar methods under finite frictional sliding coupled with finite strain inelastic material behavior. In particular, the displacement field of the billet, the evolution of the extrusion and tangential forces and the distribution of the plastic strain, will be analyzed for both methods. Material properties of the *pure aluminum* employed for this simulation are presented in Table 6.1.

Sliding forces are the principal cause of deformation in this example and therefore shear effects over the contact surface are expected. The die is regarded as a rigid body and the coefficient of friction adopted was $\mu = 0.1$. The values for the penalty multipliers selected for this problem were $\epsilon_\eta = 10^8$ and $\epsilon_\tau = 10^5$. In the simulation, the displacement load applied was divided into 200 increments. The equivalent plastic strain distribution at the final step obtained by the single step strategy is shown in Figure 6.7(b).

As expected, the higher plastic deformation level is found at the upper left side of the billet with a maximal value of 1.39. There was no appreciable difference in the equivalent plastic strain contour obtained by the two methods. The final contact surface length is equal to 257.33mm. A graphical representation of the extrusion force, measured from the reaction at the billet bottom, is shown in Figure 6.8. The difference between the two methods is negligible. The convergence rate of both methods is listed in Table 6.2 for increments 1, 100 and 200.

Nevertheless, the evolution of the frictional force obtained with the Penalty

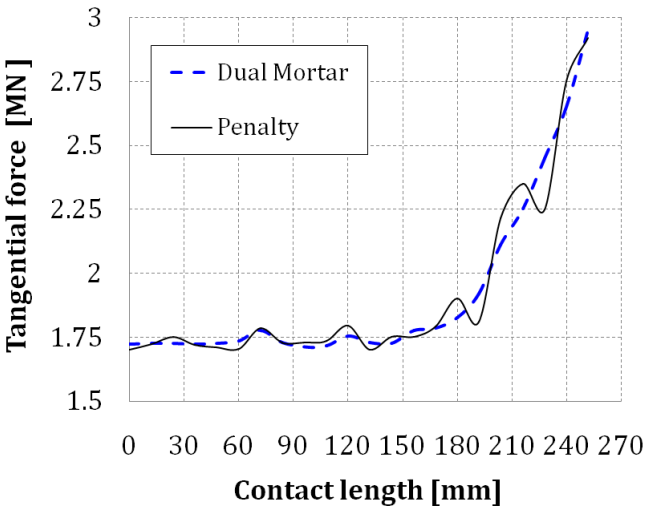

Figure 6.9: Conical extrusion - evolution of the frictional force.

method, see Figure 6.9, shows the typical non-physical oscillation due to the non-smoothness of finite element discretization along the contact surface. This drawback is mitigated by the continuous normal field provided by the Mortar segmentation, where no oscillations are observed. One advantage of performing the simulation with a rigid body is that, since the non-mortar surface is composed by a single segment of the die, the segmentation does not change, even when plastic strains are in place. Therefore, the active set is kept the same during the whole simulation, which provides optimal convergence rates for the Dual-Mortar method, as seen in Table 6.2.

6.4 Frictional beam problem

The analysis of an elasto-plastic frictional beam contact problem [88] is presented next. The objective of this analysis is to investigate the influence of the parameters c_η, c_τ, employed in the definition of the non-complementarity conditions of the Dual-Mortar method, together with the parameters ϵ_η and ϵ_τ, employed in the enforcement of contact constraints of the NTS-Penalty method, when finite frictional sliding and finite strain elasto-plastic material behavior are present. Due to the different sources of nonlinearity involved (geometrical, material and contact), this is also a good problem to test the robustness of the approach presented.

The problem is composed by two beams: a straight beam and a curved beam, which are represented in Figure 6.10. The straight beam is simply supported and the curved beam is fixed on the left end in the yy direction and subjected to a vertical displacement $\hat{u}_y = 1.2t$ at the right end. In addition, a prescribed horizontal displacement of $\hat{u}_x = 2.0t$ is applied to both left and right ends. The geometrical dimensions are: $L_1 = 30$mm, $L_2 = 23$mm, $H = 1.75$mm, $R_1 = 10$mm and $R_2 = 8$mm. Due to the curvature and boundary conditions the curved beam has a high structural stiffness and, therefore, the straight beam is more prone to deform.

Table 6.2: Conical extrusion - residual norm convergence behavior.

		Penalty	Dual Mortar
t_n	$\Bbbk$	Relative Residual Norm (%)	
001	1	0.612567E+02	0.110718E+01
	2	0.179956E+02	0.806609E+00
	3	0.845863E+00	0.173512E-02
	4	0.233792E-02	0.990222E-07
	5	0.950268E-06	0.192286E-11
	6	0.326588E-11	-
100	1	0.856247E+03	0.280271E+01
	2	0.625483E+01	0.158554E+01
	3	0.215140E-02	0.436638E-01
	4	0.269871E-04	0.274675E-04
	5	0.112124E-08	0.246126E-10
200	1	0.425783E+02	0.862577E+01
	2	0.914758E+00	0.150099E+00
	3	0.667821E-02	0.546990E-01
	4	0.299631E-04	0.734911E-04
	5	0.141457E-06	0.149939E-09
	6	0.784265E-08	-
$\sum(\Bbbk)$		1215	981

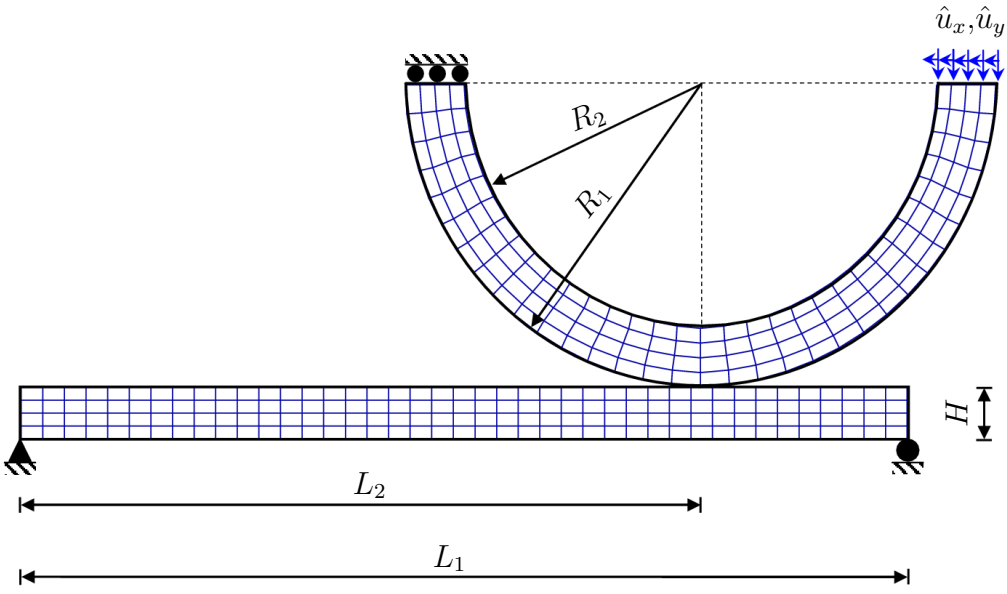

Figure 6.10: Frictional beam problem - geometry and FE discretization.

Both beams are assumed to be made of aluminum alloy, whose properties are listed in Table 6.1, with a coefficient of friction equal to $\mu = 0.3$. The total prescribed displacement, which is set to be equal to $\hat{u}_x = 16$mm, was applied over 320 equally

spaced pseudo-time increments of $\Delta t = 0.025$.

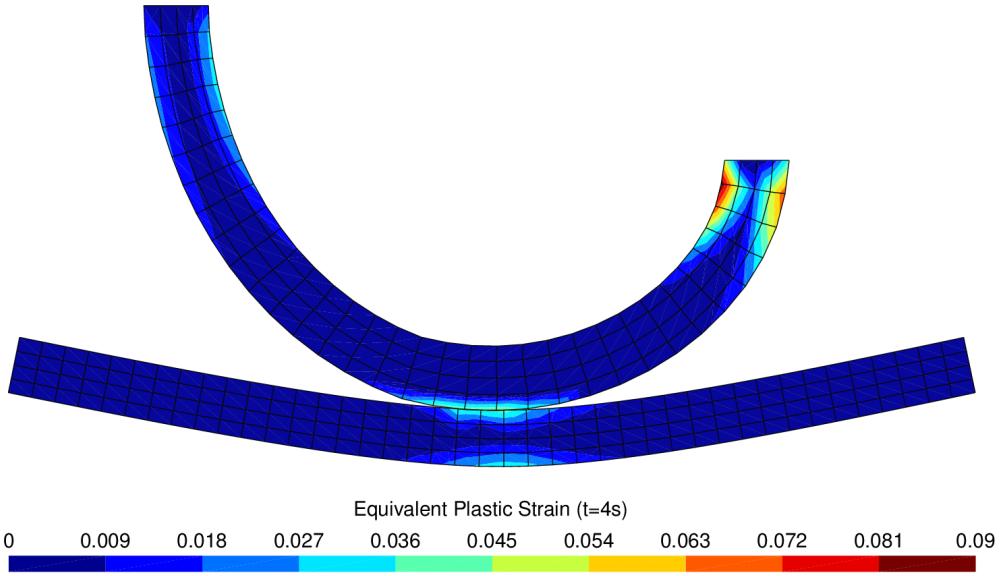

Figure 6.11: Frictional beam problem - effective plastic strain at t=4s.

6.4.1 Results and performance

The evolution of the effective plastic strain provided by the Dual Mortar method is shown in Figure 6.11 for t=4s and in Figure 6.12 for the final configuration at t=8s. There was no noticeable difference in the effective plastic strain contour between both methods. During the first 2 pseudo-seconds of the simulation, the majority of the displacement and deformation are undergone by the bottom beam. At t=4s, the contact surface already presents significant levels of plastic strain. The presence of high frictional force causes shear distortion of the finite elements on the contact region and the bending process induces the growth of the contact area.

At the end of the simulation (t=8s), the upper beam has considerable deformation levels at the right corner due to the prescribed displacement $\hat{u}_x$, while the lower beam shows moderate levels of strain at the contact surface. The spatial rate of convergence of the relative residual norm, for representative steps of this analysis, is shown in Table 6.3. In this table, it is possible to observe that the Penalty method is able to solve the entire problem when employing $\epsilon_\eta = \epsilon_\tau = 10^4$. However when the curved beam starts to experience high levels of plastic deformation, the convergence rate of this method is compromised (see increment 160 in Table 6.3).

On the other hand, the Dual-Mortar method converges reasonably well during all the simulation. Nevertheless, the convergence of the single iteration PDASS algorithm is also affected when the upper beam undergoes plastic strains. In particular, multiple attempts to find the correct subset for the mortar segmentation occur after a given configuration update, which leads to changes on the contact pairs and consequently the active set. In addition, the finite elements at the most outer-left

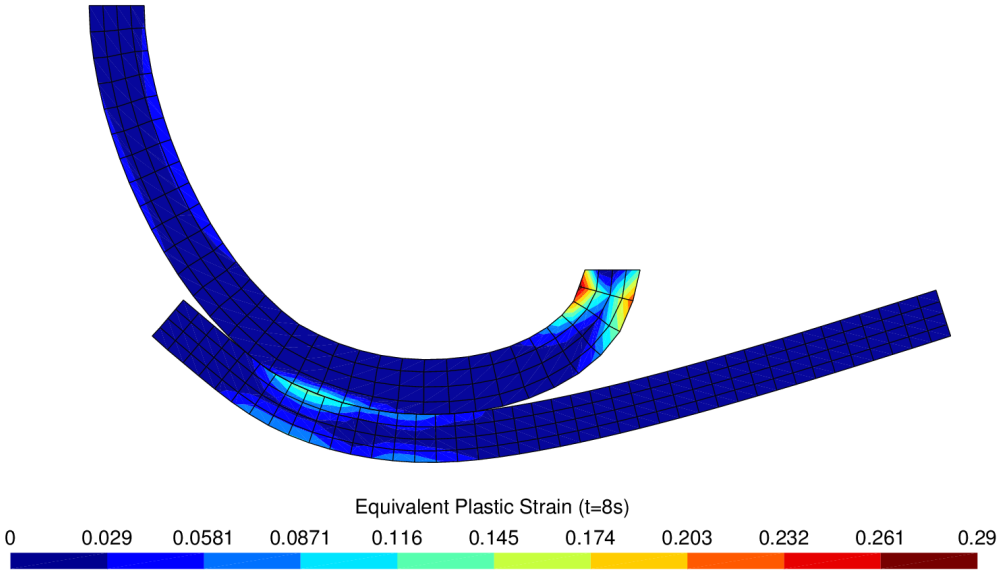

Figure 6.12: Frictional beam problem - effective plastic strain at t=8s.

section of the upper beam get significantly distorted due to the boundary conditions, leading to the computation of negative Jacobians during the analysis.

With regard to the computational time required for carrying out the analysis, it is possible to conclude that the total number of iterations to attain convergence with the NTS-Penalty method, for each increment, is always higher than the Dual-Mortar method. Although the computational cost of each iteration of the Penalty formulation is cheaper, the additional number of iterations makes the method more expensive. Furthermore, the NTS method also requires considerably smaller time steps in order to converge in both elastic and plastic domains when compared with the Dual-Mortar method which, in an overall sense, is significantly more efficient.

6.4.2 Influence of parameters c_η, c_τ and $\epsilon_\eta, \epsilon_\tau$

Finally, with this example, the influence of the parameters c_η and c_τ – introduced with the complementarity functions in Chapter 5 – is investigated. These parameters were defined within the context of small deformations in [41] and analyzed at finite strains in [33]. The parameter c_η is a positive constant that relates the different physical units of z_η and $\tilde{g}$. Therefore, it seems logical to choose c_η such that the values of z_η and $\tilde{g}$ are balanced and several authors [40, 41, 43, 62] have suggested c_η to be of the order of the Elasticity modulus of the contact bodies. The same reasoning applies to the positive constant c_τ, i.e. it is logical to choose c_τ such that z_τ and $\tilde{u}_\tau$ are balanced. Nevertheless, the conditions on the tangential directions that result from the applied Coulomb's friction law are also related to the parameter c_η. Consequently, c_τ is also suggested to reflect the material parameters of the contacting bodies [41, 62]. The convergence behavior of the single step PDASS algorithm for different values of c_η and c_τ is illustrated in Table 6.4. The number of Newton steps required to reach convergence for two representative steps, one within the elastic

Table 6.3: Frictional beam problem - residual norm convergence behavior.

		Penalty $\epsilon_\eta = \epsilon_\tau = 10^4$	Dual Mortar $c_\eta = c_\tau = 1$
t_n	$\mathbb{k}$	Relative Residual Norm (%)	
001	1	0.457532E+02	0.945446E+01
	2	0.145766E+00	0.298134E+01
	3	0.303347E-01	0.262611E-04
	4	0.198423E-02	0.444629E-10
	5	0.435333E-04	-
	6	0.254868E-10	-
160	1	0.412056E+02	0.145941E+01(*)
	2	0.211690E+00	0.112458E-01
	3	0.125627E-01	0.138134E-02
	4	0.506982E-02	0.138134E-02
	5	0.022463E-03	0.262611E-04
	6	0.174102E-04	0.444629E-10
	7	0.512961E-06	-
	8	0.512961E-09	-
320	1	0.842507E+01	0.226485E+01(*)
	2	0.631476E-01	0.286545E-01
	3	0.400189E-02	0.754524E-04
	4	0.229077E-03	0.917062E-08
	5	0.990173E-04	0.896271E-12
	6	0.303569E-06	-
	7	0.131313E-09	-
$\sum(\mathbb{k})$		2281	1756

(*) Change on the active set.

and other within the plastic domain, is investigated. It can be observed that, within the elastic domain, there is almost no degradation of the convergence rate for a wide range of c_η and c_τ. Therefore, the sensitivity of the algorithm, with regard to the choice of c_η and c_τ, is low within the elastic domain. For the plastic domain, there is still a reasonable range of c_η and c_τ that do not affect the convergence rate. Nevertheless, the spectrum of complementarity parameters for which there is no deterioration of the convergence rate is noticeably more limited.

The additional source of non-linearity caused by the material behavior significantly affects the number of iterations needed to achieve convergence and the number of active set changes. These results suggest that the values of c_η and c_τ should reflect the plastic material parameters of the bodies in contact.

It is important to emphasize that the choice of c_η and c_τ only enhances or deteriorates convergence of the Dual-Mortar method and not the accuracy of the results. On the other hand, the choice of penalty multipliers, ϵ_η and ϵ_τ, has a great influence on the accuracy of the method. In Table 6.5, the convergence behavior of the NTS-Penalty formulation for different values of ϵ_η and ϵ_τ is illustrated. Again, the

Table 6.4: Frictional beam problem - influence of the parameters c_η and c_τ.

	Elastic domain: $t_n = 10$					Plastic domain: $t_n = 300$				
	c_τ					c_τ				
c_n	10^{-2}	10^0	10^2	10^4	10^6	10^{-2}	10^0	10^2	10^4	10^6
10^{-2}	5	4	4	-	*	6	6	6	-	*
10^0	4	4	4	6	*	6	7(1)	7(1)	7(1)	*
10^2	4	4	5(1)	7(1)	*	7(1)	7(1)	7(1)	8(2)	*
10^4	5	5	6(1)	7(1)	*	7(1)	7(1)	9(3)	10(3)	*
10^6	*	*	8(1)	9(2)	*	*	*	*	*	*
(*) More than 10 iterations and 3 changes of active set.										

Table 6.5: Frictional beam problem - influence of the parameters ϵ_η and ϵ_τ.

	Elastic domain: $t_n = 10$				Plastic domain: $t_n = 300$			
	ϵ_τ				ϵ_τ			
ϵ_n	10^2	10^4	10^6	10^8	10^2	10^4	10^6	10^8
10^2	**	**	**	***	**	**	**	**
10^4	8	7	6	8	**	9	10	10
10^6	7	7	7	***	8	9	9	***
10^8	8	***	8	***	8	10	10	***
(**) Penetration over than 10% of the finite element height.								
(***) Locking/overconstraint.								

number of Newton steps needed to attain convergence for two representative steps, one elastic and one plastic, is investigated.

Within both the elastic and plastic domains, it is possible to observe the well-known behavior of the NTS-Penalty method. For low values of ϵ_η and ϵ_τ the penetration can be significant and the frictional constraints are not fulfilled. On the other hand, high values of these parameters lead to locking and/or overconstraint, which prevent the problem to be solved. Therefore, the selection of the penalty parameters is a compromise between the accuracy of the solution and finding a solution for the problem.

6.5 Cylinder-to-block problem

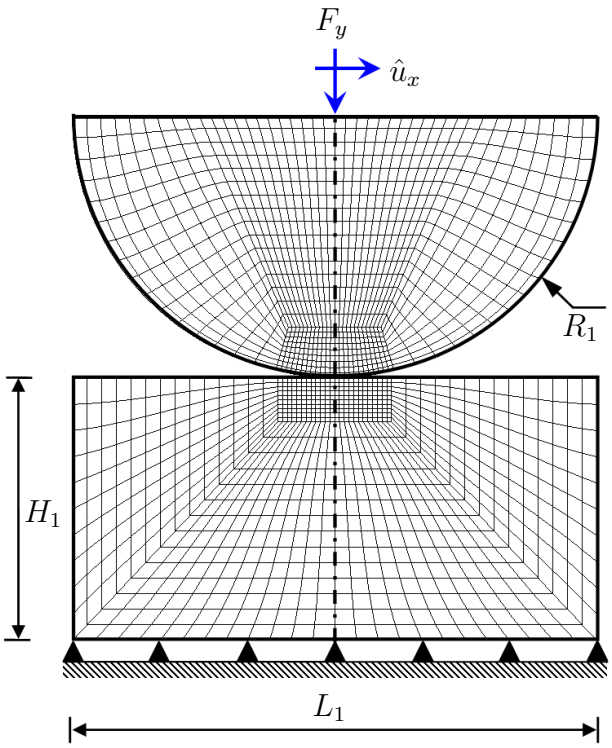

Figure 6.13: Cylinder-to-block problem - geometry and FE discretization.

The following problem is a well known benchmark widely employed for testing both contact and fretting formulations. It belongs to the Hertizian class of contact problems, which can be solved analytically. However, the analytical solution is only valid as long the deformation is kept within the elastic domain. It features a *Hard steel* cylinder that is pressed and pushed against an *aluminium alloy* block, whose properties are listed in Table 6.1. The initial contact area is very small (non-conforming contact point) and a curved contact surface is present. The simulation is conducted with the two-dimensional plane-strain assumption.

The geometry of the problem and finite element mesh, employed to discretize the geometry, are depicted in Figure 6.13. Radius of the cylinder is $R_1 = 50$mm while the dimensions of the block are $H_1 = 100$mm and $H_2 = 200$mm. A total number of 660 4-noded F-bar quadrilateral elements was employed to discretize the block and 888 elements for the discretization of the cylinder. A friction coefficient $\mu = 0.1$ is adopted in this analysis.

6.5.1 Equations for analytical solution

The analytical solution for this problem was derived from the Hertizian contact formulae [38, 46] for two cylinders, which defines the maximum contact pressure,

$P_{\max}$, the contact width, a, and the contact pressure along x-coordinate P as:

$$P_{\max} = \sqrt{\frac{FE^*}{2\pi R^*}} \ , \tag{6.1}$$

$$a = \sqrt{\frac{8FR^*}{\pi E^*}} \ , \tag{6.2}$$

$$P = P_{\max}\sqrt{1 - \left(\frac{x}{a}\right)} \ , \tag{6.3}$$

where the combined elasticity modulus, E^*, is obtained from the material parameters of the cylinder (E_c) and the block (E_b) as follows:

$$E^* = \frac{2E_pE_b}{E_c\,(1-\nu_b^2) + E_b\,(1-\nu_c^2)}, \tag{6.4}$$

and the combined radius, R^*, is evaluated from the radius of the cylinder, R_1, and block, R_2, in a similar way. Nevertheless, since $R_2 \to \infty$, the combined radius is reduced to the cylinder's radius,

$$R^* = \lim_{R_2\to\infty} \frac{R_1R_2}{R_1+R_2} = \lim_{R_2\to\infty} \frac{R_1}{R_1/R_2+1} = R_1. \tag{6.5}$$

In order to compare the numerical results with the analytical solution, the analysis was divided in two phases. In the first phase, a compressive point load of $F_y = 5kN$ is applied to the top of the cylinder. Under this load, only elastic strains will occur, which allows a direct comparison with the analytical solution. For the given numerical parameters, the expected analytical results are:

$$\begin{aligned} P_{\max} &= 1577.32N/mm^2 \ ; \\ a &= 2.018mm \ ; \\ P &= 1577.32\sqrt{1 - \left(\frac{x}{a}\right)^2} \ . \end{aligned}$$

In the second phase of the analysis, the point load is increased to $F_y = 12.5$kN, which leads to the appearance of plastic strain on both bodies. For this phase the analytical solution no longer holds.

6.5.2 Elastic domain

In the first phase of the case study, the applied load yields a maximal equivalent stress at $x = 0$ equal to 327MPa. This pressure is below the yield stress of both materials employed, which guarantees that no plastic strains are developed. In addition, at this point, frictional forces are negligible.

The load between the contact surfaces is well transferred and the convergence of the problem for the elastic increment, which is the first increment depicted in Table 6.6, is quadratic for both methods. The relative residual norm is below 10^{-10} in 4 iterations for the Penalty method and 3 iterations for the Dual Mortar method.

Figure 6.14: Cylinder-to-block problem - contact pressure evolution.

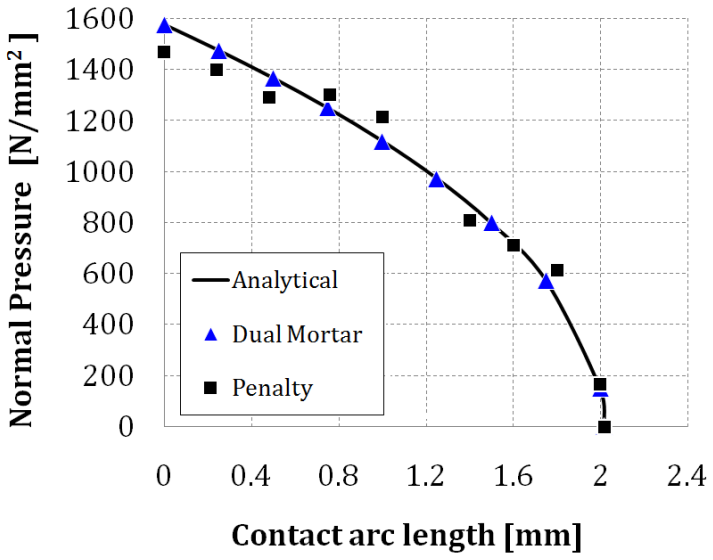

(a) Elastic domain.

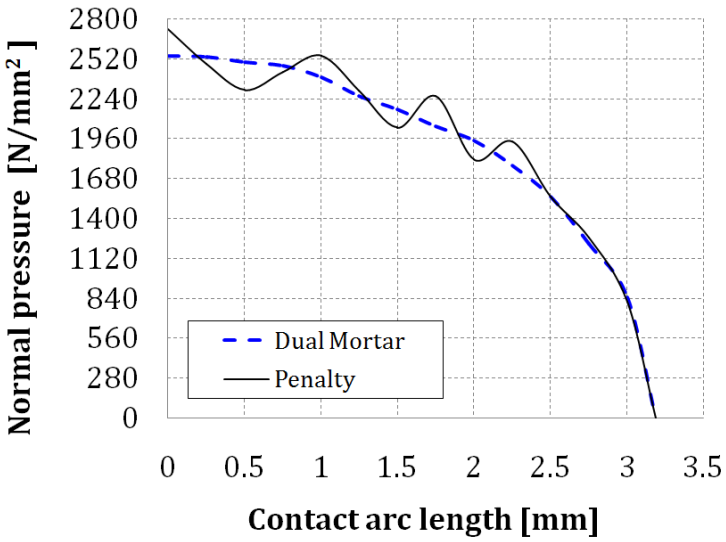

(b) Plastic domain.

A comparison between the analytical solution for the normal force with the results obtained by the numerical simulations, with both methods, is depicted in Figure 6.14(a). Despite the small differences on the normal forces, both methods have a reasonable agreement.

Table 6.6: Cylinder-to-block problem - residual norm convergence behavior.

		Penalty $\epsilon_\eta = \epsilon_\tau = 10^4$	Dual Mortar $c_\eta = c_\tau = 1$
a [mm]		3.176	3.198
t_n	$\mathbb{k}$	Relative Residual Norm (%)	
001	1	0.626481E-01	0.836091E-02
	2	0.156492E-04	0.739726E-06
	3	0.269254E-06	0.922262E-10
	4	0.198423E-10	
100	1	0.269482E-01	0.223108E-03
	2	0.589423E-04	0.198341E-07
	3	0.394568E-09	0.135704E-11
	4	0.142679E-12	
200	1	0.452691E+01	0.226485E-02
	2	0.264821E-01	0.754524E-04
	3	0.485938E-03	0.917062E-08
	4	0.337746E-06	0.896271E-12
	5	0.852251E-11	
$\sum(\mathbb{k})$		968	685

6.5.3 Plastic domain

In the second phase, under the action of a vertical force equal to $F_y = 12.5$kN, the contact surfaces develop plastic deformation. For this phase, the excessive non-physical oscillation of normal forces predicted by the NTS-Penalty method makes it no longer reliable, see Figure 6.14b. The convergence rate also decreases for the penalty method, as can be observed for increments 100 and 200 in Table 6.6. In contrast, the Dual-Mortar method preserves the spatial convergence rate regardless the presence of plastic strains. It is important to remark that the relative residual norm of the Dual Mortar method is always smaller than the penalty method, which helps the convergence. Due to the increase on the load, the number of nodes in contact also increases. This leads to the appearance of differences in the accuracy of the two methods since the Dual-Mortar method has a better distribution of loads over the contact surfaces and a relatively smoother pattern for the evolution of the normal pressure, which can be seen in Figure 6.14(b).

Table 6.7: Cylinder-to-block problem - fretting wear conditions.

Conditions	I.R. McColl (2004)	C. Paulin (2008)
Cylinder radius, R (mm)	12	10
Flat base length, L (mm)	24	20
Flat base / cylinder width, B (mm)	10	3
Indentation Force, F (N)	185	400
Displacement amplitude, $\pm\hat{u}_x$ (μm)	50	75
Number of loading cycles, n_{cyc}	18000	20000
Base material,	*Mild steel*	*Titanium*
Coefficient of friction, $\mu_{\mathcal{L}}$	0.8	0.8
Energy wear coefficient, α_w (μm$^3/J$)	660	415
Complementarity parameters, c_η, c_τ	10,10	10,10

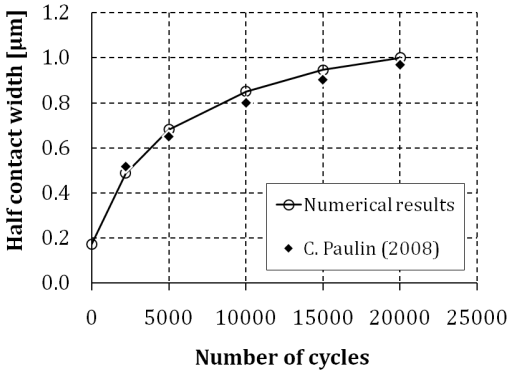

(a) Comparison with experimental data from C. Paulin et al. [58].

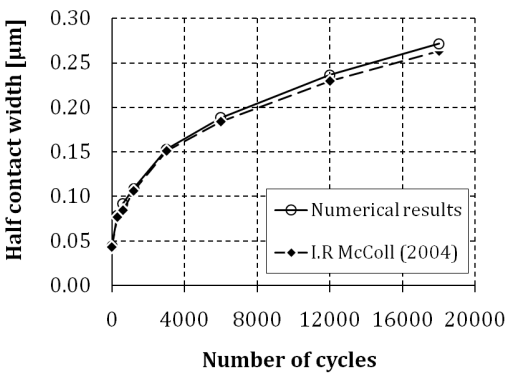

(b) Comparison with results from I.R. McColl et al. [53].

Figure 6.15: Cylinder-to-block problem - half-length of contact zone.

6.5.4 Fretting wear evaluation

Two new sets of conditions were employed to analyze the fretting wear evolution in this numerical example. They can be found in Table 6.7. These conditions were previously employed in the works of I.R. McColl et al. [53] and C. Paulin et al. [58]. Their works are also used as reference for comparison against the results obtained with the single step strategy. In this analysis, the cylinder is set to displace in it's horizontal axis after the indentation force is applied. Friction is considered in this analysis and the amplitude of the horizontal displacement is kept low in order to simulate fretting within the stick regime. In accordance with the conclusions obtained with the analysis in Section 6.2, second order dual-basis is employed in this example.

The numerical results obtained for the half-length of the contact zone are shown in Figure 6.15. They were compatible with both the experimental results provided in [58] and the numerical solution obtained by [53], which shows the accuracy of the energy wear approach employed here.

The evolution of the wear depth given by the energy method is slightly more

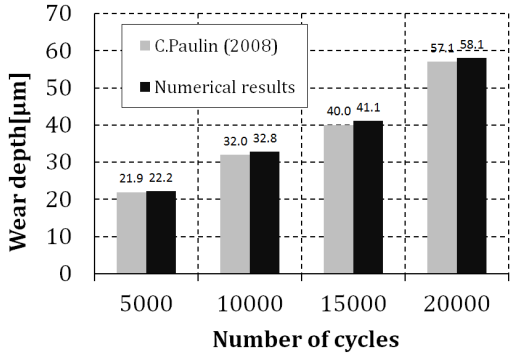

(a) Comparison with experimental data from C. Paulin et al. [58].

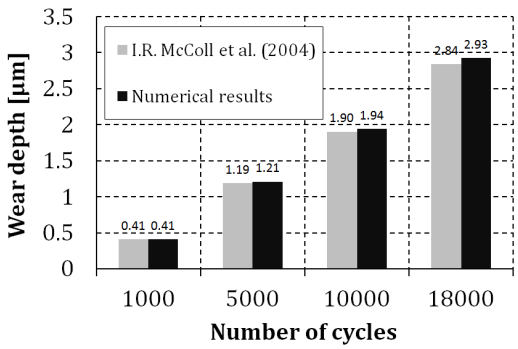

(b) Comparison with results from I.R. McColl et al. [53].

Figure 6.16: Cylinder-to-block problem - wear depth evolution.

conservative than the one obtained by the Archard method, as can be seen in Figure 6.16(b). Nevertheless, comparison between the single step strategy and the experimental data from [58], Figure 6.16(a), shows a good agreement. The convergence rates of the residual forces was kept fairly similar to the one shown in Table 6.6: an average of 4 iterations per increment.

6.6 Ironing problem

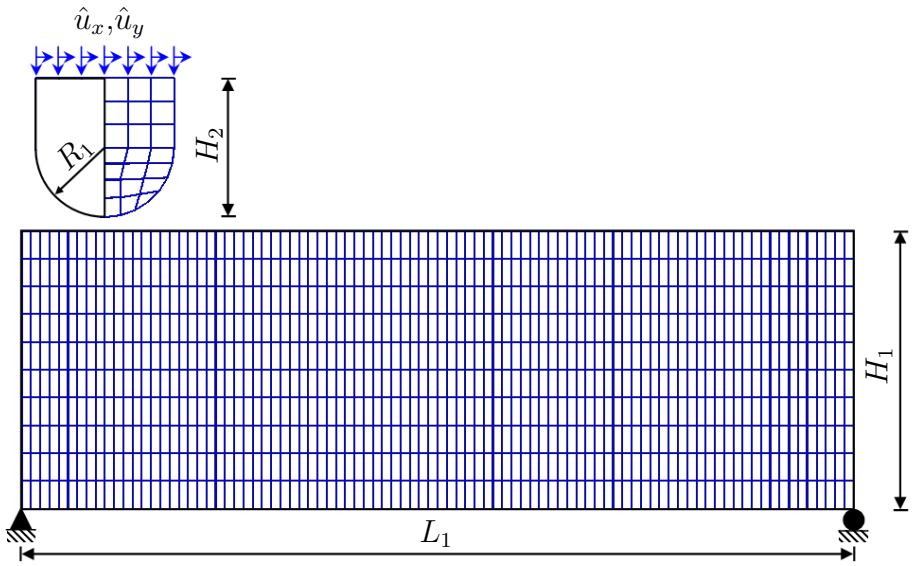

Figure 6.17: Ironing problem - geometry and FE discretization.

The so-called Ironing problem [22,33] is a variation of the cylinder-to-block Hertizian contact problem, where after the indentation stage the tool is set to slide over the block. This combination of displacements generates high levels of deformation. The geometry, the finite element discretization and the loads of this problem are depicted in Figure 6.17. The dimensions of the tool and the base are: $L_1 = 12$mm, $H_1 = 4$mm, $H_2 = 2$mm and $R_1 = 1$mm.

The simulation is divided in two stages. In the first stage, the semi-circular tool, already in contact with the base, is vertically pushed against the base $\hat{u}_y = 0.3$mm. This stage is set to take 30 increments. During the second stage, the tool is horizontally displaced by $\hat{u}_x = 9.6$mm. This load is equally divided into 400 increments. For this simulation, the values chosen for the penalty multipliers were $\epsilon_\eta = \epsilon_\tau = 10^9$ and for the complementarity parameters $c_\eta = c_\tau = 10^{-1}$. A static coefficient of friction equal to $\mu_{\mathcal{Q}} = 0.4$ and a kinetic coefficient of friction of $\mu_{\mathcal{L}} = 0.3$ are considered. The materials chosen for the tool and the block were, respectively, the *Tungsten alloy* and the *Aluminum alloy* (Table 6.1).

6.6.1 Evolution of the effective plastic strain

During the simulation, a layer of plastic deformation develops along the contact surface and the active set changes more than once for most increments. This happens due to the fact that once a given node at the left side of the contact surface reaches the yield stress it no longer recovers from the deformation, leading to it's deactivation. However, at the right side, material is being accumulated and new contact nodes become active. This constant change of the contact surface length

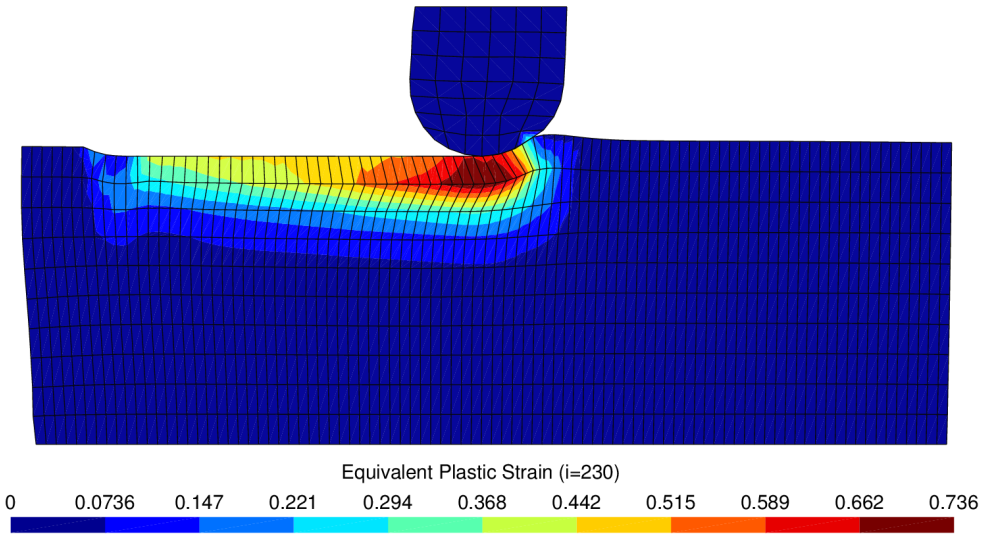

Figure 6.18: Ironing problem - effective plastic strain at $d_x = 4.8$mm and $d_y = 0.3$mm.

and the number of contact nodes during a single increment poses additional challenges to the performance of the solution algorithms, as shown in Table 6.8. The accumulated material on the right hand side also produces a high tangential load on the tool, which leads to it's distortion and plastic deformation. Figure 6.18 and Figure 6.19 show the effective strain at steps 230 and 430, respectively. Reducing the load of each increment helps to mitigate this phenomena, however as soon the material reaches the plastic domain even small loads incur in large distortions of the finite element mesh and consequently changes on the contact pairs occur.

6.6.2 Performance analysis

The convergence evolution of the relative residual norm is listed in Table 6.8, for three representative steps and for three solution strategies: the Penalty method, the nested iterative strategy described in Table 5.2 and single iterative strategy described in Table 5.1. From Table 6.8, it is possible to see that Penalty method is able to solve the problem when employing high values for the penalty multipliers ($\epsilon_\eta = \epsilon_\tau = 10^9$). Nevertheless, the convergence rate of the NTS method is poor when compared with the primal-dual active set strategies. Furthermore, the level of penetration becomes erratic during the solution and it is difficult to know in advance whether a given set of penalty multipliers will lead to the solution of the problem or not. The convergence evolution provided by the PDASS algorithms were similar. This happens due to the very small size of the increments. Therefore, in order to enable a more detailed comparison between those methods, the number of increments is reduced by half and each increment is raised to twice their initial size (i.e., phase I: 15 increments with $\Delta\hat{u}_y = 0.02$mm; phase II: 200 increments with $\Delta\hat{u}_x = 0.096$mm).

Table 6.8: Ironing problem - residual norm convergence behavior.

		Penalty $\epsilon_\eta = \epsilon_\tau = 10^9$	Single step $c_\eta = c_\tau = 10^{-1}$	Nested step
t_n	$\mathbb{k}$	Relative Residual Norm (%)		
030	1	0.285466E+02	0.772309E+01	0.772308E+01
	2	0.125468E+00	0.392728E+00	0.392728E+00
	3	0.861073E-01	0.337489E-03	0.337488E-03
	4	0.973016E-02	0.229909E-09	0.229908E-09
	5	0.744196E-03	0.111215E-11	0.111214E-11
	6	0.726018E-04	-	-
	7	0.186181E-09	-	-
230	1	0.626103E+01	0.280271E+01(*)	0.280271E+01
	2	0.124845E+00	0.158554E+01	0.220156E+01
	3	0.920084E-01	0.436638E-01	0.112644E+00
	4	0.108697E-02	0.125687E-02	0.612545E-02
	5	0.783435E-03	0.274675E-04	0.266750E-04
	6	0.226584E-06	0.246126E-10	0.422109E-07
	7	0.141980E-09	-	0.199088E-11
430	1	0.958624E+02	0.706285E+03(*)	0.706285E+03
	2	0.111254E+01	0.256844E+02(*)	0.298211E+01
	3	0.128455E+00	0.862577E+01	0.116925E-01
	4	0.547556E-01	0.150099E+00	0.138852E-02
	5	0.343761E-02	0.546990E-01	0.623577E-04
	6	0.517235E-03	0.734911E-04	0.421596E-07
	7	0.436580E-04	0.149939E-09	0.336952E-09(+1)
	8	0.140885E-06	-	-
	9	0.269842E-09	-	-
$\sum(\mathbb{k})$		3452	2600	3258(**)

(*) Change in active set.

(+1) Check of active contact set failed, Newton cycle has to be repeated.

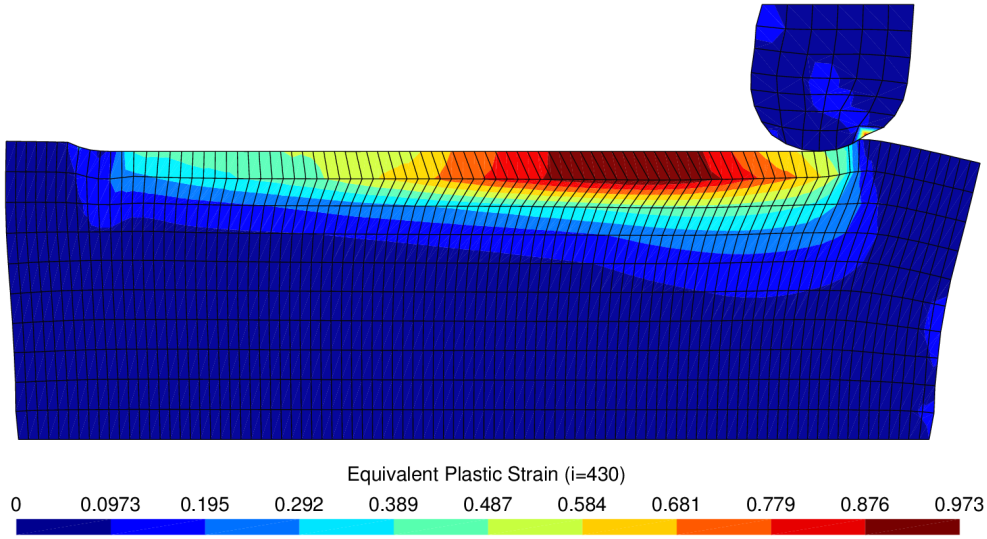

Figure 6.19: Ironing problem - effective plastic strain at $d_x = 9.6$mm and $d_y = 0.3$mm.

Table 6.9 shows the convergence results provided by this new set of loading conditions. It is possible to observe that due to the increase of the load increment, the convergence rate of both strategies is deteriorated. In particular, at the plastic regime the nested strategy becomes more costly since the changes of active set require new Newton cycles to be performed. On the other hand, the single step strategy also reveals a disadvantage: at the plastic regime, the contact pair changes more frequently during a single increment than that at the elastic regime. Therefore, due to sensitivity of this approach to changes of the active set, it's convergence rate is severely deteriorated. Furthermore, depending on geometry discretization and increment loading size the constant changes of active set may prevent to find a solution to the problem without significantly reducing the load increment.

6.6.3 Reaction forces

Figure 6.20 displays the behavior of the total reactions over the top surface of the tool obtained with the Penalty method and the single step scheme. Forces increase during the indentation phase and stay relatively constant while the tool is sliding. However, a small oscillation of the horizontal force is expected since the amount of material accumulated at the right hand side of the tool changes over the simulation. Both methods yield similar results for the vertical reactions. However the horizontal reactions provided by the Penalty method became erratic at the last quarter of the simulation, when the highest levels of shear are attained.

6.6.4 Fretting wear evaluation

Since in this problem there is a combination of an indentation and finite slip process, by repeating these two phases in a cyclical way, the fretting wear phenomena can be

Table 6.9: Ironing problem - comparison of PDASS algorithms.

		Nested step	Single step $c_\eta = c_\tau = 10^{-1}$
t_n	$\mathbb{k}$	Relative Residual Norm (%)	
015	1	0.46320E+02	0.39452E+02
	2	0.21169E+01	0.62015E+00
	3	0.10101E+00	0.30008E-02
	4	0.36045E-02	0.19961E-04
	5	0.18604E-04	0.85600E-09
	6	0.45969E-06	0.79367E-11
	7	0.20781E-11	-
115	1	0.10007E+03	0.20508E+02
	2	0.49089E+02	0.95486E+01(*)
	3	0.19065E+01	0.89068E+01(*)
	4	0.56002E+01	0.78886E+01
	5	0.27951E-02	0.30219E+00
	6	0.13355E-04	0.11298E-01
	7	0.80743E-08	0.52594E-04
	8	0.31092E-11	0.61413E-06
	9	-	0.46302E-09
215	1	0.96452E+02	0.99564E+02(*)
	2	0.38491E+01	0.49261E+02(*)
	3	0.16482E+00	0.22279E+01(*)
	4	0.79050E-01	0.31859E-00
	5	0.31105E-02	0.13692E-01
	6	0.15924E-04	0.39562E-02
	7	0.36294E-06	0.92615E-04
	8	0.14820E-08	0.41105E-06
	9	0.46594E-10(+1)	0.26941E-08
	10	-	0.12943E-11
$\sum(\mathbb{k})$		1908	1819

(*) Change in active set.
(+1) Check of active contact set failed,
Newton cycle has to be repeated.

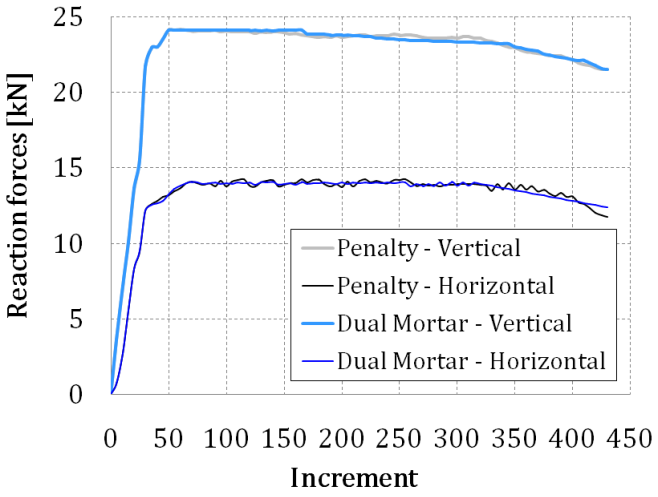

Figure 6.20: Ironing problem - Reaction forces

simulated. A more refined mesh is employed in this analysis. A total of 150 4-noded quadrilateral F-bar elements are used for the discretization of the tool, while the base is discretized with 1600 elements. The loads $\hat{u}_x$ and $\hat{u}_y$ at the top surface of the tool are applied within four stages. The vertical displacement, $\hat{u}_y = -0.04$mm, is applied at both the first stage and the third stage. The horizontal displacement, $\hat{u}_x = 9.6$mm, is applied in stage 2 towards the x-direction while in stage 4 the tool is brought back to the origin. Stages 1 and 3 are equally divided into 25 increments, stages 2 and 4 have 100 increments each. Next, these four stages are regarded as one cycle, which is repeated 100 times. Both solids are set to worn in this example. The material chosen for the tool and the base and the respective energy wear coefficient, α_w, are: *Titanium*, $415 \cdot 10^{-6} mm^3/J$ and *Aluminum alloy*, $840 \cdot 10^{-6} mm^3/J$. The complementarity parameters were set to $c_\eta = c_\tau = 10$. The wear depth is balanced among the first 5 upper FE layers of the base surface and 3 lower FE of the tool.

In Figure 6.21, the plot of the friction force versus the sliding displacement for 4 number of cycles (i.e. sample of the fretting map) is shown. At the 5th cycle both the friction force and the energy dissipated over per cycle are relatively small. The frictional force increases in a linear way until the 50th cycle, when it stabilizes. At this point the finite elements of the base are on the plastic regime of deformation and therefore the increment of force required to further deform the structure becomes much smaller. Figure 6.22 displays the stress distribution at final configuration. The levels of strain together with the wear depth create a large scar. In fact, during the last 20 cycles the size of the scar becomes deep enough to create small jumps on the friction force. This happens because the side of the tool starts to hit the corners of the scar, which leads to sudden increases of the tangential reaction that creates sharp peeks at the end of the cycles (see Figure 6.21). This effect is commonly seen in fretting experiments and does not provide any significant influence in the results.

The initial residual force changed several times during the simulation. This

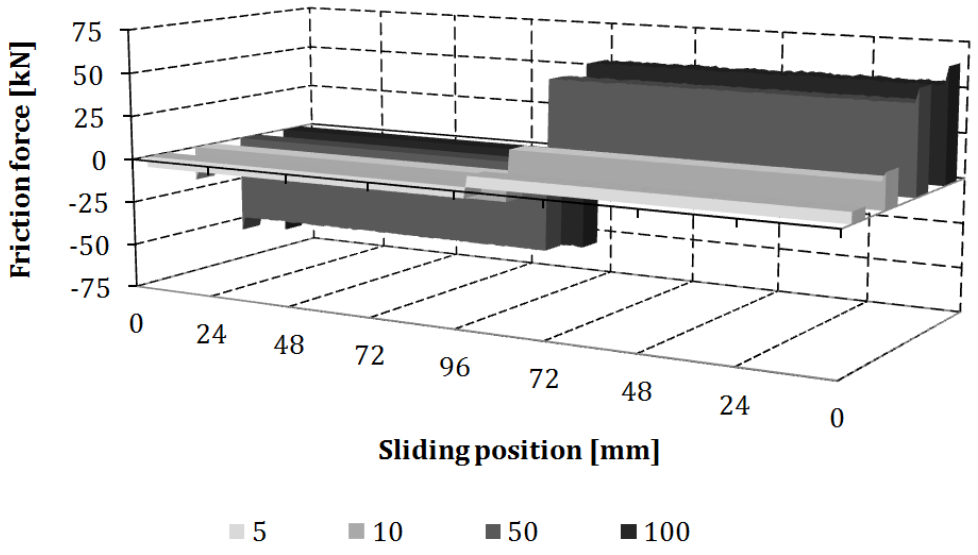

Figure 6.21: Ironing problem - Fretting map samples.

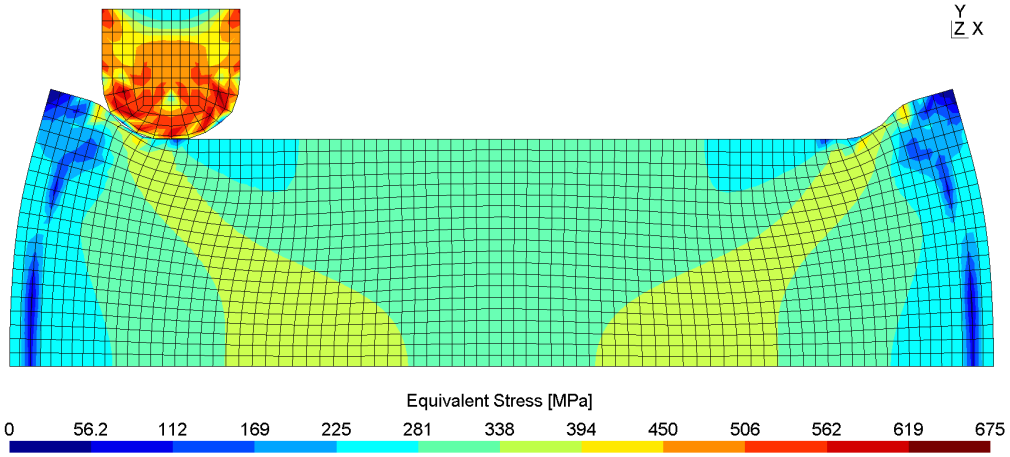

Figure 6.22: Ironing problem - stress distribution at $n_{cyc} = 100$, $\mathbb{k} = 250$.

Table 6.10: Ironing problem - residual norm convergence behavior.

t_n	$n_{cyc} = 1$, $\Bbbk = 1$	$n_{cyc} = 5$, $\Bbbk = 125$	$n_{cyc} = 10$, $\Bbbk = 250$	$n_{cyc} = 50$, $\Bbbk = 125$	$n_{cyc} = 100$, $\Bbbk = 1$
1	110.136	11.9434	99.5383	1.44039	12.8832
2	20.1235	1.05039	20.0256	0.679160E-02	1.93006
3	5.69351	0.8788E-01	3.75213	0.772553E-03	0.110024E-01
4	0.395176	0.1929E-04	0.372059	0.697208E-08	0.705730E-06
5	0.2914E-01	0.8626E-10	0.3966E-01	0.144469E-12	0.802187E-10
6	0.1067E-04	-	0.3044E-04	-	-
7	0.8972E-10	-	0.1046E-09	-	-

happened mostly due to the growth of the contact surface and to the change of deformation regime. Nevertheless, quadratic rate of convergence is achieved within 6-7 pseudo-times steps as seen in the increments shown in Table 6.10.

6.7 Round pin to flat problem

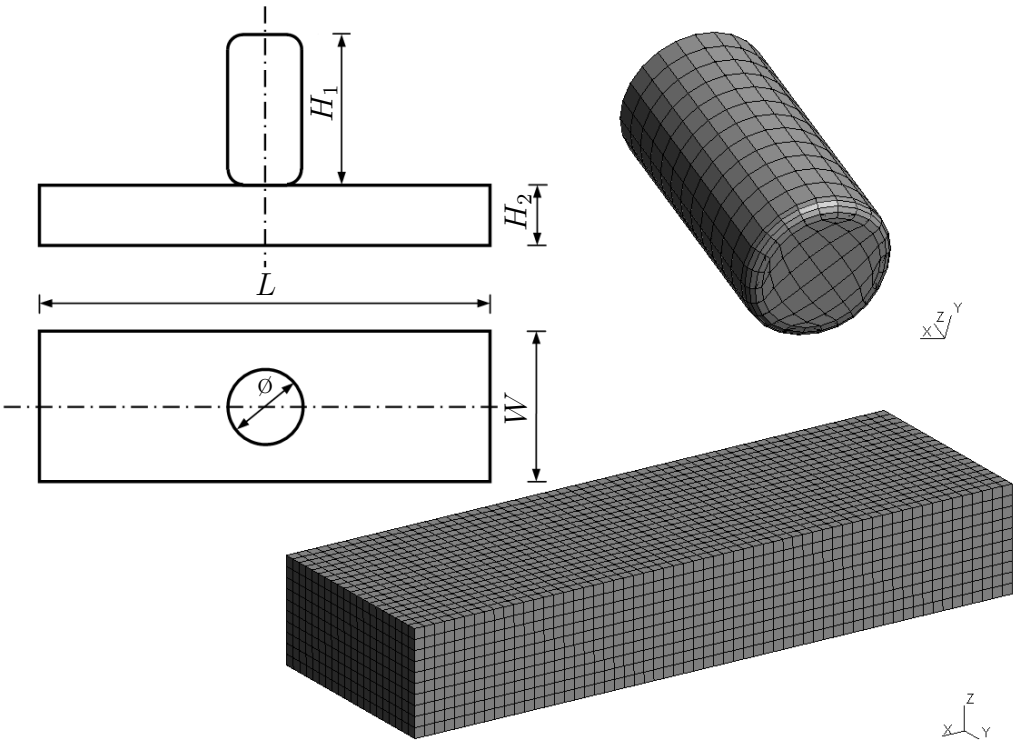

Figure 6.23: Round pin to flat problem - geometry and FE discretization.

This examples presents a benchmark often used to approximate practical problems that involve several contact phenomena, such as turbine blades, drilling screws and tyres. Here, the main goal is to compare the two active set strategies presented in Chapter 5 with experimental results in order to access their accuracy. It features a Rounded pin and flat surface, see Figure 6.23. Dimensions chosen for this analysis are: ø=5mm, $H_1 = 10$mm, $H_2 = 5$mm, $W = 10$mm and $L = 30$mm. A total of

576 linear hexahedral F-bar elements were employed for the discretization of the pin while the base contains 12000 elements.

In the first stage, the round pin is pressed against the flat surface. The applied normal pressure is $p_n = 1.3$MPa. Next, the rounded pin is set to describe a reciprocating motion leading to the development of fretting fatigue and material loss. In this example, the amplitude of the reciprocating movement applied to the pin is equal to $\delta_{\pm} = \pm 10$mm, representing one loading cycle. A total number of cycles of $n_{cyc} = 18,000$ were conducted. Each stage is divided into 25 equal incremental displacements of 0.4mm. Therefore, the number of increments per cycle is equal to 50 and the total number of increments is equal to 900,000. The materials employed for the pin and the flat surface are *Hard steel* and hydrogenated nitrile *elastomer*, respectively. The elastomer is a very resilient material when employed in a lubricated environment. However, under the assumption of dry friction ($\mu = 0.8$) it's wear coefficient is extremely high, $\alpha_w = 15 \cdot 10^{-3} mm^3$.

Since the flat surface material is highly elastic and the applied pressure is small, the presence of plastic strains in this example is minor. Therefore, the great majority of the nodal displacements at the contact interface is due to the fretting wear topography update. The displacement field for the final configuration of the flat surface is given by Figure 6.24.

Both length and depth of scar have a good agreement with the experimental results. For a qualitative comparison, the scar profile of the experimental specimen is shown in Figure 6.25.

Wear rates have a moderate increase during the simulation. The results obtained, with both nested and single step methods, have a very good agreement with experimental data. The total volume lost over the simulation was equal to $135.86 mm^3$, only 2.5% less than the experimental value of $139.27 mm^3$. This suggests that in the lack of significant levels of plastic strain both methods can reproduce the fretting phenomena accurately. The comparison between the numerical simulation results for the wear depth and it's experimental data counterpart is presented in Figure 6.26.

Since the contact area remains fairly constant during the simulation, the contact pairs and the active set are also kept the same throughout the incremental solution. In this particular situation, both methods show a quadratic convergence rate to a residual force as low as E-12, as displayed in Table 6.11.

6.8 Round pin to disc problem

This problem is basically a variation of the previous example, where instead of a reciprocating motion, the round pin prescribes a circular movement over a disc. This configuration is often used to study brake systems and other sliding mechanisms. The problem's geometry and mesh discretization are given in Figure 6.27. The dimensions of the round pin and the disc are: ø=600mm, L=300mm, $H_1 = 150$mm, $H_2 = 60$mm, and $R = 100$mm.

The total number of finite elements used for the discretization of the pin and the flat surface is equal to 576 and 10125 linear F-bar hexahedral elements, respectively. The materials chosen for the round pin and disc were, *Hard steel* and *aluminium*

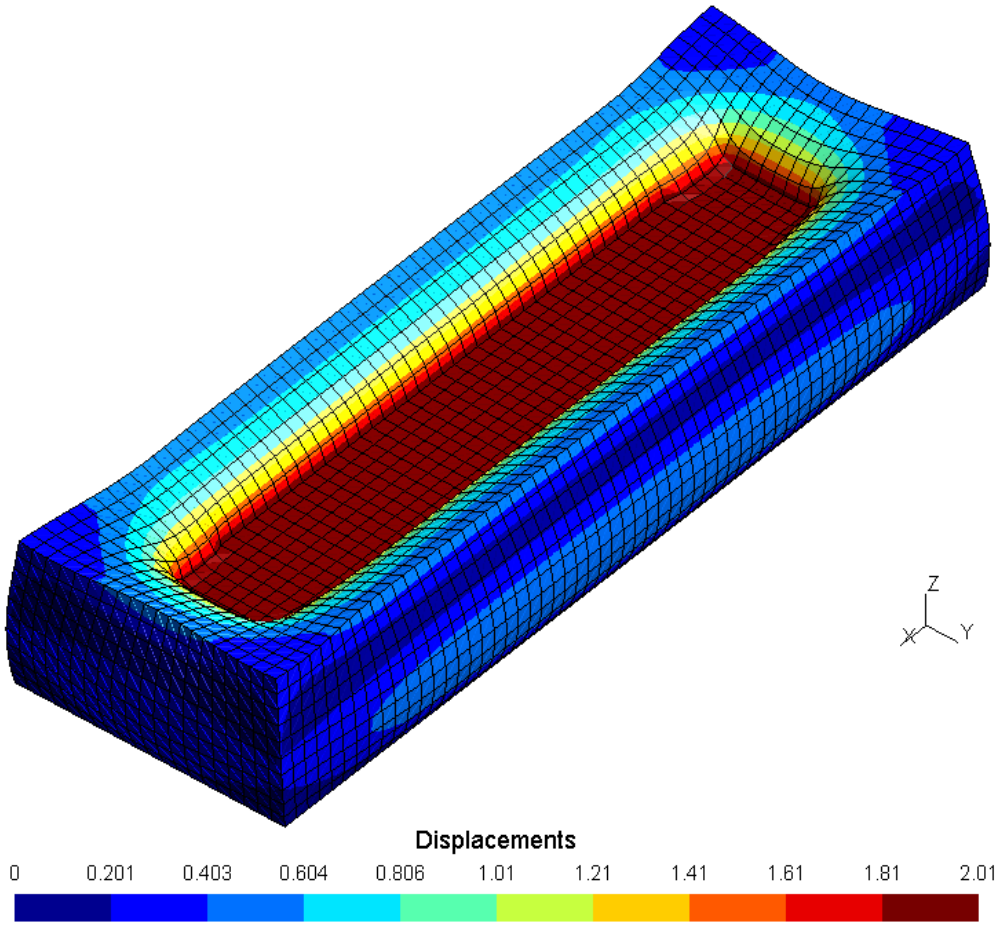

Figure 6.24: Round pin to flat problem - final configuration.

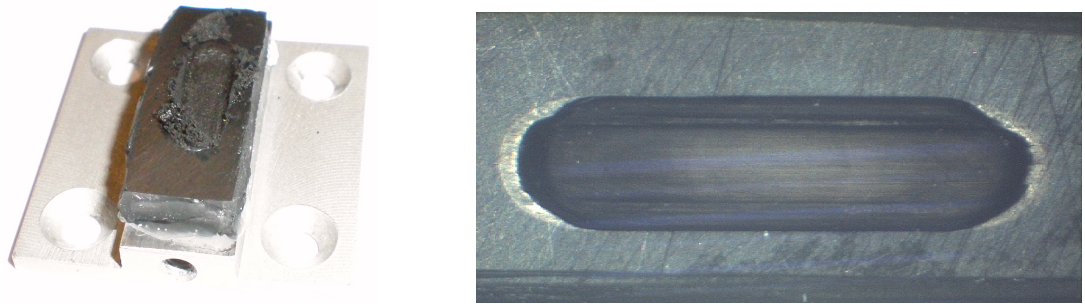

(a) Specimen with debris. (b) Clean specimen.

Figure 6.25: Round pin to flat problem - elastomer specimen after testing.

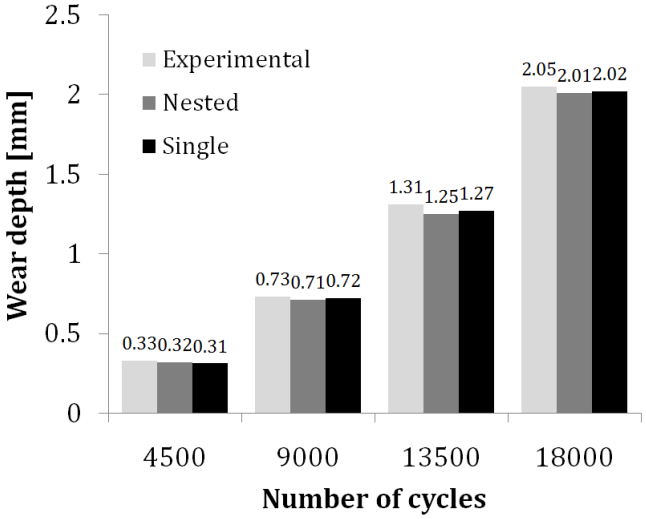

Figure 6.26: Round pin to flat problem - wear depth.

Table 6.11: Round pin to flat problem - residual norm convergence behavior.

		Nested step	Single step
$1000t_n$	$\mathbb{k}$	Relative Residual Norm (%)	
300	1	1.31E+01	1.91E+00
	2	1.02E+00	7.19E-03
	3	8.56E-03	1.27E-07
	4	1.33E-06	5.10E-13
	5	4.68E-13	-
600	1	2.52E+01	1.44E+00
	2	1.10E+00	5.82E-03
	3	1.20E-02	1.11E-07
	4	4.44E-06	4.78E-13
	5	1.03E-12	-
900	1	2.81E+01	1.17E+00
	2	1.14E+00	5.51E-03
	3	1.20E-02	1.02E-07
	4	4.44E-06	4.38E-13
	5	1.03E-12	-
$\sum(\mathbb{k})$		4,352,113	4,012,745

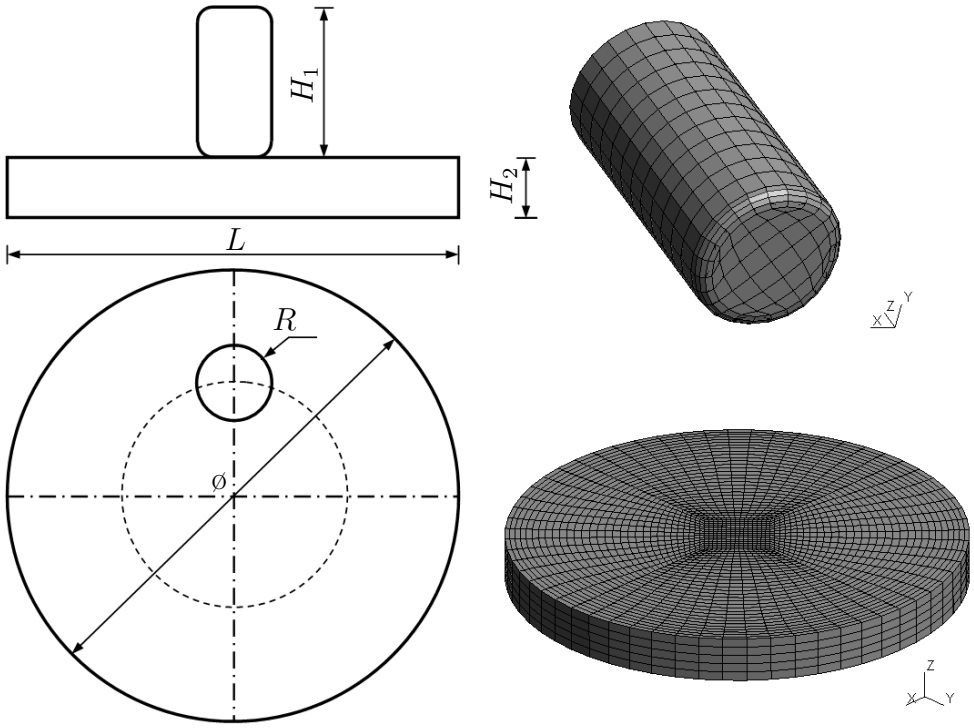

Figure 6.27: Round to disc problem - geometry and FE discretization.

alloy, respectively. The coefficient of friction assumed for the surfaces is equal to $\mu = 0.7$ and the energy wear coefficient, α_w, for the disc is equal to $840 \cdot 10^{-6} mm^3/J$.

In the first stage, a normal pressure $p_n = 600$MPa is applied to the top of the rounded pin within 20 equal pseudo-time steps. In the second stage, a radial displacement is prescribed the rounded pin such that it completes a circular path over the disc (one loading cycle). This loading stage is applied within 72 increments of 5 degrees each. Moreover, to reproduce the fretting wear phenomena, the second loading stage is repeated 20,000 times.

Different from the first example, the continuous nature of the circumferential cyclical motion gives to this problem a smoother behavior for the tangential forces. The average value for the friction force over the contact zone is 7.53kN and it remains fairly constant during the second stage of the numerical simulation. However, since the disc is made from a metallic material, the strains have a much more important role in this example. The pressure applied over the pin, $p_n = 600$MPa, develops plastic strains over the contact zone. At the end of the first stage, the total indentation displacement imposed to the disc is equal do 6.7mm (almost 12% of it's initial height). During the second stage, a total volume of $68325 mm^3$ of the disc is removed from it's surface (representing 2% of it's initial volume). At the end of the simulation the wear scar has a total depth of 9.8mm, from which 2.9mm are related to the material removal (i.e. wear depth). The final configuration of the disc, obtained with the fully implicit scheme, is depicted at Figure 6.28.

Comparing the obtained results for the wear depth – with the two schemes- - over the loading cycles, it is possible to observe that during the simulation the values

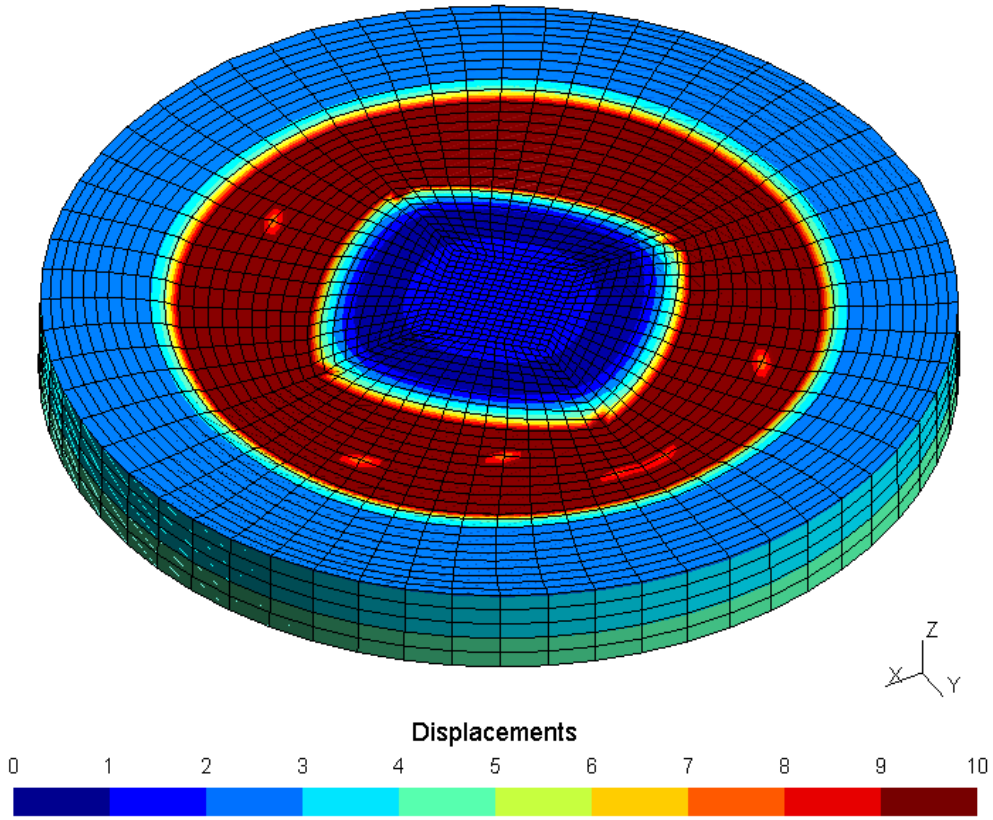

Figure 6.28: Round pin to disc problem - final configuration.

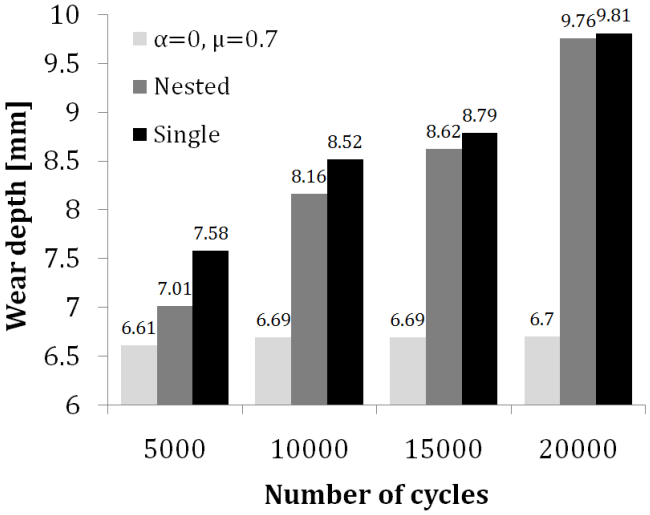

Figure 6.29: Round pin to disc problem - wear depth evolution.

provided by the Nested method are not as accurate. This happens due to the fact that the wear evaluation is done apart from the contact constraints, which leads to a non synchronized output, as can be observed in Figure 6.29. However, as the simulation continues, both methods converge to a close result.

The inelastic strains have a great impact on the convergence rates of the residual force in this example, especially those obtained with the Nested scheme. From Table 6.12 it is possible to conclude that as the simulation progresses, the required number of iterations for minimizing the residual force increases for the nested scheme. While the single step strategy maintain an average of 5-6 iterations per increment. Moreover, the total number of increments required by the nested scheme is over 16% higher when compared to the single step scheme. Nevertheless, due to the small size of the increments employed in this example, both methods shows a stable behavior. This is because there were very few active set changes on the single step scheme and there was no repetition of the Newton step on the nested scheme.

6.9 Sphere in contact with a half hollow sphere

This last numerical example presents a sphere being fretted against a hollow half-sphere base. The goal is to verify the reliability and performance of the solution schemes when dealing with highly curved surfaces. The problem geometry and respective mesh discretization are presented in Figure 6.30. For better visualization, only one-quarter of the hollow sphere is depicted.

The diameter of the sphere is ø=20mm while the outer radius of the half hollow sphere is $R = 20$mm. A fillet of $\theta = 5$ degrees is made to the top of the hollow sphere. This was done to avoid stability issues (due to the constant change on the active set) that would occur if the last nodes at the far end of the inner surface were considered as contact candidates. A total of 2048 linear hexahedral F-bar elements were employed for the discretization of the sphere while the base contains 2000

Table 6.12: Round pin to disc problem - residual norm convergence behavior.

	Nested step scheme			
$\frac{n_{cyc}}{\mathbb{k}}$	5000	10000	15000	20000
1	2.576E+2	1.676E+2	0.632E+2	1.919E+3
2	1.135E+1	0.891E+1	0.132E+1	0.344E+2
3	0.371E+0	0.569E+0	0.959E+0	0.649E+1
4	1.478E-2	0.312E-1	0.402E-1	0.102E+0
5	1.125E-4	2.090E-2	0.908E-2	0.266E-1
6	0.429E-9	0.235E-4	1.985E-4	0.701E-3
7	0.601E-12	0.103E-8	0.782E-7	0.823E-5
8	-	0.235E-12	0.755E-9	0.409E-8
9	-	-	0.302E-11	0.871E-10
10	-	-	0.166E-13	0.218E-12
$\sum(\mathbb{k})$	15,065,643			

	Single step scheme			
$\frac{n_{cyc}}{\mathbb{k}}$	5000	10000	15000	20000
1	0.581E+3	1.097E+2	0.313E+2	2.777E+3
2	0.707E+1	0.702E+1	0.109E+1	1.649E+1
3	0.815E-1	0.989E-1	0.321E+0	0.962E+0
4	0.871E-4	0.882E-2	1.091E-2	0.331E-2
5	1.541E-8	1.529E-4	0.525E-4	0.884E-5
6	0.312E-12	0.735E-7	0.656E-8	0.529E-8
7	-	0.303E-11	0.707E-12	0.902E-12
$\sum(\mathbb{k})$	12,976,081			

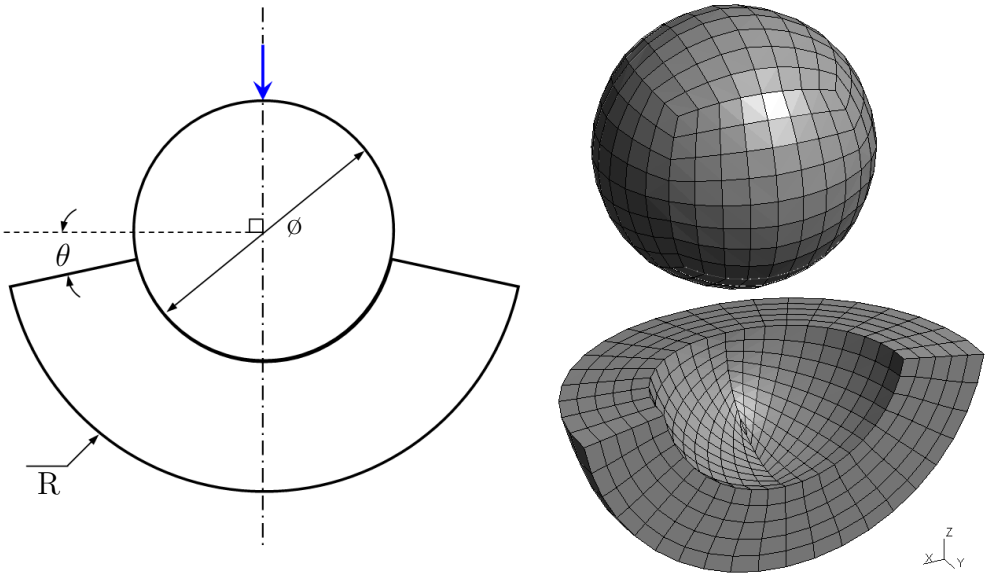

Figure 6.30: Sphere in contact with a half hollow sphere - geometry and FE discretization.

elements. A vertical force $F_y = 10\text{kN}$ is applied to the top of the sphere and the bottom of the base (outer radius surface) is fully constrained. The circular motion prescribed to the sphere is applied in 36 increments of $\frac{\pi}{18}$ radians and repeated in a total number of revolutions $n_{cyc} = 1000$.

In Figure 6.31 the history of the contact surface topography, obtained with the single step strategy, is shown. During the course of the fretting process, a wear depth of 0.48mm is reached. This value represents 2.45% of the sphere's initial radius. In Figure 6.32, it is observed a significant difference in the wear depth results at the initial stages of the loading process. Although at the end of the simulation both methods present a fairly similar result, the single step scheme shows both better performance and accuracy, as seen in Table 6.13. The nested step strategy undergoes multiple Newton steps re-calculations and the absence of a fully linearized set constraints yield an slower solution of such a highly nonlinear problem.

In a final note, although the cost of the presented frameworks is much higher than the standard solutions. The examples shown in this chapter demonstrated that even in such an overwhelming set of conditions, such as the one presented in this last example, both frameworks still show a good satisfying performance. Furthermore, there is a large number of improvements to be made. They are addressed in the following chapter.

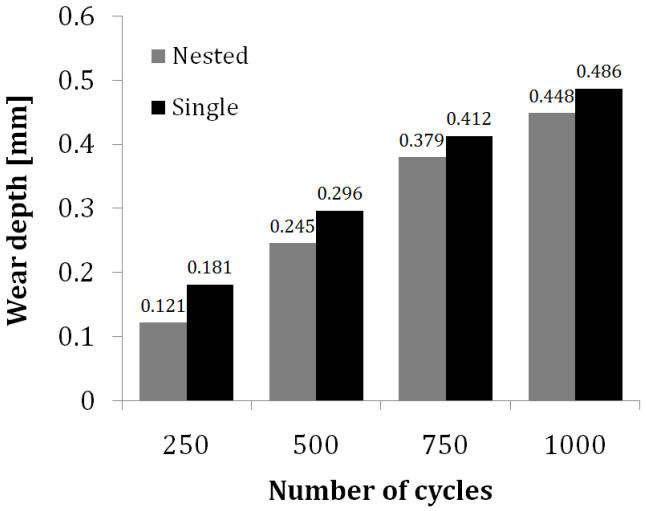

Figure 6.31: Sphere in contact with a half hollow sphere - Topography evolution for the single step scheme.

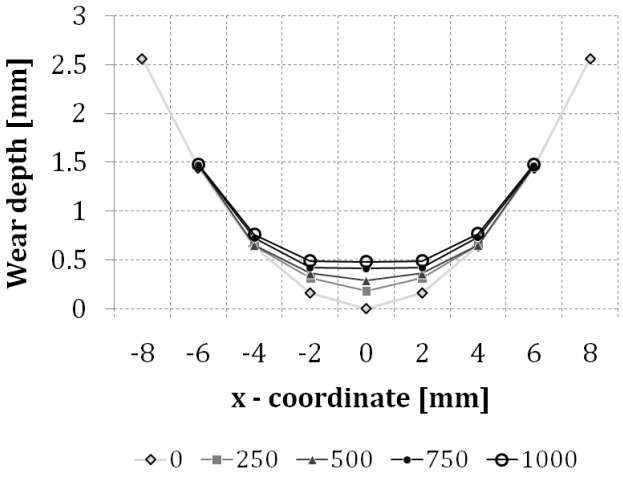

Figure 6.32: Comparison of the wear depth progression.

Table 6.13: Sphere in contact with a half hollow sphere - residual norm convergence behavior.

	Nested step scheme			
$\frac{n_{cyc}}{\mathbb{k}}$	250	500	750	1000
1	1.091E+4	2.187E+5	1.567E+5	1.423E+5
2	1.923E+3	1.089E+3	0.983E+4	0.719E+5(*)
3	0.675E+2	1.012E+2	0.429E+3	0.492E+3
4	0.303E+1	0.875E+1	0.221E+2(*)	0.301E+2
5	0.341E+0	0.341E+0	0.145E+0	0.167E+2(*)
6	0.989E-1	0.177E-1	0.761E-1	0.559E+2
7	0.385E-3	0.898E-2	0.306E-3	0.328E-2
8	0.267E-5	0.309E-4	0.166E-6	0.781E-4
9	0.521E-9	0.183E-7	0.842E-8	0.895E-7
10	0.401E-12	0.923E-10	0.384E-9	0.386E-10
11	-	1.213E-13	0.387E-11	0.791E-12
12	-	-	-	0.671E-13(+1)
$\sum(\mathbb{k})$	411,368			

	Single step scheme			
$\frac{n_{cyc}}{\mathbb{k}}$	250	500	750	1000
1	0.921E+3	1.625E+3	1.230E+4(*)	1.581E+4(*)
2	0.368E+2	0.891E+2	0.873E+4(*)	2.049E+4(*)
3	0.287E+1	0.454E+1	0.499E+3	1.091E+2
4	0.155E+0	0.258E+0	0.303E+2	0.937E+0
5	0.703E-1	0.962E-2	0.582E+0	0.382E-2
6	0.358E-2	0.421E-4	0.845E-2	0.274E-4
7	0.167E-4	0.304E-9	0.926E-4	0.561E-8
8	0.592E-8	0.991E-12	0.267E-8(+1)	0.628E-11
9	0.304E-12	-	-	0.729E-13
$\sum(\mathbb{k})$	338,952			

(*) Change in active set.
(+1) Check of active contact set failed, Newton cycle has to be repeated.

Chapter 7

Final remarks

7.1 Summary

This thesis is devoted to the formulation and analysis of robust numerical algorithms for the solution of multibody frictional contact problems, which include fretting wear and finite strains with inelastic material behavior. Therefore, two numerical frameworks are presented that cover the modeling of finite inelastic deformation, the numerical threatment of frictional contact conditions and the modeling of fretting wear phenomena. Several well-established and new models are employed for each of these building blocks, in order to capture the distinct features of the deformation behavior. In this regard, a new method for the numerical evaluation of the dissipated energy and the material volume lost due to the fretting wear phenomena is introduced. Furthermore, different schemes for performing the geometrical update of the contact surface topography are presented. A multi-directional function able to guide the evolution of the scar profile is another novelty described in this work.

Additionally, many aspects of the latest contact constraints enforcement formulations are discussed in detail. An extensive study of the performance of the Mortar method with dual-basis for the lagrangian multipliers, in the finite strain context, has been presented.

A wide range of numerical examples has been included for better comprehension of the solution procedures and to demonstrate the performance of the proposed algorithms.

7.2 Conclusions

The most important conclusions can be summarized as follows:

- The results obtained with the Dual-Mortar method emphasized the benefits of using this formulation in contact problems involving inelastic material behavior. The superior correlation between the contacting surfaces provided by the mortar segmentation promotes a smaller initial value for the residual forces, which leads to a faster solution in every increment. On the other hand, the

NTS-Penalty method was not able to fulfill the contact conditions in either an accurate or stable manner.

- In the context of accurate enforcement of contact constraints and computation of the contact pressure, it was observed that the dual basis plays a significant role. This is true for both small and finite strains.

- The complementarity parameters employed in the definition of the nonlinear complementarity functions do not affect the accuracy of the solution as occurs with the penalty multipliers in the NTS formulation. Nevertheless, the selection of complementarity parameters has a significant impact in the efficiency of the solution whether the material behavior is within the elastic or plastic domains. Due to the (possibly) strongly nonlinear nature of problem, the optimal convergence rate is only preserved when relatively low values for the complementarity parameters are used, particularly in the plastic domain, and small incremental steps are prescribed.

- Two primal-dual active set strategies (PDASS) have been discussed and applied for the solution of the class of problems addressed. Results obtained for the simulation of contact benchmarks, comparison with experimental data and other wear formulations were very satisfying. While, within the plastic domain, the single step strategy was generally more efficient than the nested iterative scheme, the robustness of the latter was usually greater than the former. However, the nested scheme struggles to deliver accurate results throughout the simulation. In particular, at the first stages of the solution process. Nevertheless, the final results obtained with this method are in relative good agreement with those obtained by the single step strategy. In summary, the nested scheme is recommended for problems with constant change of the contact pairs/active set. On the other hand, the single step strategy is suggested when dealing with complex geometries and high levels of finite strain and/or when precise computation of the Fretting wear effects, at each pseudo-time step, is demanded.

7.3 Outlook

A significant progress has been achieved in the field of fretting wear simulation with the developed framework. Nonetheless, many aspects require further examination. An investigation of the complementarity parameters influence, in problems in a finite strain regime and/or fretting wear condition, is required. Since there are indications that these parameters could be affect by the levels of strain to which the solids bodies are submitted. An adaptive strategy to compute the ideal complementarity parameters during the analysis, while considering the magnitudes of the mechanical properties of the solids in question, is currently under research.

For enhancing the evaluation of fretting wear effects, additional multi-directional friction functions should be explored. Moreover, in order to include adhesion effects,

anisotropic friction and a non-constant friction coefficient, the whole Coulomb friction concept should be re-examined. This would shed additional light on the stability issues that emerge in the frictional and in the highly curved three-dimensional numerical examples.

In order to accommodate large-scale finite element meshes and problems where the contact surface evolves in a completely unpredictable way during the simulation, the topography update scheme must be improved. For instance, an extension of the existing method, for treatment of problems where the contact zone might change in different parts of the structure or with multiple zones of contact, is already under development.

Although the proposed methods are able to deal with a large spectrum of contact problems, additional physical conditions such as fluid-structure interaction [61] and thermomechanical effects [32] must be included. Furthermore, applications that require analysis on both macroscopic and microscopic levels (i.e. surface roughness) may require a suitable multi-scale approach [67,87]. The recent improvements introduced to stabilize the constraint fields of enriched interfaces in XFEM and embedded interfaces [51] might have enabled the treatment of another topic: the development and propagation of cracks.

For analysis of real engineering applications, several aspects of the computational implementation must be addressed. In particular, the framework would vastly benefit from a suitable parallel architecture. Both in scalability and efficiency. Faster contact detection methods would also be an interesting topic of further research.

Appendix A

Total Lagrange Formulation

The BVP is solved by imposing a energy balance and a force equilibrium over Γ, such that,

$$\Pi = \Pi_{\text{int,ext}} + \Pi_c - \Pi_w, \tag{A.1}$$

$$\sum_{\gamma_C \cup \gamma_D \cup \gamma_N} \{\mathbf{f}\} = 0 \ \therefore \ \mathbf{f}_c - \mathbf{f}_w = \mathbf{f}_{\text{ext}} - \mathbf{f}_{\text{int}}. \tag{A.2}$$

The external forces are obtained directly from the prescribed tractions. The internal forces, in a Total Lagrangian framework, are obtained by pulling back the stress tensor and the test functions, $\mathbf{v}$, from the current configuration (Ω_t) to the initial configuration (Ω_0) as follows,

$$\begin{aligned}
\mathbf{f}_{\text{int}} &= \int_{\Omega_t} \boldsymbol{\sigma}_t^I : \left[\nabla_0 \left(\mathbf{v}(\varphi^{-1})\right)\right]^T \ d\Omega_t, \\
&= \int_{\Omega_0} J_t^I \boldsymbol{\sigma}_t^I : \left[\nabla_0 \left(\mathbf{v}\right)\right]^T \ d\Omega_0, \\
&= \int_{\Omega_0} \left[\mathsf{F}_0^{I+1}\mathsf{P}_0^{I+1}\right] : \left[\nabla_0 \left(\mathbf{v}\right)\right]^T \left[\mathsf{F}_0^{I+1}\right]^{-1} \ d\Omega_0, \\
&= \int_{\Omega_0} \mathsf{P}_t^I : \left[\nabla_t(\mathbf{v})\right]^T \ d\Omega_0, \\
&= \int_{\Omega_0} \mathsf{S}_t^I : \left[\mathsf{F}_0^{I+1}\right]^T \left[\nabla_t(\mathbf{v})\right]^T \ d\Omega_0, \\
&= \int_{\Omega_0} \mathsf{S}_t^I : \left[\mathsf{E}_0^{I+1}\right] \ d\Omega_0,
\end{aligned} \tag{A.3}$$

where upper index represents the pseudo-time step ("iteration" I) and the values of $\mathbf{v}$ denotes iterative solutions (virtual displacements) for the displacements $\mathbf{u}$. The

contact tractions, $\mathbf{T}$, are also mapped back to the initial referential, such that,

$$\begin{aligned}
&\int_{\{\Gamma_c\}_t} \mathbf{T}_t^I \left(\boldsymbol{\varphi}^{-1}\right) \cdot \mathbf{v}\left(\boldsymbol{\varphi}^{-1}\right) \; d\{\Gamma_c\}_t \,, \\
=&\int_{\{\Gamma_c\}_t} \left[\boldsymbol{\sigma}_t^I \boldsymbol{\eta}_t\right] \left(\boldsymbol{\varphi}^{-1}\right) \cdot \mathbf{v}\left(\boldsymbol{\varphi}^{-1}\right) \; d\{\Gamma_c\}_t \,, \\
=&\int_{\{\Gamma_c\}_0} \left[\boldsymbol{\sigma}_0^I \left[J_0^I\right]^{-1} \boldsymbol{\eta}_0\right] (\mathbf{X}) \cdot \mathbf{v}(\mathbf{X}) \; d\{\Gamma_c\}_0 \,, \\
=&\int_{\{\Gamma_c\}_0} \left[\mathsf{P}_0^I \boldsymbol{\eta}_0\right] (\mathbf{X}) \cdot \mathbf{v}(\mathbf{X}) \; d\{\Gamma_c\}_0 \,, \\
=&\int_{\{\Gamma_c\}_0} \mathbf{T}_0^{I+1} (\mathbf{X}) \cdot \mathbf{v}(\mathbf{X}) \; d\{\Gamma_c\}_0 \,.
\end{aligned} \tag{A.4}$$

The mapping of the normal unit vector, $\boldsymbol{\eta}$, is obtained by applying the Nanson's formula,

$$\boldsymbol{\eta}_t \; d\{\Gamma_c\}_t = \left[J\left(\mathsf{F}_0^I\right)\right]^{-1} \boldsymbol{\eta}_0 \; d\{\Gamma_c\}_0 \,. \tag{A.5}$$

Appendix B

Linearizations

In this appendix a brief list containing the most important linearizations required for obtaining the directional derivatives is presented.

Unnormalized nodal normal for two dimensional problems

$$\hat{\boldsymbol{\eta}}_j = \frac{1}{l_j^1}\hat{\boldsymbol{\eta}}_j^1 + \frac{1}{l_j^2}\hat{\boldsymbol{\eta}}_j^2. \tag{B.1}$$

Directional derivative of $\mathbf{n}_j$ with respect to the nodal displacements $\mathbf{d}$

$$\Delta\boldsymbol{\eta}_j = \Delta\left(\frac{\hat{\boldsymbol{\eta}}_j}{\left\|\hat{\boldsymbol{\eta}}_j\right\|}\right) = \frac{\Delta\hat{\boldsymbol{\eta}}_j}{\left\|\hat{\boldsymbol{\eta}}_j\right\|} - \frac{\left[\hat{\boldsymbol{\eta}}_j \cdot \Delta\hat{\boldsymbol{\eta}}_j^1\right]\hat{\boldsymbol{\eta}}_j}{\left\|\hat{\boldsymbol{\eta}}_j\right\|^3}. \tag{B.2}$$

Directional derivative of the tangential vector

$$\Delta\boldsymbol{\tau}_j = \mathbf{e}_3 \times \Delta\boldsymbol{\eta}_j \tag{B.3}$$

2D Directional derivative of matrix $\mathbf{D}$

$$\begin{aligned}
\Delta D_{jk} = &\sum_{g=1}^{n_{gp}} w_{gp}\Delta\phi_j(\xi^s)N_k^s(\xi^s)J\left((\xi^s)\right)\ \frac{\xi_b^s - \xi_a^s}{2} \\
&+ \sum_{g=1}^{n_{gp}} w_{gp}\phi_j(\xi^s)\Delta N_k^s(\xi^s)J\left((\xi^s)\right)\ \frac{\xi_b^s - \xi_a^s}{2} \\
&+ \sum_{g=1}^{n_{gp}} w_{gp}\phi_j(\xi^s)N_k^s(\xi^s)\Delta J\left((\xi^s)\right)\ \frac{\xi_b^s - \xi_a^s}{2} \\
&+ \sum_{g=1}^{n_{gp}} w_{gp}\phi_j(\xi^s)\Delta N_k^s(\xi^s)\ J\left((\xi^s)\right)\ \frac{\Delta\xi_b^s - \Delta\xi_a^s}{2}.
\end{aligned} \tag{B.4}$$

2D Directional derivatives of one entry of $\mathbf{M}$

$$\begin{aligned}\Delta M_{jl} = &\sum_{g=1}^{n_{gp}} w_{gp}\Delta\phi_j(\xi^s)N_l^m(\xi^m)J\left((\xi^s)\right)\ \frac{\xi_b^s-\xi_a^s}{2}\\ &+\sum_{g=1}^{n_{gp}} w_{gp}\phi_j(\xi^s)\Delta N_l^m(\xi^m)J\left((\xi^s)\right)\ \frac{\xi_b^s-\xi_a^s}{2}\\ &+\sum_{g=1}^{n_{gp}} w_{gp}\phi_j(\xi^s)N_l^m(\xi^m)\Delta J\left((\xi^s)\right)\ \frac{\xi_b^s-\xi_a^s}{2}\\ &+\sum_{g=1}^{n_{gp}} w_{gp}\phi_j(\xi^s)N_l^m(\xi^m)J\left((\xi^s)\right)\ \frac{\Delta\xi_b^s-\Delta\xi_a^s}{2}.\end{aligned} \tag{B.5}$$

3D Directional derivative of matrix $\mathbf{D}$

$$\begin{aligned}\Delta D_{jk} = &\sum_{g=1}^{n_{gp}} w_{gp}\Delta\phi_j(\xi^s)N_k^s(\xi^s)J_{cell}\\ &+\sum_{g=1}^{n_{gp}} w_{gp}\phi_j(\xi^s)\Delta N_k^s(\xi^s)J_{cell}\\ &+\sum_{g=1}^{n_{gp}} w_{gp}\phi_j(\xi^s)N_k^s(\xi^s)\Delta J_{cell}.\end{aligned} \tag{B.6}$$

3D Directional derivatives of one entry of $\mathbf{M}$

$$\begin{aligned}\Delta M_{jk} = &\sum_{g=1}^{n_{gp}} w_{gp}\Delta\phi_j(\xi^s)N_l^m(\xi^m)J_{cell}\\ &+\sum_{g=1}^{n_{gp}} w_{gp}\phi_j(\xi^s)\Delta N_l^m(\xi^m)J_{cell}\\ &+\sum_{g=1}^{n_{gp}} w_{gp}\phi_j(\xi^s)N_l^m(\xi^m)\Delta J_{cell}.\end{aligned} \tag{B.7}$$

where the dual-basis functions ϕ are defined obtained by solving the bi-orthogonality condition at the element level,

$$\begin{bmatrix}\Delta\phi_1\left(\xi^s\right)\\ \vdots\\ \Delta\phi_{n_e^s}\left(\xi^s\right)\end{bmatrix} = \Delta\mathsf{A}_e\begin{bmatrix}N_1^s\left(\xi^s\right)\\ \vdots\\ N_{n_e^s}^s\left(\xi^s\right)\end{bmatrix}. \tag{B.8}$$

Jacobian

$$J\left(\xi\right) = \left\|\sum_{k=1}^{n_s^e} N_k^s\ \mathbf{x}_k^s\right\|. \tag{B.9}$$

Directional derivative of J

$$\Delta J\left(\xi\right)=\frac{1}{J\left(\xi\right)}\left[\sum_{k=1}^{n_s^e}\ N_k^s\ \mathbf{x}_k^s\right]\cdot\left[\sum_{k=1}^{n_s^e}\ N_k^s\ \Delta\mathbf{x}_k^s+\sum_{k=1}^{n_s^e}\ N_k\Delta\mathbf{x}_k^s\right]. \tag{B.10}$$

Directional derivative of the discrete weighted gap $\tilde{g}_j$:

$$\begin{aligned}\Delta\tilde{g}_j=&-\left[\boldsymbol{\eta}_j\right]^T\left\{\sum_{k=1}^{n_s}\left\{\mathbf{D}_{[j,k]}\Delta\mathbf{d}_k^s\right\}-\sum_{l=1}^{n_m}\left\{\mathbf{M}_{[j,l]}\Delta\mathbf{d}_l^m\right\}\right\}\\&-\left[\Delta\boldsymbol{\eta}_j\right]^T\left\{\sum_{k=1}^{n_s}\left\{\mathbf{D}_{[j,k]}\mathbf{x}_k^s\right\}-\sum_{l=1}^{n_m}\left\{\mathbf{M}_{[j,l]}\mathbf{x}_l^m\right\}\right\}\\&-\left[\boldsymbol{\eta}_j\right]^T\left\{\sum_{k=1}^{n_s}\left\{\Delta\mathbf{D}_{[j,k]}\mathbf{x}_k^s\right\}-\sum_{l=1}^{n_m}\left\{\Delta\mathbf{M}_{[j,l]}\mathbf{x}_l^m\right\}\right\}.\end{aligned} \tag{B.11}$$

Directional derivative of the wear depth, $\left\{\tilde{u}_\tau\right\}_j$:

$$\begin{aligned}\left\{\tilde{u}_\tau\right\}_j^{\mathbb{k}}=&-\left[\boldsymbol{\tau}_j^{\mathbb{k}}\right]\left\{\mathbf{D}\left[j,j\right]^{\mathbb{k}}-\mathbf{D}\left[j,j\right]\right\}\Delta\left\{\mathbf{d}_j^s\right\}^{\mathbb{k}}\\&+\left[\boldsymbol{\tau}_j^{\mathbb{k}}\right]\sum_{l=1}^{n_m}\left\{\mathbf{M}\left[j,l\right]^{\mathbb{k}}-\mathbf{M}\left[j,l\right]\right\}\Delta\left\{\mathbf{d}_l^m\right\}^{\mathbb{k}}\\&-\left[\Delta\boldsymbol{\tau}_j^{\mathbb{k}}\right]\left\{\mathbf{D}\left[j,j\right]^{\mathbb{k}}-\mathbf{D}\left[j,j\right]\right\}\left\{\mathbf{x}_j^s\right\}^{\mathbb{k}}\\&+\left[\Delta\boldsymbol{\tau}_j^{\mathbb{k}}\right]\sum_{l=1}^{n_m}\left\{\mathbf{M}\left[j,l\right]^{\mathbb{k}}-\mathbf{M}\left[j,l\right]\right\}\left\{\mathbf{x}_l^m\right\}^{\mathbb{k}}\\&-\left[\boldsymbol{\tau}_j^{\mathbb{k}}\right]\left\{\Delta\mathbf{D}\left[j,j\right]^{\mathbb{k}}+\sum_{l=1}^{n_m}\Delta\mathbf{D}\left[j,j\right]\right\}\Delta\left\{\mathbf{d}_j^s\right\}^{\mathbb{k}}.\end{aligned} \tag{B.12}$$

Directional derivative of the wear depth, $\tilde{h}_j$:

$$\begin{aligned}\Delta\tilde{h}_j=&\frac{\mu\alpha_w}{n_{nod}^{adj}}\left\|\left\{z_\eta\right\}_j\right\|\left[\boldsymbol{\eta}_j\right]^T\left\{\sum_{k=1}^{n_s}\left\{\mathbf{D}_{[j,k]}\Delta\mathbf{d}_k^s\right\}+\sum_{l=1}^{n_m}\left\{\mathbf{M}_{[j,l]}\Delta\mathbf{d}_l^m\right\}\right\}\\&+\frac{\mu\alpha_w}{n_{nod}^{adj}}\left\|\left\{z_\eta\right\}_j\right\|\left[\Delta\boldsymbol{\eta}_j\right]^T\left\{\sum_{k=1}^{n_s}\left\{\mathbf{D}_{[j,k]}\mathbf{x}_k^s\right\}+\sum_{l=1}^{n_m}\left\{\mathbf{M}_{[j,l]}\mathbf{x}_l^m\right\}\right\}\\&+\frac{\mu\alpha_w}{n_{nod}^{adj}}\left\|\Delta\left\{z_\eta\right\}_j\right\|\left[\boldsymbol{\eta}_j\right]^T\left\{\sum_{k=1}^{n_s}\left\{\mathbf{D}_{[j,k]}\mathbf{x}_k^s\right\}+\sum_{l=1}^{n_m}\left\{\mathbf{M}_{[j,l]}\mathbf{x}_l^m\right\}\right\}\\&+\frac{\mu\alpha_w}{n_{nod}^{adj}}\left\|\left\{z_\eta\right\}_j\right\|\left[\boldsymbol{\eta}_j\right]^T\left\{\sum_{k=1}^{n_s}\left\{\Delta\mathbf{D}_{[j,k]}\mathbf{x}_k^s\right\}+\sum_{l=1}^{n_m}\left\{\Delta\mathbf{M}_{[j,l]}\mathbf{x}_l^m\right\}\right\}.\end{aligned} \tag{B.13}$$

Appendix C

Penalty method

The so-called Penalty method is obtained by basically the addition of penalty parameters in the weak form in order to satisfy the constraints conditions,

$$\Pi(\mathbf{u})^{\text{PM}} = \Pi(\mathbf{u}) + \frac{1}{2}\mathbf{g}^T \epsilon_\eta \mathbf{g}$$

$$= \Pi(\mathbf{u}) + \frac{1}{2}\int_\Gamma \left(\left[\epsilon_\eta \left(\overline{g}_\eta \right)^2 \right] + \epsilon_\tau \ \overline{g}_\tau \cdot \overline{g}_\tau \right) dA, \quad \epsilon_\eta, \epsilon_\tau > 0. \tag{C.1}$$

where ϵ and ϵ_τ represent the penalty parameters, $\overline{g}_\tau$ is the *tangential displacement* while $\overline{g}_\eta$ is defined as the *normal penetration function* which has the magnitude of g_η and the direction of $\overline{\mathbf{n}}^1$

$$\overline{g}_\eta = \begin{cases} [(\mathbf{x}^m - \overline{\mathbf{x}}^s)\cdot\overline{\mathbf{n}}^s]\overline{\mathbf{n}}^s & \text{if} \quad (\mathbf{x}^m - \mathbf{x}^s)\cdot\overline{\mathbf{n}}^s < 0, \\ 0, \ \text{otherwise.} \end{cases} \tag{C.2}$$

The most important feature of this regularization method consist in the direct definition of the *normal contact force* and *tangential contact force* by means of the normal penetration function g_η and the tangential displacement $\overline{g}_\tau$ respectively,

$$F_\eta = \epsilon_\eta g_\eta; \ F_\tau = \epsilon_\tau g_\tau. \tag{C.3}$$

The addiction of these "penalities" has got the objective of decreasing the influence of the element stiffness of the contacting nodes and creating a relationship among them. The constraint formulation for the penalty method is obtained from the variation of Equation (C.4) in terms of the nodal displacements

$$\partial\Pi(\mathbf{u})^{\text{PM}} = \partial\Pi(\mathbf{u}) + \int_\Gamma \left(\epsilon_\eta \overline{g}_\eta \ \delta\overline{g}_\eta + \epsilon_\tau \ \overline{g}_\tau \cdot \delta\overline{g}_\tau \right) dA \ = \ \mathbf{0}. \tag{C.4}$$

Further development of Eq. (C.4) will lead to its discretized form:

$$\left[\mathsf{K}\mathbf{u} - \mathbf{R} + \left(\epsilon_\eta \left[\frac{\partial \overline{g}_\eta}{\partial \mathbf{u}} \right] \left[\frac{\partial \overline{g}_\eta}{\partial \mathbf{u}} \right]^T + \epsilon_\tau \left[\frac{\partial \overline{g}_\tau}{\partial \mathbf{u}} \right] \left[\frac{\partial \overline{g}_\tau}{\partial \mathbf{u}} \right]^T \right) \mathbf{u} \right] [\partial \mathbf{u}]^T = \mathbf{0}$$

$$\left[\mathsf{K} + \left(\epsilon_\eta \left[\frac{\partial \overline{g}_\eta}{\partial \mathbf{u}}\right] \left[\frac{\partial \overline{g}_\eta}{\partial \mathbf{u}}\right]^T + \epsilon_\tau \left[\frac{\partial \overline{g}_\tau}{\partial \mathbf{u}}\right] \left[\frac{\partial \overline{g}_\tau}{\partial \mathbf{u}}\right]^T\right)\right] \mathbf{u} = \mathbf{R}$$

$$\Rightarrow \left[\mathsf{K} + \mathsf{K}^{\mathrm{PM}}\right] \mathbf{u} = \mathbf{R} \tag{C.5}$$

The force vector $\mathbf{R}$ for the Penalty method can be split in two members: $\mathbf{R}_{\mathrm{ext}}$, which is related to the external forces, and $\mathbf{R}_{\mathrm{ct}}$, that represents the contact forces,

$$\mathbf{R}_{\mathrm{ct}} = \epsilon_\eta \overline{g}_\eta + \epsilon_\tau \overline{g}_\tau. \tag{C.6}$$

From Eq. (C.5) it is possible observe that the main advantages of the penalty method rely on the maintenance of the total number of degrees of freedom (and so the number of equations in the system) and the fact that the normal contact force, F_η, can be expressed only in terms of g. Nevertheless the constraints are satisfied in an approximate manner and only if the correct range of penalty parameters is chosen. The penetration depends upon the value of penalty parameter and the constraint equation is only fulfilled in the limit $\epsilon \to \infty$. Hence, one can distinguish the penalty method in two cases:

- If ϵ is too low the constraints are poorly satisfied leading to a high penetration;
- For a large value of the penalty parameter, ϵ, the penetration remains small and better is the given solution obtained in terms of contact enforcement. However if the penalty value is too high the stiffness matrix becomes ill conditioned and harder to solve.

Appendix D

Patch tests

Two patch tests are presented in this Appendix. They show the difficulties presented by the NTS Penalty method to correctly enforce the contact constraints.

In both tests, the solids are discretized with 4-noded quadrilateral elements. Frictionless contact is assumed. The normal penalty multipliers is set to $\epsilon_\eta = 10^5$ while the normal complementarity parameter is $c_\eta = 100$. The material properties of the solids are: $E = 210GPa$, $G = 76GPa$, $\nu = 0.33$, $\sigma_y = 830MPa$ and $\sigma = \sigma_y + 600\epsilon^{0.21}$.

The geometry and the mesh discretization used for the first test is shown in Figure D.1. A distributed load equal to $1kN/mm$ is applied within 20 equally divided increments.

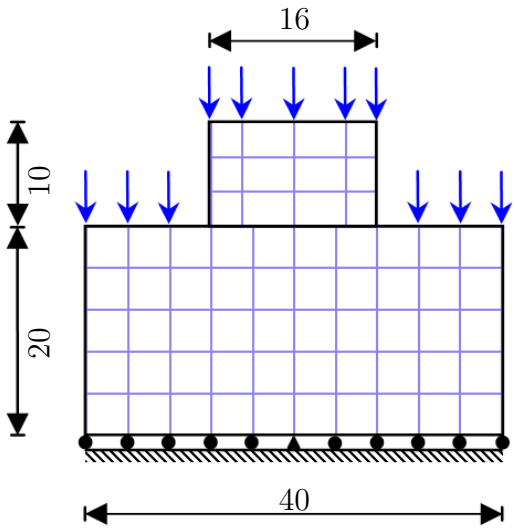

Figure D.1: Patch test 1 - geometry and FE discretization.

It is possible to observe from Figure D.2a when the structure reaches the plastic regime of deformation the values chosen for the penalty parameters are not high enough to avoid penetration between solids. The results shown by the Dual Mortar method are much more consistent, as can be seen in Figure D.2b.

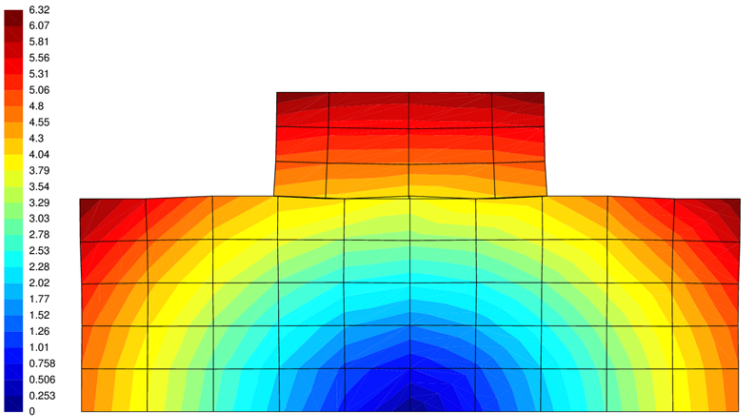

(a) Penalty method.

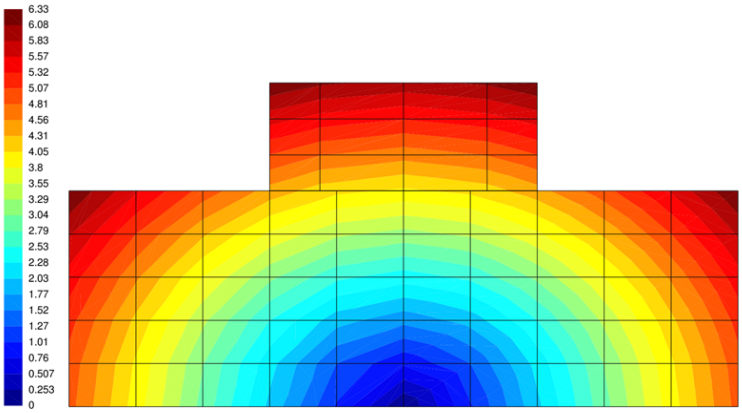

(b) Dual-Mortar method.

Figure D.2: Patch test 1 - Displacement field.

The second patch test is depicted in Figure D.3. In this test, a prescribed vertical displacement equal to $-15mm.$ is applied to the top of the structure. Symmetry in x-direction is assumed.

Once again, the structure shows penetration (see Figure D.4a) at the interface of the solids when employing the NTS Penalty method. However, the Dual Mortar method displays a correct constraint enforcement, as observed in Figure D.5a. The penetration observed in the results provided by the NTS Penalty method compromise the correct evaluation of the stress distribution, see Figures D.4b. On the other hand, the Dual Mortar method provides a perfect distribution over the structure. These results indicate that the penalty parameters are more unstable than the complementarity parameters when solids are undergoing plastic deformation.

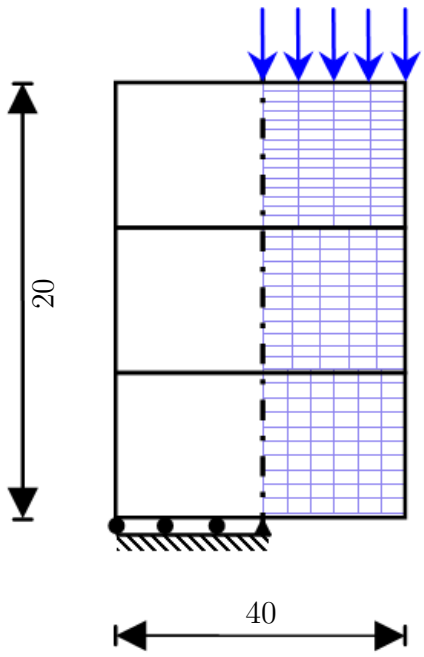

Figure D.3: Patch test 2 - geometry and FE discretization.

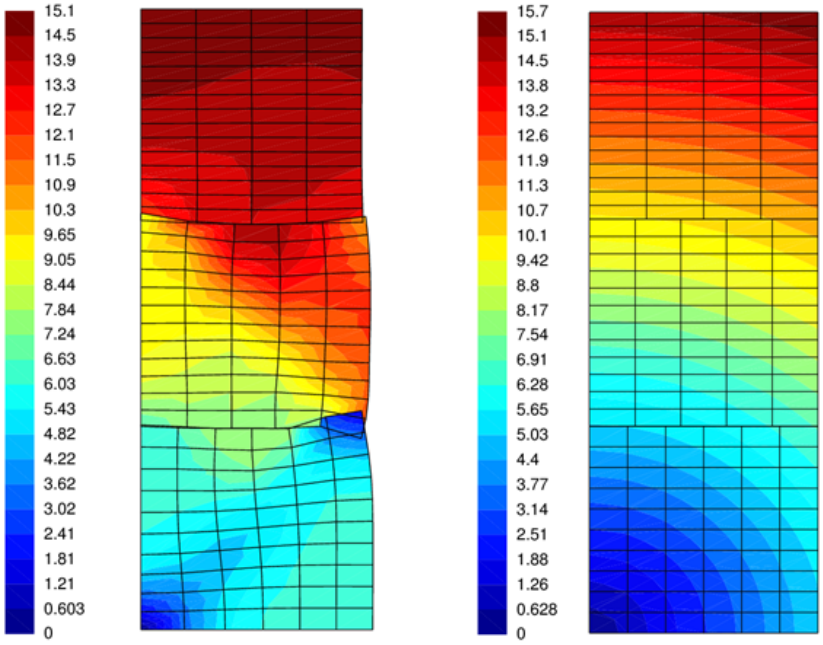

(a) Penalty method. (b) Dual Mortar method.

Figure D.4: Patch test 2 - Displacement field.

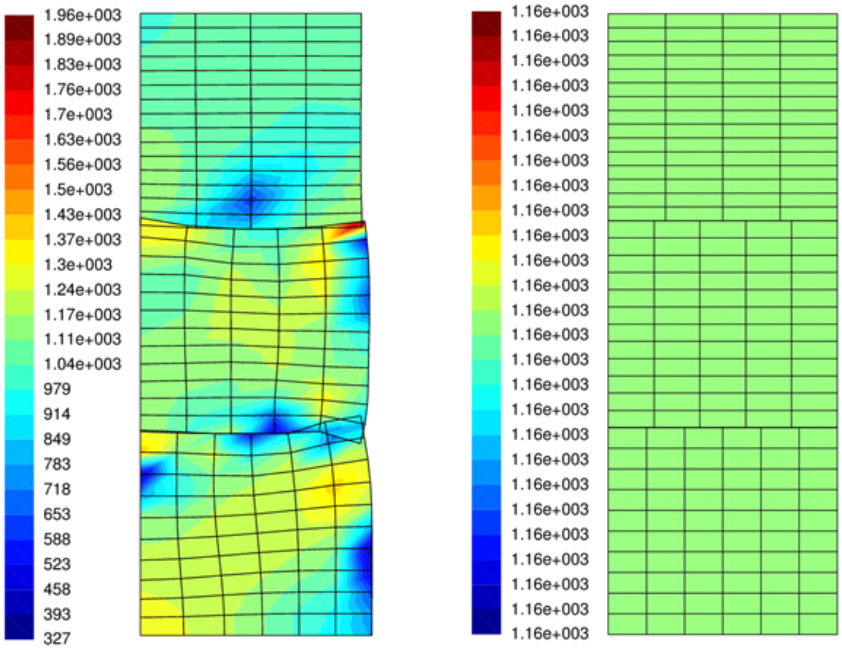

(a) Penalty method. (b) Dual-Mortar method.

Figure D.5: Patch test 2 - Stress distribution.

Bibliography

[1] P. Alart and A. Curnier. A mixed formulation for frictional contact problems prone to newton like solution methods. *Computer Methods in Applied Mechanics and Engineering*, 92: 353–375, 1991.

[2] J.F. Archard. Contact and rubbing of flat surfaces. *Journal of Applied Physics*, 24 (8): 981–988, 1991.

[3] F. Armero and E. Love. An arbitrary lagrangian-eulerian finite element method for finite strain plasticity. *International Journal for Numerical Methods in Engineering*, 57: 471–508, 2003.

[4] K.J. Bathe and A. Chaudhary. A finite element method for a class of contact-impact problems. *International Journal for Numerical Methods in Engineering*, 21: 65–88, 1985.

[5] F. Belgacem, P. Hild, and P. Laborde. The mortar finite element method for contact problems. *Mathematical and Computer Modelling*, 28: 263–271, 1998.

[6] F Belgacem and Y. Maday. A spectral element methodology tuned to parallel implementations. *Computer Methods in Applied Mechanics and Engineering*, 116: 59–67, 1994.

[7] Z. Belhachmi and C. Bernardi. Resolution of fourth order problems by the mortar element method. *Mathematical and Computer Modelling*, 28: 263–271, 1998.

[8] T. Belytschko, W.K. Liu, and B. Moran. *Nonlinear finite elements for continua and structures*. Wiley, 2000.

[9] C. Bernardi, Y. Maday, and A. Patera. A new nonconforming approach to domain decomposition: the mortar element method. *In Nonlinear Partial Differential Equations and Their Applications. Brezis H, Lions J (eds). Pitman/Wiley: London/New York*, pages 13–51, 1994.

[10] S. Brunssen, F. Schmid, M. Schäfer, and B.I. Wohlmuth. A fast and robust iterative solver for nonlinear contact problems using a primal-dual active set strategy and algebraic multigrid. *International Journal for Numerical Methods in Engineering*, 69: 524–543, 2007.

[11] P.W. Christensen. A nonsmooth newton method for elastoplastic problems. *Computer Methods in Applied Mechanics and Engineering*, 191: 1189–1219, 1977.

[12] G.R. Cowper. Gaussian quadrature formulas for triangles. *International Journal for Numerical Methods in Engineering*, 7: 405–408, 1973.

[13] M.A. Crisfield. *Non-linear Finite Element Analysis of Solids and Structures. Vol. 2: Advanced Topics*. John Wiley & Sons: Chichester, 1997.

[14] A. Cuitiño and M. Ortiz. A material-independent method for extending stress update algorithms from small-strain plasticity to finite plasticity with multiplicative kinematics. *Engineering Computations*, 9: 437–451, 1992.

[15] E.A. de Souza Neto, D. Perić, M. Dutko, and D.R.J. Owen. Design of simple low order finite elements for large strain analysis of nearly incompressible solids. *International Journal of Solids and Structures*, 33: 3277–3296, 1996.

[16] E.A. de Souza Neto, D. Perić, and D.R.J. Owen. *Computational Methods for Plasticity: Theory and Application*. John Wiley & Sons Ltd, 2008.

[17] J. Ding, S.B. Leen, and I.R. McColl. The effect of slip regime on fretting wear-induced stress evolution. *International Journal of Fatigue*, 26: 521–531, 2004.

[18] T. Doca, F.M. Andrade Pires, and J.M.A. Cesar de Sa. A frictional mortar contact approach for the analysis of large inelastic deformation problems. *International Journal for Solids and Structures*, 51: 1697–1715, 2014.

[19] T. Erhart, W.A. Wall, and E. Ramm. Robust adaptive remeshing strategy for large deformation, transient impact simulations. *International Journal for Numerical Methods in Engineering*, 65: 2139–2166, 2006.

[20] A.L. Eterovic and K.-J. Bathe. A hyperelastic-based large strain elasto-plastic constitutive formulation with combined isotropic-kinematic hardening using logarithmic stress and strain measures. *International Journal for Numerical Methods in Engineering*, 30: 1099–1114, 1985.

[21] F. Facchinei and J.-S. Pang. *Finite-Dimensional Variational Inequalities and Complementary Problems*, volume 1. Springer, 1998.

[22] K.A. Fischer and P. Wriggers. Mortar based frictional contact formulation for higher order interpolations using the moving friction cone. *Computer Methods in Applied Mechanics and Engineering*, 195:5020–5036, 2006.

[23] B. Flemisch and B.I. Wohlmuth. Stable lagrange multipliers for quadrilateral meshes of curved interfaces in 3d. *Computer Methods in Applied Mechanics and Engineering*, 196: 1589–1602, 2007.

[24] J.D. Foley, A. van Dam, S.K. Feiner, and J.F. Hughes. *Computer Graphics, Principles and Practice*. Addison-Wesley, 1990.

[25] S. Fouvry, P. Duo, and Ph. Perruchaut. A quantitative approach of ti-6a1-4v fretting damage: friction, wear and crack nucleation. *Wear*, 257: 916–929, 2004.

[26] S. Fouvry, P. Kapsa, H. Zahouani, and L. Vincent. Wear analysis in fretting of hard coatings through a dissipated energy concept. *Wear*, 203-204: 393–403, 1997.

[27] S. Fouvry, T. Liskiewicz, Ph. Kapsa, S. Hannel, and E. Sauger. An energy description of wear mechanisms and its applications to oscillating sliding contacts. *Wear*, 255: 287–298, 2003.

[28] S. Fouvry, C. Paulin, and T. Liskiewicz. Application of an energy wear approach to quantify fretting contact durability: Introduction of a wear energy capacity concept. *Tribology International*, 40: 1428–1440, 2007.

[29] S. Fouvry, L. Vincent, and P. Kapsa. Quantification of fretting damage. *Wear*, 200: 186–205, 1996.

[30] A. Francavilla and O.C. Zienkiewicz. A note on numerical computation of elastic contact problems. *International Journal for Numerical Methods in Engineering*, 9: 913–924, 1975.

[31] B. Fredriksson. Finite element solution of surface nonlinearities in structural mechanics with special emphasis to contact and fracture mechanics problems. *Computer and Structures*, 6: 281–290, 1976.

[32] M. Gitterle. *A dual mortar formulation for finite deformation frictional contact problems including wear and thermal coupling*. PhD thesis, Technische Universität München, 2012.

[33] M. Gitterle, A. Popp, M.W. Gee, and W.A. Wall. Finite deformation frictional mortar contact using a semi-smooth newton method with consistent linearization. *International Journal for Numerical Methods in Engineering*, 84: 543–571, 2010.

[34] W. Goldsmith. *Impact: The Theory and Physical Behavior of Colliding Solids*. Edward Arnold, 1960.

[35] C. Hager and B.I. Wohlmuth. Nonlinear complementarity functions for plasticity problems with frictional contact. *Computer Methods in Applied Mechanics and Engineering*, 198: 3411–3427, 2003.

[36] J. Hallquist, G. Goudreau, and D. Benson. Sliding interfaces with contact-impact in large-scale lagrangian computations. *Computer Methods in Applied Mechanics and Engineering*, 51: 107–137, 1985.

[37] S. Hartmann and E. Ramm. A mortar based contact formulation for non-linear dynamics using dual lagrange multipliers. *Finite Elements in Analysis and Design*, 44: 245–258, 2004.

[38] H. Hertz. Über die berührung fester elastischer körper (on contact between elastic bodies). *Journal für die Reine und Angewandte Mathematik*, 29: 156–171, 2009.

[39] M. Hintermüller, K. Ito, and K. Kunisch. The primal-dual active set strategy as a semi-smooth newton method. *SIAM Journal on Optimization*, 13: 865–888, 2003.

[40] S. Hüeber. *Discretization techniques and efficient algorithms for contact problems*. PhD thesis, Universität Stuttgart, 2008.

[41] S. Hüeber, G. Stadler, and B.I. Wohlmuth. A primal-dual active set algorithm for three-dimensional contact problems with coulomb friction. *SIAM Journal on Scientific Computing*, 30: 572–596, 2008.

[42] S. Hüeber and B.I. Wohlmuth. Nonlinear complementarity functions for plasticity problems with frictional contact. *SIAM Journal on Numerical Analysis*, 43: 157–173, 2005.

[43] S. Hüeber and B.I. Wohlmuth. A primal-dual active set strategy for non-linear multibody contact problems. *Computer Methods in Applied Mechanics and Engineering*, 194: 3147–3166, 2005.

[44] T.J.R. Hughes, R.L. Taylor, J.L. Sackman, A. Curnier, and W. Kanoknukulchai. A finite element method for a class of contact-impact problems. *Computer Methods in Applied Mechanics and Engineering*, 8: 249–276, 1976.

[45] K.L. Johnson. Contact mechanics and the wear of metals. *Wear*, 190, 1995.

[46] K.L. Jonhson. *Contact Mechanics*. Cambridge University Press, 1987.

[47] J.W. Ju and R.L. Taylor. A perturbed lagrangian formulation for the finite element solution of nonlinear frictional contact problems. *Journal de Mecanique Theorique et Appliquée*, 7(1): 1–14, 1988.

[48] N. Kikuchi and J. Oden. *Contact problems in elasticity: a study of variational inequalities and finite element methods*. SIAM Studies in Applied Mathematics, 1988.

[49] T. Koziara and N. Bicanic. Semismooth newton method for frictional contact between pseudo-rigid bodies. *Computer Methods in Applied Mechanics and Engineering*, 197: 2763–2777, 2008.

[50] T.A. Laursen. *Computational Contact and Impact Mechanics: Fundamentals of Modeling Interfacial Phenomena in Nonlinear Finite Element Analysis*. Springer-Verlag, 2002.

[51] T.A. Laursen, M. A. Puso, and J. Sanders. Mortar contact formulations for deformable-deformable contact: Past contributions and new extensions for enriched and embedded interface formulations. *Computer Methods in Applied Mechanics and Engineering*, 3-15: 205–208, 2012.

[52] E.H. Lee. Elastic-plastic deformation at finite strains. *Journal of Applied Mechanics*, 36: 1–6, 1969.

[53] I.R. McColl, J. Ding, and S.B. Leen. Finite element simulation and experimental validation of fretting wear. *Wear*, 256: 1114–1127, 2004.

[54] T.W. McDevitt and T.A. Laursen. A mortar-finite element formulation for frictional contact problems. *International Journal for Numerical Methods in Engineering*, 48: 1525–1547, 2000.

[55] J.T. Oden. Exterior penalty methods for contact problems in elasticity. *Nonlinear Finite Element Analysis in Structural Mechanics*, pages 655–665, 1981.

[56] M. Ortiz and E.P. Popov. Accuracy and stability of integration algorithms for elastoplastic constitutive relations. *International Journal for Numerical Methods in Engineering*, 21: 1561–1576, 1985.

[57] P. Papadopoulos and R.L. Taylor. A mixed formulation for the finite element solution of contact problems. *Computer Methods in Applied Mechanics and Engineering*, 94: 373–389, 1992.

[58] C. Paulin, S. Fouvry, and C. Meunier. Finite element modelling of fretting wear surface evolution: Application to a ti-6a1-4v contact. *Wear*, 264: 26–36, 2008.

[59] D. Perić, D.R.J. Owen, and M. Honnor. A model for large strain elastoplasticity based on logarithmic strain: computational issues. *Computer Methods in Applied Mechanics and Engineering*, 94: 35–61, 1992.

[60] P. Põdra and S. Andersson. Simulating sliding wear with finite element method. *Tribology International*, 32: 71–81, 1999.

[61] A. Popp. *Mortar methods for Computational Contact Mechanics and General Interface Problems*. PhD thesis, Technische Universität München, 2012.

[62] A. Popp, M. W. Gee, and W. A. Wall. A finite deformation mortar contact formulation using a primal-dual active set strategy. *Computer Methods in Applied Mechanics and Engineering*, 79: 1354–1391, 2009.

[63] M. A. Puso, T. A. Laursen, and J. Solberg. A segment-to-segment mortar contact method for quadratic elements and large deformations. *Computer Methods in Applied Mechanics and Engineering*, 197:555–566, 2008.

[64] M.A. Puso and T.A. Laursen. A 3d contact smoothing method using gregory patches. *International Journal for Numerical Methods in Engineering*, 54: 1161–1194, 2002.

[65] E. Rabinowicz. *Friction and Wear of Materials*. John Wiley and Sons, 1995.

[66] A. Ramalho and J.C. Miranda. The relationship between wear and dissipated energy in sliding systems. *Wear*, 60: 361–367, 2006.

[67] F.J.P. Reis and F.M. Andrade Pires. A mortar based approach for the enforcement of periodic boundary conditions on arbitrarily generated meshes. *Computer Methods in Applied Mechanics and Engineering*, 274: 168–191, 2014.

[68] A. Signorini. Sopra akune questioni di elastostatica. *Atti della Societa Italiana per il Progresso delle Scienze*, 1933.

[69] J.C. Simo. Algorithms for static and dynamic multiplicative plasticity that preserve the classical return mapping schemes of the infinitesimal theory. *Computer Methods in Applied Mechanics and Engineering*, 99: 61–112, 1992.

[70] J.C. Simo and T.J.R. Hughes. *Computational Inelasticity*. Springer, 1998.

[71] J.C. Simo and T.A. Laursen. An augmented lagrangian treatment of contact problems involving friction. *Computers and Structures*, 42: 97–116, 1992.

[72] J.C. Simo, P. Wriggers, and R.L. Taylor. A perturbed lagrangian formulation for the finite element solution of contact problems. *Computer Methods in Applied Mechanics and Engineering*, 50: 163–180, 1985.

[73] M. Stadler and G. Holzapfel. Subdivision schemes for smooth contact surfaces of arbitrary mesh topology in 3d. *International Journal for Numerical Methods in Engineering*, 60: 1161–1195, 2004.

[74] J.T. Stadter and Weiss R.O. Analysis of contact through finite element gaps. *Computers and Structures*, 10: 867–873, 1979.

[75] Laursen T.A. and Simo J.C. A continuum-based finite element formulation for the implicit solution of multi-body, large deformation frictional contact problems. *International Journal for Numerical Methods in Engineering*, 36: 3451–3485, 1993.

[76] S.P. Timoshenko and Goodier J.N. *Theory of Elasticity*. McGraw-Hill, 1970.

[77] M. Tur, E. Giner, F.J. Fuenmayor, and P. Wriggers. 2d contact smooth formulation based on the mortar method. *Computer Methods in Applied Mechanics and Engineering*, 247-248: 1–14, 2012.

[78] O. Vingsbo and S. Soderberg. On fretting map. *Wear*, 26: 131–147, 1988.

[79] R.B. Waterhouse. *Fretting Fatigue*. Applied Science publishers, 1981.

[80] R.B. Waterhouse. Fretting wear in asm handbook, friction lubrication, and wear technology. *ASM International*, 18: 242–256, 1992.

[81] G. Weber and L. Anand. Finite deformation constitutive equations and a time integration procedure for isotropic, hyperelastic-viscoplastic solids. *Computer Methods Applied Mechanics and Engineering*, 79: 173–202, 1990.

[82] E.A. Wilson and B. Parsons. Finite element analysis of elastic contact problems using differential displacements. *International Journal for Numerical Methods in Engineering*, 2: 387–395, 1970.

[83] B.I. Wohlmuth. A mortar finite element method using dual spaces for the lagrange multiplier. *SIAM Journal on Numerical Analysis*, 38: 989–1012, 2000.

[84] B.I. Wohlmuth. *Discretization Methods and Iterative Solvers Based on Domain Decomposition*. Springer, 2001.

[85] P. Wriggers. *Computational Contact Mechanics*. Wiley & Sons Ltd., 2006.

[86] P. Wriggers, L. Krstulovic-Opara, and J. Korelc. Smooth c1-interpolations for two-dimensional frictional contact problems. *International Journal for Numerical Methods in Engineering*, 51: 1469–1495, 2001.

[87] P. Wriggers, T. Vu Van, and E. Stein. Finite element formulation of large deformation impact-contact problems with friction. *Computers and Structures*, 37: 319–331, 1990.

[88] B. Yang, T.A. Laursen, and X. Meng. Two dimensional mortar contact methods for large deformation frictional sliding. *International Journal for Numerical Methods in Engineering*, 62: 1183–1225, 2005.